

A MLEM Approach to Range Verification for Proton Beam Therapy using 3-D Position Sensing CdZnTe

by

Valerie E. Nwadeyi

A dissertation submitted in partial fulfillment
of the requirements for the degree of
Doctor of Philosophy
(Nuclear Engineering and Radiological Sciences)
in The University of Michigan
2021

Doctoral Committee:

Professor Zhong He, Chair
Professor Jeffrey Fessler
Dr. Paul Maggi, Sandia National Laboratory
Professor Jerimy Polf, University of Maryland
Professor Sara Pozzi

Valerie E. Nwadeyi

vnwadeyi@umich.edu

ORCID iD: 0000-0002-1629-1012

© Valerie E. Nwadeyi 2021

To my mommy. For teaching me the true meaning of love, faith, hard work, and sacrifice.
Zephaniah 3:17

ACKNOWLEDGEMENTS

Wrigley, thank you for making the sugar free double mint gum, bounds better than the original. Your gum has always been there when work was too stressful or I just needed a Jimmy Neutron brain blast, I'm chewing as a I type this actually...

Firstly, to my research advisor, Professor Zhong He, thank you for setting the tone and the exemplary standard of the Orion Research Group. I am thankful to you for your leadership, helping hand, and understanding. In the summer of 2015, you took a chance and let me intern with your group as an eager undergrad who was not sure about her next steps. From that moment you have provided me the space to learn and grow as a researcher, and for that I am eternally grateful. I am also thankful for everyone that is a part of my thesis committee. To Professor Fessler and Professor Polf thank you both for your wisdom and guidance through my research, none of my questions ever went unanswered and I am thankful for your patience and support as I was discovering my approach to research. I am also thankful to Dr. Paul Maggi, your support and helping hand in my research has been vital. And to Professor Pozzi, thank you for your unwavering support of me as a student leader and researcher. I would also like to extend gratitude to the Maryland Proton Therapy Center for allowing me to conduct research in your facility and to H3D Inc. for letting me use, test, and give input on CZT detection systems. Thank you to my funding institutions: the Rackham Merit Fellowship and CVT (Consortium for Verification Technology) and MTV (Monitoring, Technology, and Verification) DE-NNSA 0002534 and DE-NA0003920, respectively.

I have been blessed to meet and be surrounded by so many bright and kindhearted people, who have played such an integral role in my graduate tenure. To the Orion Research Group, thank you all, past and present, for being such an inspiring group of minds. Your work never ceases to amaze me and push me to give my best. I am especially thankful to Dr. Will Koehler for allowing me to work under him as an intern and taking the time to explain not only TlBr detectors, but a host of fundamental detection physics topics. Dr. David Goodman's and Dr. Steven Brown's work is what inspired me to take on radiation imaging for my graduate career, thank you both for your insight during our overlap in the group. Special thank you to Dr. Daniel Shy for being my writing buddy, challenging my thought process, and providing valuable feedback along the way. Also a special thank you to Alex and Sara for your review of my thesis. Thanks to Zhuo, Matt, Damon, Jim Berry, and Hao Yang of H3D who have aided in the success of many of my experimental setups. Hao, our discussions have helped shaped much of the research in this work, thanks.

I would also like to highlight the people in the NERS department, outside of my research group, who have played key roles in my success at the University of Michigan. First, to the late and great Professor Emeritus Ronald Fleming, I am indefinitely indebted to you for the progression of my research. Your presence and excitement for students learning will truly be missed. The administration and staff, especially Jennifer, Garnette, and Peggy, thank you for all that you've done, even the little things that go unnoticed. To Cherilyn Davis, thank you so much for always having my back, for being one of the first friendly faces I met at UM, I am forever grateful for you. To the Women in NERS group, newly and aptly named WinNERS, thank you all so much for allowing me to bring my authentic self to the group and leading you all in the best way I knew how, I truly cherish our discussions, lunches, and social events. A special thank you to Dr. Ciara

Sivels for your friendship and for being a shining example in the NERS department and Lauren Finney for being so supportive along the way.

To all of my Ann Arbor friends and family, I can never truly express to you all how much you have meant to me over the past five years. I cherish every laugh, happy hour, rant, brunch, and meme we have shared. Thank you all for being such an amazing group of people. I love you all dearly, especially my *RMF Family*.

My writing group, *Moving Phoward*, thank you ladies for keeping me active in my research through a global pandemic! I'm not sure I would have made the strides I did without your support, understanding, and friendship. Love you all, and I am forever thankful and inspired by each one of you.

I would like to especially highlight mentors that have known me since youth and have been by my side even today. Dr. Musa Danjaji and Dr. Kenneth Lewis, you both have been like father figures through this journey, words can never truly describe how much your guidance, teaching, and support means to me. To the late Mr. Tryciecky, thank you sir for being a friend and the first teacher to challenge me to think harder, think bigger, and think more.

Thank you to my core friends and extended family from my alma mater, South Carolina State University, and those since childhood. When I wanted to throw in the towel, your encouragement never failed to put a smile on my face and push me forward. To Dr. Crystal Green and Sam Cole, thank you for being like siblings to me, especially during my graduate experience, I owe you both more than you know. Liz and April, thank you for your sisterhood and for your always cheering me on every step of the way. Dr. Darian “D” James, since the beginning of our college careers you have been by my side, thank you sis, for everything. My besties, “baby cakes” Sean and “my Cinnabon” Marissa, the bond we share and your love me for me has made these last

5 years fly by, thank you both for everything...every little thing. The two of you are unmatched and irreplaceable. And to my late Aunt Debra, thank you for everything, I hope I've made you proud.

To my siblings, father, and mother, thank you for always believing in my potential. My siblings ("*my kids*"): Deloris, Maryah, and Jeremiah, thank you for being my why, constantly reminding me of my reason for the daily grind. And to my amazing mother, Mary White, there is not enough words to even scratch the surface of my gratitude to and for you, your peace, your prayers, and your guidance. You all have been my strong foundation through it all, love you.

Lastly, but certainly not least, none of this would have been possible without my Lord and savior Jesus Christ, for breathing new life into me. Thank you for molding me into the Valerie that I needed to be to complete the tasks you have called me to. For every tool you have given me, every person you have placed in my life, and every obstacle you have and will help me overcome, thank you. Throughout my PhD journey my faith in you has grown, and your love for me was and is still, unwavering. I'm so excited for what your future has in store for my life.

"Gee, we did it, let's leave this imprint. Just finished writing..."

- Onika Tanya Maraj, *All Things Go*

TABLE OF CONTENTS

DEDICATION.....	ii
ACKNOWLEDGEMENTS	iii
LIST OF FIGURES	ix
LIST OF TABLES	xv
LIST OF ABBREVIATIONS	xvi
ABSTRACT	xviii
CHAPTER	
I. Introduction	1
1.1 Compton Imaging	1
1.2 Motivation and Outline of This Work	4
II. Basis of CdZnTe Detection and Near Field Imaging	7
2.1 Shockley-Ramo Theorem	8
2.2 Detector Characteristics	9
2.2.1 CZT Detection Systems Used in This Work.....	11
2.2.2 Performance and Limitations.....	14
2.3 Near Field Imaging Model.....	15
2.3.1 Source Distribution in a Near Field Imaging Space	16
2.3.2 Performance and Limitations.....	17
2.4 Imaging Reconstruction Modalities or Methods-Add References.....	20
2.4.1 Inverse Reconstruction Methods.....	20
2.4.2 Iterative Methods	21
III. Proton Radiation and Therapy	23
3.1 History of Hadron Therapy	23
3.2 Proton Beam Radiation	26
3.2.1 Proton Interactions with Matter	27
3.2.2 Bragg Curve Characterization.....	28
IV. LM-MLEM for Prompt Gamma Ray Imaging	43
4.1 Introduction.....	43
4.2 Derivation of List-Mode Maximum Likelihood Expectation Maximization	45
4.2.1 Expectation	47
4.2.2 Maximization	48
4.3 Application for High-Flux and High-Energy Gamma-Ray Scenarios.....	49
4.3.1 High Energy and High Flux Source Imaging Using LM-MLEM.....	50
4.5 ROI-MLEM	63
4.5.1 Background Constant.....	66
4.5.2 Comparative Analysis of Standard MLEM and ROI-MLEM	68
V. Proton Beam Range Verification Methods	78
5.1 Motivation.....	78
5.2 Prompt Gamma Correlation to the Proton Beam.....	79

5.2.1	Thick Target Yield Approximation Derived from Threshold Energy	80
5.2.2	Spatial Distribution Analysis	85
5.2.3	Spectral Analysis	101
5.2.4	Analysis Summary	107
5.3	Verification Method I: 718 keV Imaging	108
5.3.1	Bragg Peak Fit for High Threshold Energy Prompt Gammas	110
5.3.2	Experimental Analysis	113
5.4	Verification Method II: 4.44 MeV Imaging	120
5.4.1	Simulation Analysis	121
5.4.2	Experimental Analysis	122
5.4.3	Analysis Summary	127
VI.	CZT Detector Considerations for the Improvement of Prompt Gamma Ray	
	Detection	130
6.1	Introduction.....	130
6.2	Analog and Digital Systems for Prompt Gamma Ray Detection	131
6.2.1	Simulation Analysis	132
6.2.2	Experimental 4.44 MeV Detection Analysis	137
6.2.3	Experimental Prompt Gamma Detection Analysis	143
6.3	Large Array CZT (H3D-J) for Prompt Gamma Detection	150
6.4	Conclusion	155
VII.	Summary and Future Considerations.....	156
7.1	Benefits and Limitations of Using CZT for Proton Beam Range Verification	156
7.2	Future Work	159
7.2.1	Detection Efficiency Improvements through Detector Geometries.....	159
7.2.2	Alternative Imaging Methods	161
7.3	Other Applications of This Work	162
BIBLIOGRAPHY	164

LIST OF FIGURES

Figure 1.1: Gamma-ray Compton scattering interaction with an electron at rest.	2
Figure 1.2: A Compton cone reconstruction from two interaction sites of the incident gamma ray as depicted in Figure 1.1. The first interaction occurs at the position where the deposits E_1 to the recoil electron and the second interaction is where the photon is absorbed depositing the rest of its energy, E_2	3
Figure 2.1: Example of the weighting potential profile with respect to the cathode and a single anode pixel.	10
Figure 2.2: H3D J system.	12
Figure 2.3: M400 detection system.	13
Figure 2.4: H3D S400X system.	13
Figure 2.5: 2-D 4π image reconstructions of a Cs^{137} check source at varying image frame radii.	18
Figure 2.6: 1-D profiles along the peak intensity in the (a) azimuthal and (b) polar directions of each image reconstruction shown in Figure 2.6. The dotted black line represents the true source location. (c) FWHM versus image frame radius.	19
Figure 2.7: SBP reconstruction of increasing number of Compton rings. Note the improvement of the source location with increasing overlap of events.	21
Figure 3.1: Illustration by the University of Florida Proton Therapy Institute of the cyclotron used to accelerate hydrogen atoms for use in three separate gantries.	25
Figure 3.2: Treatment plan comparison using proton beam therapy (left) and x-ray therapy (right) for gastric cancer, studied by Dionisi et al.	26
Figure 3.3: Illustrations of proton interactions: (a) Ionization of the target atom through Coulombic interactions, (b) Elastic scattering due to the repelling forces of the atomic nuclei and the proton, (c) Inelastic scattering causing secondary particle emission, (d) Nuclear absorption of the primary proton. (p = primary proton, e= electron, n = neutron γ = gamma ray, α = alpha particle).	28
Figure 3.4: Mass stopping power and projected range curves calculated for three different materials. Bone equivalent plastic (solid line, $\rho=1.83 \text{ g/cm}^3$), Polyethylene (dashed line, $\rho = 0.97 \text{ g/cm}^3$), Tissue (dotted line, $\rho=1.03 \text{ g/cm}^3$)	32
Figure 3.5: Theoretical polyethylene (density = 0.97 g/cc) Bragg Curve for a 100 MeV proton beam.	33
Figure 3.6: TRIM simulation of 100 MeV protons in polyethylene and the associated mean range and straggle of the beam intensity.	36
Figure 3.7: Cumulative total dose from 6 beam pulses to create a spread out Bragg peak, SOBP [47].	37

Figure 4.1: (a) SBP and (b) LM-MLEM reconstructions of the same 10,000 photopeak events from experimental Cs ¹³⁷ data.	49
Figure 4.2: 4.44 MeV photopeak image reconstructions from an experimental PuBe source measurement (left column) and Geant4 simulations (right column). Both reconstructions use 5000 photopeak events. Shown are iterations 1 (a and d), 10 (b and e), and 20 (c and f).	53
Figure 4.3: MLEM reconstruction of a truncated imaging space using the 718 keV photopeak in a 60° × 60° FOV. The image is turned axially to show the image in depth accentuating the corner artifacts (right column).	56
Figure 4.4: MLEM reconstructions of truncated imaging spaces using the 718 keV photopeak. The 10 outermost pixels are removed along the edges of the 60° × 60° imaging space, reducing the FOV to 57.8° × 57.8°. (<i>Proton beam profile enters the target with respect to the image from top to bottom</i>)	57
Figure 4.5: (a) The 1st iteration of a4π MLEM image reconstruction of 4.44 MeV photons from experimental PuBe data. (b) The back projection of all Compton rings in the 4π space, developed using (4.14), prior to reconstructing the first iteration. (c) The back projection in a truncated 60° FOV of all Compton rings that intersect the FOV outlined by the dotted green line in (a). (d) A line plot of the intensity along the first row each back projection shown in (c), highlighting the sharp corner convergence at 62° and 122°	59
Figure 4.6: (a) A 2-D histogram of the forward projection value calculated using (3) for each Compton ring reconstructed in 4π shown in Fig. 1(a). (b) A 2-D histogram of the forward projection value of all Compton rings intersecting the truncated 60° FOV. The forward projection value is binned in the azimuthal and polar directions for each pixel that the Compton ring intersects. All blacked out regions indicate that zero of the Compton rings resulted in a forward projection value of that magnitude in the respective pixel locations.	63
Figure 4.7: (a) 1 st LM-MLEM iteration of the background FOV which is multiplied by the (b) apodizing cos ² mask that smoothly transitions to the ROI where all pixel values go to zero in the (c) masked background projection.	66
Figure 4.8: Exaggerated Cosine Apodizing Mask	67
Figure 4.9: (a) 4π image reconstruction, (b) LM-MLEM, (c) LM-MLEM with the outermost 10 edge pixels removed, and (d) ROI-MLEM, 22 nd iteration reconstructions of a simulated 10 cm Cs ¹³⁷ line source. (e) and (f) compares the FWHM values in the Y and X directions, respectively of (c) and (d) reconstructions, for both imaging algorithms, and (f) compares the SNR values for 50 iterations of both methods.	69
Figure 4.10: ROI-MLEM reconstructions of the Cs ¹³⁷ shifted source measurement. (a) No Shift, (b) 3 mm shift, (c) 5 mm shift, (d) 10 mm shift.	72
Figure 4.11: 1-D profiles through and Gaussian fit of the peak centroids in the X (a) and Y (b) directions for the image reconstructions shown for the Cs ¹³⁷ shifted source measurement. (c) and (d) shows the top 50% of the intensity normalized by the peak value in the X and Y directions, respectively.	73
Figure 4.12: PuBe source measurement setup.	74

Figure 4.13: Single module events energy spectra from PuBe measurements. The 4.44 MeV photopeak and escape peaks are focused on in the spectra to the right.	75
Figure 4.14: ROI-MLEM image reconstruction of the 4.44 MeV photopeak from Mod 0 for both the left and right positions of the PuBe source.	75
Figure 4.15: 1-D Slice through the peak centroid of both ROI-MLEM reconstructions shown in Figure 4.12.	76
Figure 5.1: Threshold depth estimate based on the 22.1 MeV threshold energy of the $^{12}\text{C}(p, x)^{10}\text{B}^*$, 0.718 MeV emission. The materials estimated are HDPE ($\rho=0.97 \text{ g/cm}^3$), Bone Equivalent Plastic ($\rho=1.82 \text{ g/cm}^3$), Tissue ($\rho=1.03 \text{ g/cm}^3$).	84
Figure 5.2: $^{12}\text{C}(p, x)^{10}\text{B}^*$, 0.718 MeV Cross-section experimentally given by Kozlovsky [61] . Fitted with a 4 th degree polynomial.	85
Figure 5.3: Schematic of MCNP6 simulations of various low Z targets and a 0.25 cm radius proton pencil beam incident from the central -x axis.	87
Figure 5.4: 3-D Distribution for HDPE (top row), BEP (middle row), and Tissue (bottom row) targets simulated in MCNP6. The intensity bar corresponds to the number of tracks tallied in each voxel. The 3-D target is truncated for the gamma and proton tracks in the X direction to 10 cm.	88
Figure 5.5: Neutron dose calculated by MCNP6 using a F6 tally, as a function of proton beam energy.	89
Figure 5.6: 2-D neutron mesh tally profile simulated in MCNP6	90
Figure 5.7: 2-D gamma mesh tally profile simulated in MCNP6.	91
Figure 5.8: 2-D proton mesh tally profile simulated in MCNP6	92
Figure 5.9: 1-D profiles along the central beam axis of the photon and proton intensity.	93
Figure 5.10: Schematic of the HDPE using <i>PGCCS</i>	95
Figure 5.11: 2-D distribution of gamma rays emitted from nuclear reactions induced by protons, neutrons, and ions within the HDPE target. The intensity bar corresponds to the number of photons emitted in the voxel (0.5 cm^3)	96
Figure 5.12: 1-D distribution of the 4.44 MeV, 718 keV, and 511 keV depth profile along the proton central axis as a function of proton beam energy in the HDPE target simulated in <i>PGCCS</i>	98
Figure 5.13: 1-D distribution of the 4.44 MeV, 718 keV, and 511 keV depth profile along the proton central axis as a function of proton beam energy in the BEP target simulated in <i>PGCCS</i>	99
Figure 5.14: 1-D distribution of the 4.44 MeV, 718 keV, and 511 keV depth profile along the proton central axis as a function of proton beam energy in the tissue target simulated in <i>PGCCS</i>	100
Figure 5.15: MCNP6 gamma-ray energy spectra from proton beam irradiation of the HDPE target.	102

Figure 5.16: MCNP6 gamma-ray energy spectra from proton beam irradiation of the BEP target.	102
Figure 5.17: MCNP6 gamma-ray energy spectra from proton beam irradiation of the tissue target.	103
Figure 5.18: Polaris J3 recorded energy spectra of the HDPE Simulation up to 5 MeV. Bottom figures show the 718 keV (left) and the 4.44 MeV (right) photopeaks.	104
Figure 5.19: 3-D distributions of the originating locations of the 4.44 MeV (red) and the 718 keV (blue) photons within the HDPE target that were detected by the Polaris J3 system. The bottom right figure shows the number of emitted 718 keV and 4.44 MeV photons for each proton beam energy.	105
Figure 5.20: 1-D Profile of the 718 keV and 4.44 MeV photon emission within the simulated HDPE target with respect to the Bragg curve for each beam energy within a C ₂ H ₄ target calculate by SRIM. The bottom left figure shows the peak difference between the 718 keV and the 4.44 MeV profiles with respect to the Bragg peak, respectively.	107
Figure 5.21: Comparison of the <i>PGCCS</i> 718 keV peak location to the SRIM2008 calculate depth at which the proton beam reaches 22 MeV.	111
Figure 5.22: Comparison of the 718 keV peak and stop depths recorded from PGCSS to the SRIM2010 calculated Bragg peak locations for an HDPE target.	112
Figure 5.23: Proton beam measurement setup for the analog and digital systems. The top image shows the 30 cm separation setup, and the bottom figure shows the 96 cm separation measurement setup. (The green cross on the HDPE Block indicates the location of the proton beam entrance.)	113
Figure 5.24: ROI-MLEM image reconstructions of the 718 keV photopeaks from measurements AM 9-12. The pixel resolution averages 0.025 cm ² . The red line indicates the distal fall-off of the proton beam and the green line represents the trajectory of the beam, the green arrow indicates the direction.	115
Figure 5.25: 1-D profile comparison of the 718 keV image reconstructions for measurements AM 09-12.	116
Figure 5.26: ROI-MLEM image reconstructions of the 718 keV photopeaks from measurements AM 13 an AM14. The pixel resolution averages 0.025 cm ² . The red line indicates the distal fall-off of the proton beam and the green line represents the trajectory of the beam, the green arrow indicates the direction.	117
Figure 5.27: 1-D profile comparison of the 718 keV image reconstructions for measurements AM 13 and AM 14.	118
Figure 5.28: Estimation of the incident proton energy and threshold depth from the peak positions of the 718 keV image reconstructions for the M400 AM measurements.	119
Figure 5.29: Simulation of the 4.44 MeV gamma ray distribution within a HDPE target.	121
Figure 5.30: Proton beam measurement setup using the Polaris J3 (black) detection system at the MPTC with a 12.5 cm × 12.5 cm × 5 cm HDPE target (blue). The patient bench is shown in gray. <i>Not drawn to scale.</i>	123

Figure 5.31: 4π image reconstructions of the 4.44 MeV photopeak (highlighted in red) using standard MLEM.	124
Figure 5.32: ROI-MLEM reconstruction of the 4.44 MeV photopeak. The image reconstruction is truncated to the size of the target profile. The green dotted line indicates the trajectory of the beam upward from the negative y-direction and the red dotted line indicates the beam's end point. The 1-D slice profile is taken from the values along the y-direction through the peak centroid of the image reconstruction.	125
Figure 5.33: $90^\circ \times 90^\circ$ ROI image reconstructions with a 0.02 cm^2 pixel resolution of the (a) 4.44 MeV and (b) 718 keV prompt gamma rays. (c) A 1-D slice is taken through the peak centroid of each image to show the profile of the events along the beam path. This is compared to the (d) simulated Bragg curve of a 70 MeV proton beam incident on a C_2H_4 target ($\rho = 0.97 \text{ g/cm}^3$). ..	128
Figure 6.1: Geant4 simulation of two 2×2 CZT arrays with 11 cm separation, 30 cm away from a 4.44 MeV source.	132
Figure 6.2: Recorded energy spectra from 4.44 MeV Geant4 simulation comparing the spectrum of all recorded events to the spectrum of coincidence events.	133
Figure 6.3: Recorded energy spectra from 4.44 MeV Geant4 simulation for each CZT array independently recorded events.	134
Figure 6.4: (a) Interplanar interaction distribution of each coincidence event as a function of energy. (b) Non-interplanar interaction energy distribution for each plane's independently recorded events.	135
Figure 6.5: ROI-MLEM image reconstruction of the Geant4 simulated extended 4.44 MeV source, with the expected distribution outlined in green.	137
Figure 6.6: PuBe source experimental setup.	138
Figure 6.7: PuBe measurement energy spectra results. (a) Recorded coincidence energy spectrum. (b) Recorded single events energy spectra. (c) Single events energy spectra with special attention to the 4.4 MeV and 6.1 MeV photopeaks.	139
Figure 6.8: 511 keV event distribution across all crystals in (a) Module 0 and (b) Module 1 ...	141
Figure 6.9: 4.44 MeV photopeak image reconstruction from the combined single event spectrum using ROI-MLEM.	143
Figure 6.10: S400X Non-interplanar spectra for each proton beam measurement.	145
Figure 6.11: 3-D plot of all events recorded for measurement 10 in the M400 systems: (a) System 1 on the left and (b) System 0 on the right.	146
Figure 6.12: Recorded energy spectra for Measurement 10 for both M400 systems	147
Figure 6.13: Recorded energy spectra for proton beam measurement 9 for both M400 systems	147
Figure 6.14: Recorded energy spectra for Measurement 13 for both M400 systems	148
Figure 6.15: Energy spectra for Measurement 13 separated by number of interactions for one M400 system.	149

Figure 6.16: Experimental setup of the H3D J system for four different beam measurements: (a) small HDPE tube shielded by lead, (b) a large HDPE tank, (c) unshielded HDPE tube, (d) a large water bottle. Each target is centered above H3DJ which is attached to the underside of the patient bench.	151
Figure 6.17: Raw recorded energy spectra for the H3D-J measurements.	152
Figure 6.18: Recorded energy spectra range: 1250 keV – 2300 keV.	153
Figure 6.19: High energy spectra from H3D-J measurements.	154
Figure 7.1: Simulated CZT detection geometries: (a) “H3D-J” configuration of 64 crystals, (b) “Square” configuration of 64 crystals and four planes, (c) “Triple” configuration of 27 crystals and three planes, (d) “Long” configuration of 64 crystals, 2×8 crystals per plane for four planes.	159
Figure 7.2: Full energy absorption efficiency calculated for each geometry at 2.31 MeV, 4.44 MeV, and 6.10 MeV. Blue: H3D-J, Purple: Long, Red: Square, Green: Triple	160

LIST OF TABLES

Table 3.1: Expected proton induced reactions on ^{12}C and ^{16}O	40
Table 4.1: Time to reconstruct the first iteration of the same photon data for varying FOV sizes.	55
Table 4.2: Comparison of the SNR and FWHM of the image reconstructions developed using LM- MLEM and ROI-MLEM of the 10 cm Cs^{137} line source simulation. The FWHM error is taken as twice the pixel pitch.	70
Table 4.3: Source distribution location estimation based on the peak centroid location in the x- direction of the 1D profiles of the image reconstructions shown in Figure 4.11.....	72
Table 4.4 Computation performance comparison of the time to reconstruct the 1 st iteration.....	77
Table 5.1: Elemental composition of Simulated Targets.....	86
Table 5.2: Summary of Beam Measurements at 30cm Separation Distance kMU = kilo-Monitor Units.....	114
Table 6.1: Comparison of recorded peak events for the 4.44 MeV gamma-ray.....	140
Table 6.2: Distribution off all events recorded by both modules for each crystal.....	142
Table 6.3: Proton Beam Measurements specifications. Red: M400 specific, Blue: S400X specific	144

LIST OF ABBREVIATIONS

ASIC Application-Specific Integrated Circuit

BEP Bone Equivalent Plastic

BKR Bragg-Kleeman Rule

BNCT Boron Neutron Capture Therapy

CZT Cadmium Zinc Telluride

EIID Energy-Imaging Integrated Deconvolution

FBP Filtered Back Projection

FWHM Full Width at Half Maximum

FOV Field of View

G4 Geant4

HDPE High Density Polyethylene

LET Linear Energy Transfer

LM-MLEM List-Mode Maximum Likelihood Expectation Maximization

MLEM Maximum Likelihood Expectation Maximization

MPTC Maryland Proton Therapy Center

PET Positron Emission Tomography

PGCCS Prompt Gamma Compton Camera Simulation

PSF Point Spread Function

RBE Radiobiological Effectiveness

ROI Region of Interest

ROI-MLEM Region of Interest Maximum Likelihood Expectation Maximization

SBP Simple Back Projection

SPECT Single Photon Emission Computed Tomography

SRIM Stopping and Range of Ions in Matter

TRIM Transport of Ions in Matter

ABSTRACT

The viability of 3-D position sensing CdZnTe (CZT) semiconductor, high-resolution, gamma-ray spectrometry imaging systems have impacted a wide array of nuclear applications. The high performance of CZT at room temperature ($<1\%$ FWHM at 662 keV) and position sensing capabilities allows for high fidelity Compton imaging applications for 3-D event reconstruction of radioactive sources. Current improvement in this technology has allowed for research in its application of high-flux and high energy (>1 MeV) gamma ray scenarios, particularly prompt gamma ray detection and imaging for proton beam radiotherapy.

Proton therapy is proving to be an advantageous treatment option for cancerous tumors, as the charged particle has a finite range which can aid in sparing at risk organs from unnecessary dose. However, uncertainty arises in determining the absolute range of the proton within a patient. This uncertainty can be detrimental in the treatment planning for radiation oncologist, as the safety margins around the treatment volume must be well understood, to spare healthy organs that could be at risk due to their proximity to the tumor. Therefore, real-time range and dose verification is sought after, as it is vital in capitalizing on the advantages of proton therapy safely and effectively.

This work presents the use of a digital and analog application-specific integrated circuits (ASICs) CZT systems and their feasibility in the detection of the prompt gamma rays that are emitted from high-energy proton beams incident on various low Z targets. Through simulation we study the spectral features of proton beam interactions in bone equivalent plastic, high density polyethylene, and normal tissue targets and correlate these features to data retrieved experimentally from high density polyethylene targets used for irradiation measurements.

The list-mode maximum likelihood expectation maximization (LM-MLEM) image reconstruction method is used to develop an ROI (region of interest) MLEM approach to mitigate the effects of noise artifacts in the image space and computational expense, by truncating the image space used for image reconstruction.

This work intends to provide an imaging approach via ROI-MLEM to proton beam range verification (PBRV). ROI-MLEM capabilities are tested by imaging gamma-ray sources with emission energies below and above 1 MeV and has shown to be able to separate sources to the order of a centimeter with sub-millimeter pixel resolution. The limitations of imaging are studied by understanding the detection limitations of the CZT systems employed for experimental analysis in this work. The S400X, M400, and H3D-J systems, all CZT detector systems provided by H3D Inc. are assessed in their performance of high energy and high-flux gamma ray detection. Proton beam measurements with the M400 and H3D-J systems are used for prompt gamma-ray imaging analysis of the 718 keV photon and the 4.44 MeV photon, both emitted from carbon-proton interactions in the plastic target. The imaging analysis of these photons show the current state of CZT and ROI-MLEM performance and the possible reasons for uncertainty in the beam range estimation. Lastly, we discuss the considerations of CZTs limitations and advantages in this application and the potential for improvement in both detection and imaging. This work intends to provide an introductory assessment of CZT's use for PBRV, with the future goal of achieving millimeter accuracy in determining the Bragg peak location of the proton beam from prompt gamma ray imaging, in real time.

CHAPTER I

Introduction

1.1 Compton Imaging

Photons, or x-rays and gamma rays, have a long history of being particularly useful in visualizing unseen objects through probing methods and identifying those that are radioactive through their emission. In this text we focus on the gamma-ray, which is emitted from the nucleus of an excited atom or a radioactive isotope. The gamma-ray can undergo mainly three types of interactions: photoelectric absorption, Compton scattering, and pair production, all of which has a dependency on the energy of the photon. Of the three methods, the Compton scattering mechanism, named after Nobel Prize (1927) winner Arthur H. Compton, can provide a method of using the angular information between each scatter site of the photon to infer an estimate of its originating location[1].

A photon with an initial energy of E_0 interacts with an electron, transferring part of its energy to the recoiled electron (E_I), and then scattering away with some residual energy, E_2 , at an angle θ as shown in Figure 1.1.

With the initial energy, E_0 , and the scattered photon energy E_2 , the deposited energy, E_I , can be obtained from simple subtraction. Thus the scattering angle can then be calculated using the Compton scattering formula,[1]

$$\cos(\theta) = 1 - \frac{m_e c^2 E_1}{E_0 E_2} \quad (1.1)$$

employing the rest mass energy of the electron, $m_e c^2$.

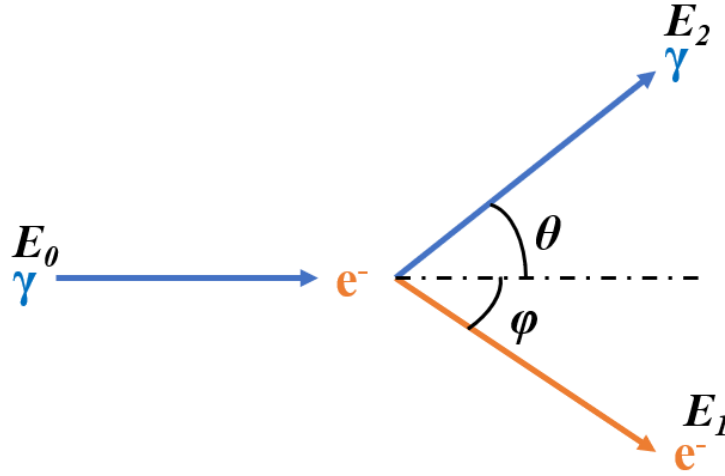


Figure 1.1: Gamma-ray Compton scattering interaction with an electron at rest.

If the scattered photon goes on to be photoelectrically absorbed at some location, knowing the positions of this absorption site, $P(\overline{E_2})$, and the location of the first interaction with the electron, the direction of the incident photon can be contained to the surfaces of the Compton cone provided some uncertainty from the position estimate of each interaction site. Figure 1.2 shows the estimated Compton cone that provides a Compton ring of the possible incident photon's originating location.

Using the directionality provided by the Compton ring allows us to reconstruct the source distribution in space as a radiation image via Compton imaging.

Detecting photons for Compton imaging has long been used to describe the nature of radiation in space and was first described by Lale in 1959 in a medical application, inspiring work for Compton scatter radiography using x-rays [2], [3]. Compton imaging has gone on to prove to be useful in a wide array of applications, especially medically, in practices such as PET (positron emission tomography) and SPECT (single photon emission computed tomography) imaging [4]–[7]. Various systems have also been employed for non-destructive assay of materials which probes an unknown material via the collection of back scattered photons from a photon emitting source

and detection system to one side of the intended target [8], [9]. Coded Aperture Imager (CAI), pixelated Compton imagers, and Compton telescopes which employ multiple layers of the detection medium to record multiple scatters and the absorbing interaction in the last layer, are all attractive modes of Compton imaging that employ unique mechanisms to record the Compton interactions for imaging in applications such as astrophysics [10], [11].

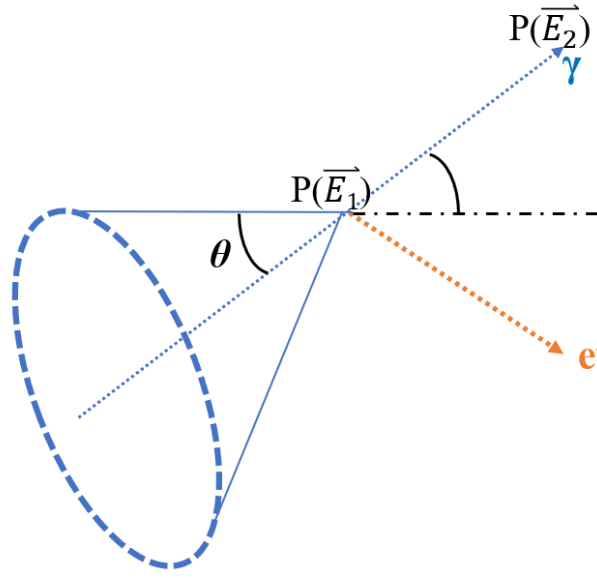


Figure 1.2: A Compton cone reconstruction from two interaction sites of the incident gamma ray as depicted in Figure 1.1. The first interaction occurs at the position where the deposits E_1 to the recoil electron and the second interaction is where the photon is absorbed depositing the rest of its energy, E_2 .

The challenge in each domain has consistently been the assay of high energy photons whose probability of Compton scattering wanes as its more likely to undergo pair production which skews the Compton ring estimate.

In the Orion research group, great strides have been made by past researchers in the realm of Compton imaging. For example, Zhang et al. demonstrated that 3-D position information of multiple gamma-ray interactions in a single semiconductor pixelated CdZnTe detector, can be

ascertained by measuring the drift time of the recoil electron clouds with an improved application-specific integrated circuit (ASIC) design [12]. Lehner et al shows the capability of 4π Compton imaging, achieving less than 30° angular resolution, imaging 662 keV photons emitted from a Cesium-137 source using a single CdZnTe crystal detector ($15 \times 15 \times 10 \text{ mm}^3$) [13]. Xu and Chu have both worked on the advancement of imaging algorithms for CZT detection specific Compton imaging problems, developing methods such as LM-MLEM (list-mode maximum likelihood expectation maximization), FBP (filtered back projection), EIID (energy imaging integrated deconvolution) [14], [15]. Whereas other researchers such as Goodman and Jaworski demonstrated various applications of Compton imaging in a wide array of scenarios, such as moving sources, and shielding material identification [16][17]. Most recently, Shy developed methods to mitigate noise artifacts from super MeV photons in Compton imaging[18].

1.2 Motivation and Outline of This Work

3-D position sensitive CZT has shown its capability to provide quick and accurate information of radioactive sources in both position and energy, providing a means of imaging allowing for both source localization and identification. Currently, research is pushing the bounds of CZT's limitations at high energies and under high saturation levels of extremely radioactive sources.

This work intends to show an understanding of CZT imaging and detection performance in the arena of proton beam range verification (PBRV) for the use of cancer therapy.

PBRV is a growing research field in medical physics, where the goal is to provide real time analysis of the proton beam trajectory and dose profile within the patient. In doing so, uncertainty in the dose distribution can be minimized potentially saving nearby healthy organs and tissue of the tumor being treated via proton irradiation.

As the highly energetic proton travels through the patient, or any material, it can undergo many different interactions with the atoms along its path, causing excitation of the nuclei along the way. This excitation will lead to the emission of gamma-rays ranging in energy up to 15 MeV on an average timescale of femtoseconds, we term these photons as prompt gammas (PG). The PG emission of a standard dose pencil beam of protons can range anywhere from tens of thousands to millions of photons per second, creating a very high flux environment. The job of CZT in this case is to detect these photons, then image, and provide a means of correlating the PG emission to the proton beam profile. The imaging analysis particular objective here is to estimate the Bragg peak location with great precision, as this corresponds to the single point at which most of the dose is deposited.

In this work we aim to provide a foundation in the understand of proton beam therapy and the implementation of CZT for use in beam range verification. In chapter 2 we discuss the physics behind CZT and the imaging model, along with the three CZT systems employed in this foundational effort. Chapter 3 will then give a brief overview of the history of proton radiation and therapy and some of the key physics behind the dose profile of the proton beam. Chapter 4 follows the physics of CZT and proton therapy with the derivation of the imaging algorithm used in this work, LM-MLEM. Here we will also discuss the development of ROI-MLEM specifically designed to aid in overcoming some of the limitations of CZT in imaging high energy photons, with high resolution in a timely manner. Chapter 5 follows up by using ROI-MLEM for two methods of estimating the proton beam profile using two distinct PG emission photons from carbon-proton interactions. The 718 keV photon and the 4.44 MeV photon are both PG that are derived from two different modes of interactions between the proton and carbon nuclei (discussed in Chapter 3) which could lend different information about the profile of our beam. Experimentally

the work takes a first order approach to difficulty focusing on single-pencil beam proton irradiations of a homogeneous C_2H_4 plastic target. Chapter 6 discusses some considerations of the limitations of CZT in the application of PBRV and areas where there is room for improvement based on the findings in this work. Lastly, chapter 7 will summarize the efforts shown in this thesis of using CZT in the application of PBRV via imaging prompt gammas and the many ways future researchers can build upon the foundation provided here.

CHAPTER II

Basis of CdZnTe Detection and Near Field Imaging

To obtain a precise estimate of the radioactive source distribution in space, whether it be informative in the two-dimensional or three-dimensional frame, the detection parameters set for locating the source must provide information that can be leveraged for calculating the originating location of the incident gamma-ray. There are many materials employed today to detect and locate, radioactive photon emitting sources such as, gas chambers, liquid or plastic scintillators, and solid-state semiconductors[19][20]. For this work, room temperature operated, solid-state semiconductor crystals, CdZnTe (CZT), are employed as the detection medium. The compact design of pixelated CdZnTe based detection system allows for position-sensitive signal readout of the energy deposition as the photons interact within the crystal[21]. The provided signal can be further analyzed to estimate the origin of the photon via various imaging modalities.

The imaging space studied for the particular use in this work is in the near field of the detector system, that is to say, the radioactive source is expected to be within range of the detector ($< 1\text{m}$ spacing between source and detection system for this work) such that the detection geometry needs to be especially considered for image reconstruction. Thus, there are some assumptions that will not stand given the nature of the photons being emitted from a source near the detection system.

2.1 Shockley-Ramo Theorem

The foundation of the Shockley-Ramo theorem is that the moving charge within a detection medium induces charge on the electrodes of the detector and thus can be isolated and estimated [22]. The theorem provides a simplistic way of theorizing pulse shapes of the induced signal, which can provide information about the interaction location of the incident particle and the energy deposited within the detection medium.

For a moving charge, q , the Shockley-Ramo theorem states that the charged induced on the electrode, Q , is

$$Q = -q\varphi_0(x), \quad (2.1)$$

where $\varphi_0(x)$ is the unitless weighting potential profile of the negatively induced charged by the moving charge carrier. The same could also be said for the current, i , induced on the electrode,

$$i = qv \cdot E_0(x), \quad (2.2)$$

where v is the instantaneous velocity and $E_0(x)$ is the weighting field created within the detection system between electrodes. The weighting potential and the weighting field define the potential and field that would theoretically exist at the moving charge carrier with respect to the electrode of interest.

The weighting potential can also be leveraged to have a profile driven by the detector geometry and the specified electrode. Applying Green's first identity allows for the follow conditions:

$$E = -\nabla\varphi(x) \quad (2.3)$$

$$\text{Boundary Condition 1: } \varphi_1|_s = 0 \quad (2.4)$$

$$\text{Boundary Condition 2: } \nabla^2\varphi_0 = 0 \quad (2.5)$$

The first condition states that the electric field within the medium is the equivalent of the negative flux of the weighting potential field. The following boundary conditions contain the weighting potential to the volume of the detector. The first states that the weighting potential at the surface of the detector is zero due to the grounding of all other electrodes. The second boundary condition states that the volumetric flux of the weighting potential is equal to zero in the case of no charge distribution within the detector. Both terms equaling zero allows for the Shockley-Ramo theorem to be independent of space charge or externally applied bias. Employing the Shockley-Ramo theorem is valid in the case of multiple moving charges in one medium. Thus, the change in the charge induced on the electrode of interest, ΔQ , can be redefined as

$$\Delta Q = \int_{x_i}^{x_f} q E_0 dx = -q [\varphi_0(x_f) - \varphi_0(x_i)], \quad (2.6)$$

where the change in the induced charge is independent of the electric field caused by the applied bias voltage and space charges. Thus it is solely determined by the trajectory of the moving charge carries relative to the specified electrode. Therefore, if the weighting potential is known for a specific detector configuration the induced charged on any electrode can be easily calculated for multiple moving charges, even in complex designs.

2.2 Detector Characteristics

The detection systems used in this work are based on cuboid, semiconductor, pixelated CdZnTe crystals. CZT detection systems have been historically employed as a gamma-ray detector, as their large band gap of approximately 1.6 eV permits room temperature operation allowing for electrons to be excited to the conduction band as radiation interacts with the medium [19]. The CZT crystals used are approximately $22 \times 22 \text{ mm}^2$ and are either 10 mm or 15 mm thick. One of the square faces is a gold-plated planar cathode electrode and the opposite face consists of

an 11×11 array of anode electrodes. The signal from cathode and each anode electrode can be individually read out using its unique weighting potential profile, as shown in Figure 2.1, provides a means of determining not only the energy deposited but the location of the incident interaction as well.

The number of electron hole pairs created as the electrons are excited into the conduction band is proportional to the deposited energy of the incident photon. Coupling the energy deposition proportionality with the pixelated design provides multi-dimensional information from the photon interaction; energy, position (x , y , z), and timing. These characteristics of the detection design allows for high performance and advanced applications of CZT in various experimental radiation detection and imaging applications.

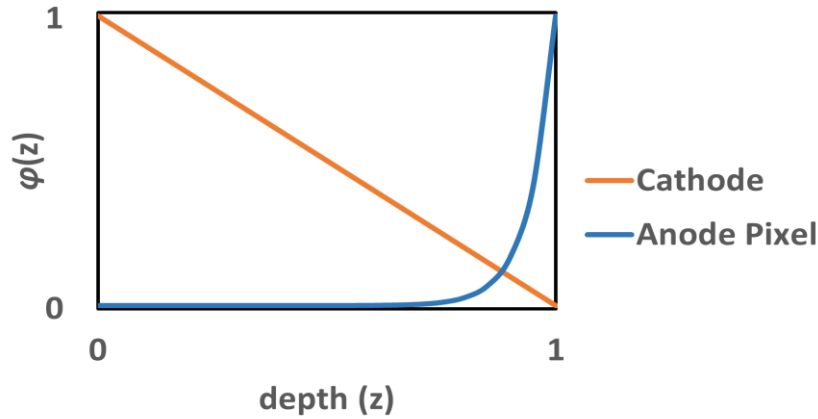


Figure 2.1: Example of the weighting potential profile with respect to the cathode and a single anode pixel.

With a high negative bias applied to cathode side of the CZT detector, the excited electrons are steered towards a single pixel anode inducing their full charge on the collecting pixel and transient charge on the neighboring pixels and cathode. The pixel anode that collects the full charge signal provides cartesian information in the x and y direction on the location of the originating interaction, with 1.72 mm pitch, or the size of the pixel. With the slope of the weighting potential

of the cathode signal being a function of the thickness of the detector crystal, a ratio of the induced signal on the cathode and collecting pixel anode provides depth of interaction information,

$$\frac{Q_c}{Q_a} = \frac{n_o e(Z)}{n_o e} = Z, \quad (2.7)$$

where n_o is the number of charge carriers and e is the charge of an electron. The charge induced on the cathode is a function of Z or depth into the detector, and Q_a is the charge induced on the collecting anode pixel which is proportional to the number of charge carriers.

2.2.1 CZT Detection Systems Used in This Work

In this work, three different CZT detection systems are employed for gamma-ray detection and imaging analysis. Each crystal is equipped with 121 anode pixels in a 11×11 array and a planar cathode, allowing for 3-D position sensing and energy read out. Each system is provided by H3D Inc. in Ann Arbor, MI [23]. More details about the basis of the design of these systems can be found in [24] [25].

2.2.1.1 H3D-J system

Figure 2.2 shows the schematic and detector housing of the H3D-J (formerly called *Polaris J3*) system which has two detection stages, each stage containing four modules, and within each module there are four CZT crystals in a 2×2 array. The modules in the first stage are comprised of crystals that are $2.0 \text{ cm} \times 2.0 \text{ cm} \times 1.0 \text{ cm}$ and the second stage modules are comprised of crystals that are $2.0 \text{ cm} \times 2.0 \text{ cm} \times 1.5 \text{ cm}$. This results in 64 total CZT crystals with a total active volume of 320 cm^3 , the largest detection volume CZT array system built by H3D Inc for research applications. The two detection stages are sandwiched together one on top the other with a 5 cm

separation distance between them. H3D-J employs 16 independent readout analog-based ASICs and uses a calibrated dynamic energy range of 50 keV to 3 MeV per detector pixel.

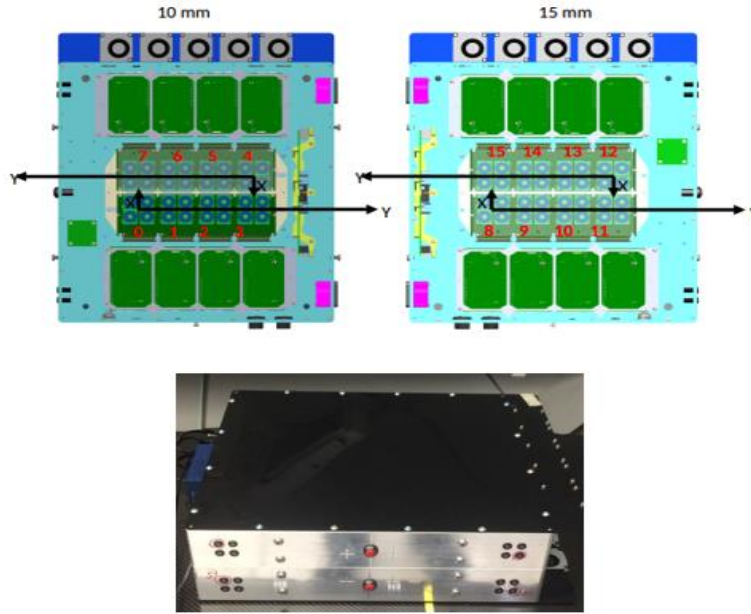


Figure 2.2: H3D J system.

2.2.1.2 H3D M400

The M400 is a modular compact design system housing only four CZT crystals in a 2×2 array. Each crystal is $2.0 \text{ cm} \times 2.0 \text{ cm} \times 1.0 \text{ cm}$ in dimension and employs an analog ASIC for signal readout. The compact design of these systems allows for easy maneuvering and block-style geometry building when using more than one system. They also provide the option to synchronize data collection such that coincidence events can be recorded across multiple systems. The dimensions of the M400 system shown in Figure 2.3 is $5.8 \text{ cm} \times 5.8 \text{ cm} \times 10.2$ and weighs 1.3 lbs.

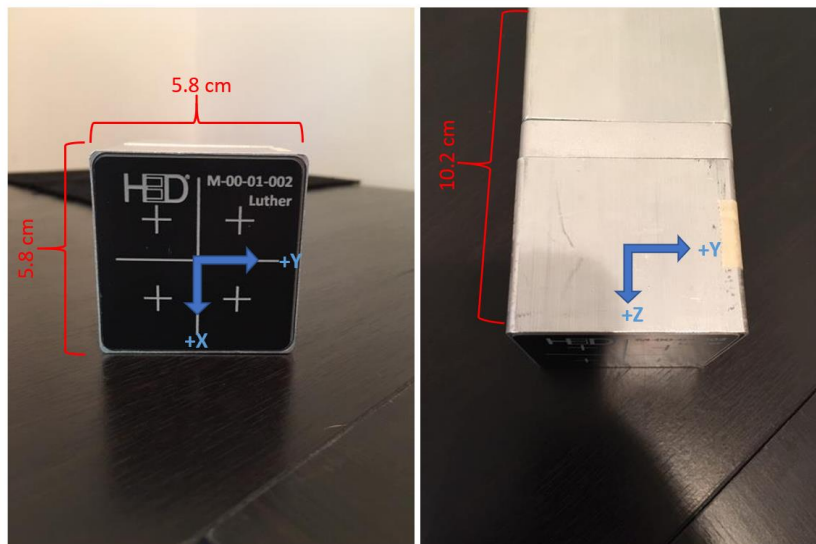


Figure 2.3: M400 detection system.

2.2.1.3 S400 X

The S400X system, shown in Figure 2.4, houses the same configuration of four CZT crystals like the M400 system but utilizes a digital direct attached ASIC for signal readout.

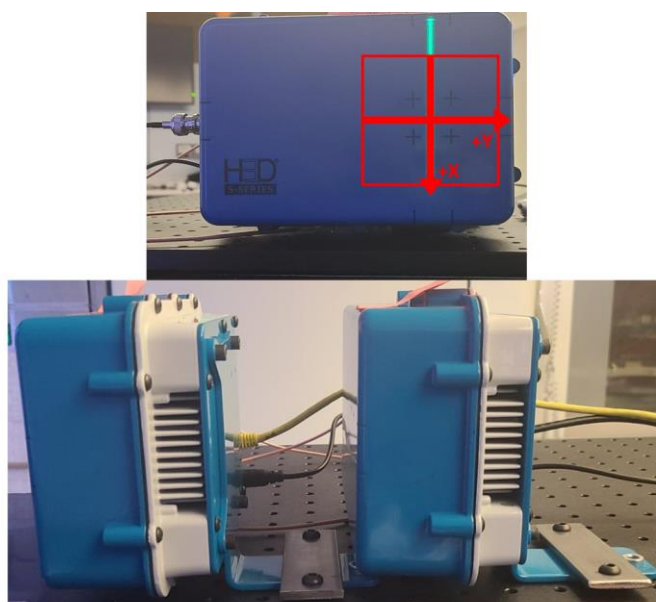


Figure 2.4: H3D S400X system.

This allows for a dynamic range energy calibration up to 9 MeV. Its outer design allows for a permanent mounting of the detector and is more robust in comparison to the M400, with dimensions of $9\text{ cm} \times 15\text{ cm} \times 21\text{ cm}$.

2.2.2 Performance and Limitations

Continual research over the past 50 years have led to strides in the improvement of CZT detection and imaging capabilities. Each of the systems described in this chapter have shown to be able to achieve about 1.1% full width and half maximum (FWHM) resolution at 662 keV. However, the majority of the CZT detectors developed in the Orion Research Group at the University of Michigan boasts a FWHM resolution of less than 0.5% [26].

Both the S400X and the M400 models allow for on-the-fly processing of all data collected, whereas the H3D-J system requires post processing to separate and filter the events. The timing resolution of all the systems are quoted as less than 500 ns. However, the digital ASICs employed in the S400x systems are about an order of magnitude slower than that of the analog ASICs employed in the M400 and H3D-J systems. The timing resolution of these systems can allow for high-activity source detection, processing events on the order of 10,000 (digital) to 60,000 (analog) cps (counts per second).

For imaging purposes, the spatial resolution of these system is a vital aspect. The analog readout ASIC system's spatial resolution is limited to 1.72 mm in both the X and Y direction which is the pitch of a single anode pixel. This spatial resolution is three times larger than the 0.5 mm Z axis depth resolution. To improve upon this, the digital ASICs can provide sub-pixel position sensing techniques [27]. This is achieved through analysis of the signal recorded from the transient signal induced on the neighboring pixels surrounding the collected anode pixel. Measuring the charge induced on these neighbor or non-collecting pixels is optimized through

digitized signal processing, pushing the spatial resolution within a pixel to 300 μm at 662 keV [28]. Thus, where the digital ASICs are hindered by timing, they provide a superior spatial resolution, when subpixel sensing is enabled, in comparison to the faster analog ASICs.

2.3 Near Field Imaging Model

Defining an imaging model will provide a base for solving any imaging problem that correlates observation data with ground truth information. It is typically impractical to derive an image directly without the collection of observations or measurements, provided a detection setup. Thus the relationship between the expected observation and the final image can be represented in matrix notation as follows:

$$\bar{\gamma} = \mathbf{T}\mathbf{f}, \quad (2.8)$$

where \mathbf{f} is the image vector of length J , such that $j \in \{1, 2, \dots, J\}$, $\bar{\gamma}$ is the expected observation vector of length I , where each element is a recorded observation event, $\bar{\gamma}_i = \bar{\gamma}[i]$. To provide a correlation between the expected observation and the final image, \mathbf{f} , the system matrix \mathbf{T} , is segmented into $I \times J$ system matrix of elements, t_{ij} . Thus the matrix form of this general imaging model will look like such:

$$\begin{bmatrix} \bar{\gamma}_1 \\ \bar{\gamma}_2 \\ \vdots \\ \bar{\gamma}_{I-1} \\ \bar{\gamma}_I \end{bmatrix} = \begin{bmatrix} t_{1,1} & t_{1,2} & \dots & t_{1,J-1} & t_{1,J} \\ t_{2,1} & t_{2,2} & \dots & t_{2,J-1} & t_{2,J} \\ \vdots & \vdots & \ddots & \vdots & \vdots \\ t_{I-1,1} & t_{I-1,2} & \dots & t_{I-1,J-1} & t_{I-1,J} \\ t_{I,1} & t_{I,2} & \dots & t_{I,J-1} & t_{I,J} \end{bmatrix} \cdot \begin{bmatrix} f_1 \\ f_2 \\ \vdots \\ f_{J-1} \\ f_J \end{bmatrix}. \quad (2.9)$$

The system matrix is a convolution of the parameters describing both the detector setup and the experimental probability of obtaining the expected observation. For the purposes of deriving an observation, from each event, i , in Compton imaging, each event will also hold a set of parameters describing the event within the system matrix:

$$i \rightarrow \{ E_1 R_1, E_2 R_2, \dots, E_{M-1} R_{M-1}, E_M R_M \}, \quad (2.10)$$

where E and R represent the energy and location of each interaction, m , respectively, for that event, i . Thus, for Compton imaging, t_{ij} , is the probability that the event, i , can be emitted from the image element, j .

2.3.1 Source Distribution in a Near Field Imaging Space

For practical computation, it is suitable to use a discrete or pixelated imaging space to characterize the source distribution, which is the expected number of photons emitted over an area. This allows for our image vector, f , from Eq. 2.8, to become a function of the source distribution, such that,

$$f[j] = f(x_j), \quad (2.11)$$

where x_j is the position of the source value, or intensity at the j -th image pixel, where $j \in J$.

There are a number of ways to define the image space to best suit the problem and detection setup. Most commonly, a spherical or cartesian coordinate system is used for localizing radioactive sources. Either system can be employed for 2-D imaging, and it is more feasible to employ the cartesian system for 3-D space imaging. Each method has their strengths and conditions before being employed for specific imaging problems [14]. In this work specifically, a 2-D spherical coordinate system is employed for imaging of sources within close proximity of the detection system, or near field.

Near field imaging implies that the distance between the source being observed and the detection system is too small to assume that the distribution of the photons attenuation into the detector is uniform. In a far-field scenario the space between the source and detection system is large enough such that the detector can be treated as a point detector. This difference in imaging

space with respect to Compton imaging corresponds to how we define the origin, or the vertex, of the Compton ring and how it is back projected. Under far-field approximations one can set the vertex of all reconstructed Compton cones to the center of the detection geometry. However, in the case of near field imaging this simplification does not hold, and the vertex of each Compton cone must be centered to the point of origin of the first interaction of each event as seen in **Error! Reference source not found.**

Setting the vertex of each event to the location of its first point of interaction will account for the attenuating effects of the detector near the source and correct for the depth of each interaction within the detector volume. Since near field imaging corrects for the originating interaction location within the detection medium the radial extent of the 4π spherical imaging frame must also be set as a focus distance such that the imaging frame intersects the source's true location.

2.3.2 Performance and Limitations

When employing a 2-D spherical coordinate system for near field Compton imaging the blurring or noise associated with the image reconstruction will be affected by the radial distance set as the extent of the imaging frame between the source and the detector. As the imaging frame deviates from the true distance between source and detector, this blurring effect will also hinder the position or location estimate of the source in the azimuthal and polar directions as well. Figure 2.5 compares the spread of the source distribution and position estimate of the same Cs^{137} check source data taken with the M400 detection system with a 30 cm separation distance, at varying focus distances and using a far field approximation.

For this measurement, the Cs^{137} check source is placed near the center of the detection system and expected to be imaged at 90° in both the polar and azimuthal directions, corresponding to a (0,0) x-y coordinate in the cartesian frame. Figure 2.6 shows that when the focus distance is set properly (at 30 cm) the angular resolution is near its peak and allows for a more precise estimate of the source's true location in comparison to other radii set for the imaging frame.

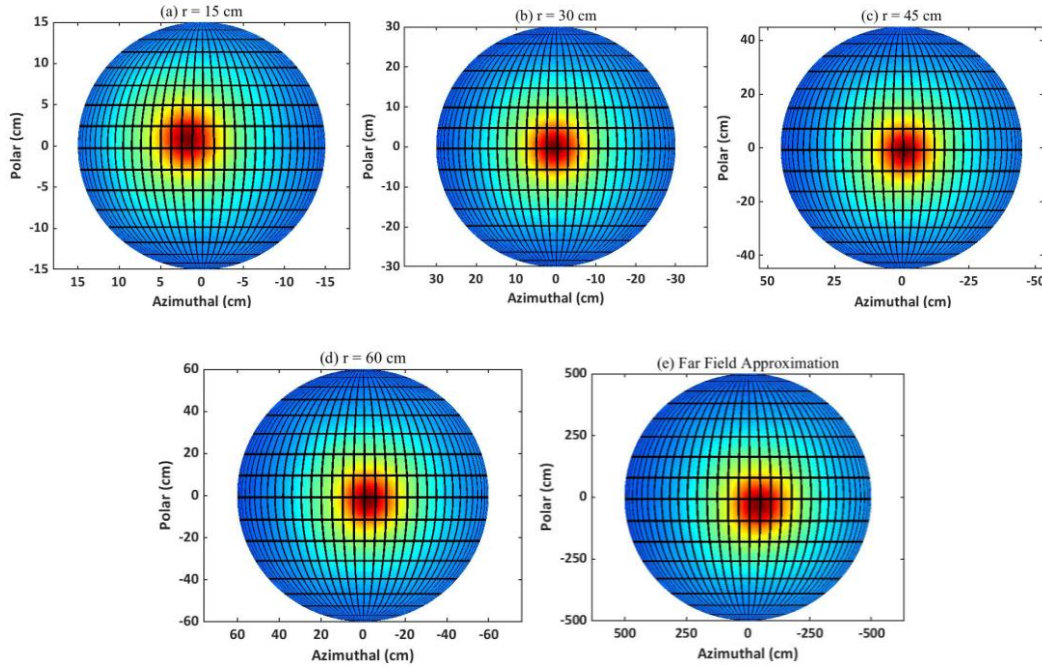


Figure 2.5: 2-D 4π image reconstructions of a Cs^{137} check source at varying image frame radii.

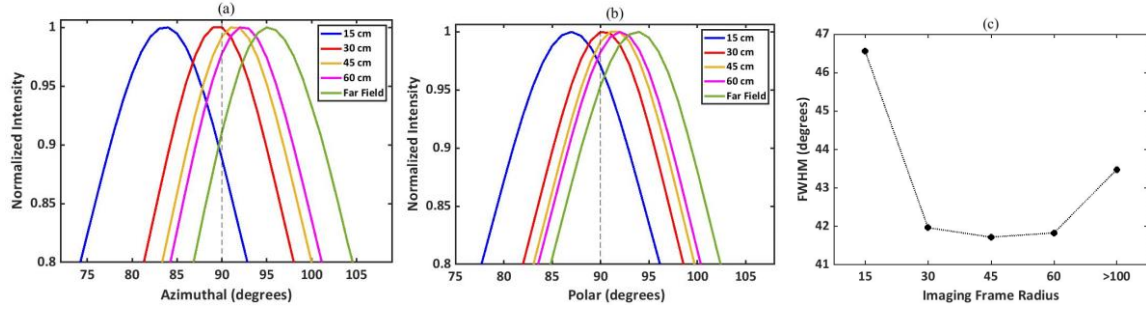


Figure 2.6: 1-D profiles along the peak intensity in the (a) azimuthal and (b) polar directions of each image reconstruction shown in Figure 2.6. The dotted black line represents the true source location. (c) FWHM versus image frame radius.

It is also possible to back project Compton rings onto a 2-D cartesian space or into a 3D cartesian space rather than a 4π sphere for near field imaging. A 2-D cartesian space is often preferred for near field imaging since the detector's geometry plays a considerable role. Since the vertex of each Compton cone reconstructed possess 3-D information about the event location, the back projected cone can be viewed in a 3-D space, as presented by Xu [29]. Using fundamental trigonometry, the azimuthal, and polar positions of the source distribution can be converted to cartesian coordinates further compensating for the change in solid angle of the angular bins or the pixel sizing and shape over a spherical imaging frame, where the cartesian coordinates are equal to:

$$x = r \cos(\theta) \sin(\phi) \quad (2.12)$$

$$y = r \sin(\theta) \sin(\phi) \quad (2.13)$$

$$z = r \cos(\phi) \quad (2.14)$$

where ϕ and θ represents the azimuthal and polar coordinates of the vertices of each pixel, respectively and r is the distance between source and detector, or the radius of the imaging sphere.

A 3-D imaging frame can be advantageous as it provides a depth perception of the source's distribution as well, which can provide a more accurate description of the source's shape and extent. However, this approach demands more storage space and computational time in both the

cartesian and spherical coordinate system. It is also worth noting that to an untrained eye, the blur of the Compton rings in a cartesian coordinate system, especially in a 3-D space, can be difficult to interpret and may lead to confusion about the source's true distribution in space if not properly accounted for or reduced via filtering or iterative methods for noise reduction.

2.4 Imaging Reconstruction Modalities or Methods

Compton imaging can be carried out using several different reconstruction methods. Classically, there are two different classifications of reconstruction algorithms: (1) inverse or direct reconstruction methods and (2) iterative methods.

2.4.1 Inverse Reconstruction Methods

Of the inverse methods, the naivest method is simple back projection (SBP). Simple back projection is a widely used imaging tool as it is computationally efficient, providing both speed and an adequate level of accuracy. As briefly described in Chapter 1, the Compton angle for each event is calculated based on the first scatter in the detector providing the half-opening angle of the Compton cone and the lever arm drawn between the first and second interaction provides the general direction of the incident gamma-ray. In SBP, each Compton cone is back projected to the desired imaging frame, where only the rings of the cones are seen in the final image. SBP reconstruction sums the back projected rings on the imaging surface, and with enough overlap or summation of the rings, the source estimate is improved, as shown Figure 2.7. Complete derivation and further details of this method can be found in the following references[10], [11], [12], [30].

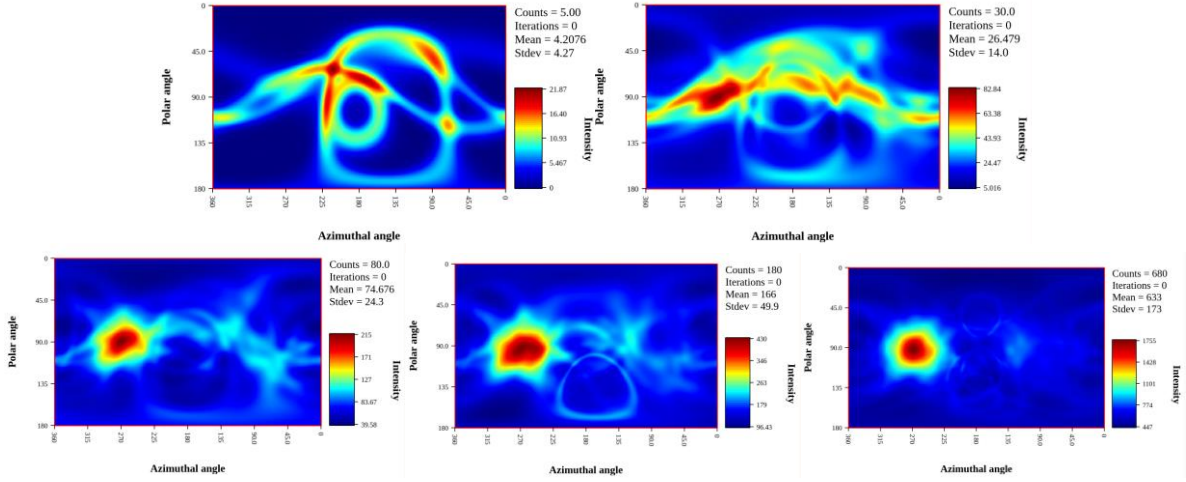


Figure 2.7: SBP reconstruction of increasing number of Compton rings. Note the improvement of the source location with increasing overlap of events.

To take the inverse method, SBP, a step forward, filtered back projection (FBP) can be used to overcome the inherent limited resolution of SBP, assuming there is associated Gaussian noise accounting for the uncertainty of detecting the observation. FBP is used to deconvolve the point spread function (PSF) or blur introduced by the uncertainty of the detection system, thus improving the resolution of the reconstructed images [31]. However, FBP requires a filter that appropriately models the point spread function of the system, which can be a challenge. For image reconstruction with CZT systems, a Weiner filter is applied to minimize the mean square error during the inverse process. The following references provide detailed derivation of the FBP reconstruction algorithm [10], [18].

2.4.2 Iterative Methods

For many imaging problems a direct reconstruction may not be the ideal imaging modality, especially in source estimation that utilizes Poisson data. Iterative reconstruction methods can achieve an accurate description of the source estimate and often provide a higher image resolution in comparison to the direct methods. Maximum Likelihood Expectation Maximization [14], [15]

[33], Order Subset Expectation Maximization [14], and Energy-Imaging Integrated Deconvolution [15], [34] are all iterative methods that have been fully implemented in the Orion Research Group.

Although iterative reconstructions can produce high resolution images and are widely used in Compton imaging applications, they can often be computationally expensive. To achieve maximum accuracy and resolution in the final image the data set provided to the algorithm must be iterated over to provide some statistical improvement via noise reduction or estimate enhancement. To do so the system matrix or data bank must be stored in memory for the duration of the processes, which can be computationally consuming. A complete derivation and detailed description of list-mode Maximum Likelihood Expectation Maximization (LM-MLEM) is provided in Chapter 4 of this text, in which the list-mode attribute allows for the system matrix to be created in step with the algorithm, saving some computational expense in both speed and storage.

CHAPTER III

Proton Radiation and Therapy

3.1 History of Hadron Therapy

Hadron therapy, often termed “ion beam therapy”, uses fast hadrons or subatomic particles, that can undergo strong interactions, for clinical radiotherapy. Hadron therapy was developed to obtain a better dose deposition profile when compared to x-rays used for conventional radiotherapy [35] [36]. In the last 60 years, many milestones have been achieved in the advancement of the technology and applications of hadron therapy. Much of the success of hadron therapy is in part due to: (1) the development of rotating gantries, delivering the clinical beam to the patient at different angles, (2) the development of scanning beams, used to precisely radiate a tumor’s full geometry, and (3) their unique dose profile which has a finite stopping point, corresponding to the location of the largest dose deposition along its path, thus mitigating any associated exit dose, as seen in standard x-ray radiotherapy.

The first hadrons used in radiotherapy were fast neutrons in 1936 published by J. Lawrence et. al and were used clinically in 1938, treating patients using a 37-inch cyclotron accelerating deuterons up to 8 MeV [37]. Boron Neutron Capture Therapy (BNCT) is another technique that utilizes epithermal to thermal neutrons by using a radiotracer that allows for the boron compounds to accumulate in the tumor. When the low energy (0.025 eV) neutrons hit the ^{10}B nuclei in the tumor they are absorbed by the boron atoms which emit alpha and lithium, ^7Li , ions which have

very short tracks and very high LET (linear energy transfer) [38]. The energy released by the emitted ions are confined to the tumor controlling the breakdown of the cancerous tissues.

Neutrons have shown to be particularly useful in attacking radio-resistant tumors or tumors that did not respond to standard x-rays. However, neutrons are difficult to collimate and have an unfavorable depth-dose distribution and for that reason are typically not used clinically [39].

In 1946 Robert Wilson introduced highly accelerated protons to hadron therapy after realizing that the depth-dose profiles of the protons in matter have a significant increase at the end of their range, or in their “Bragg peak” [36]. Today, both carbon ion and protons have been the forerunners in hadron therapy as they both provide advantageous dose-depth profiles and are capable of effectively irradiating x-ray resistant tumors. Although carbon and other light ions have the advantage of a finite dose range, the growth of dedicated clinical facilities was much slower in comparison to x-ray therapy. The reason for the slow growth of hadron therapy is the cost and scale of medical proton accelerators [40]. For x-ray therapy of deep tumors, it is enough to accelerate electrons up to 10 MeV, whereas protons must reach an energy of at least 200 MeV for the same range [39]. The energy requirements and magnetic rigidity of steering a massive number of heavy protons (1832 times heavier than electron) causes a typical proton gantry to be about 5-10 meters long and weigh about more than 20 tons, like the proton gantry used at the University of Florida’s Proton Therapy Institute in Figure 3.1 [41]. The weight and size for a carbon ion gantry to achieve the same requirements, is only scaled up, which are typically four times heavier, as carbon ions are 12 times heavier than the proton.

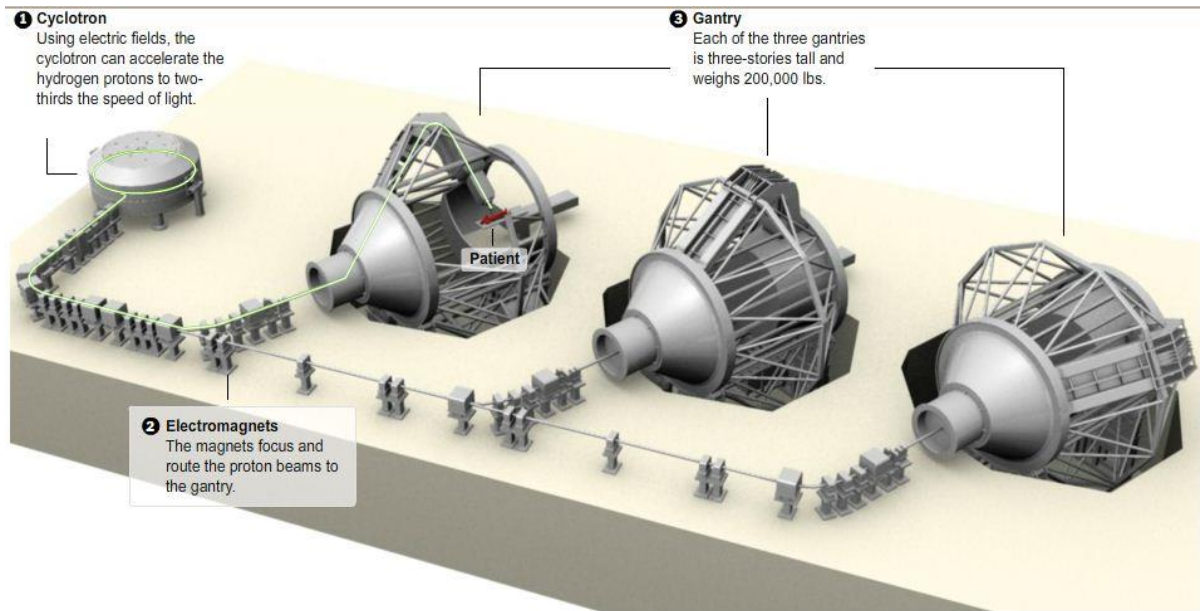


Figure 3.1: Illustration by the University of Florida Proton Therapy Institute of the cyclotron used to accelerate hydrogen atoms for use in three separate gantries.

As of today, over 170,000 patients have been treated using proton therapy and over 10,000 using carbon ions. Newly developed cyclotrons, such as the seven-meter diameter 250 MeV synchrotron built by Fermi Lab, have led to enormous strides in the number of clinical practices of hadron therapy for various cancers [42][43][44]. The Fermi cyclotron is one that introduced adjusting the angle of the beam's trajectory and scanning beams, which actively covers the tumor volume with "spot" or "raster" scanning of multiple beams. Compared with photon therapy, hadron therapy technology and underlying physics provides the benefit of reducing the volume of irradiated normal tissue and improvement in the defining the target area, as shown in Figure 3.2 which compares a standard x-ray treatment plan with that of a proton therapy treatment plan for the same tumor geometry [45], [46].

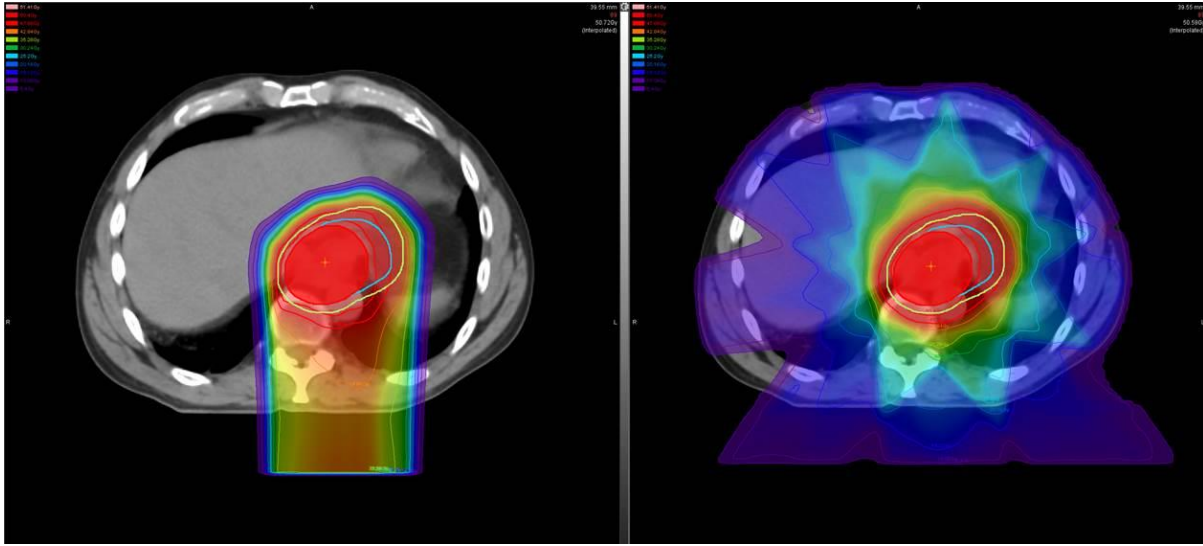


Figure 3.2: Treatment plan comparison using proton beam therapy (left) and x-ray therapy (right) for gastric cancer, studied by Dionisi et al.

3.2 Proton Beam Radiation

Proton beam radiation therapy (PBRT) is one of the latest types of radiotherapy, which has shown a satisfactory curing effect, especially for pediatric cancers [40]. The high energy protons can penetrate skin and tissue, undergoing a slowing down process as it interacts with the matter through nuclear scattering interactions and ionization. The point at which the proton rapidly and locally deposits the most amount of energy per a differential path length is referred to as the Bragg peak, detailed in section 3.2.2. This unique feature of the dose distribution of protons gives this radiotherapy technique an advantage over traditional photon therapy which has an associated exit dose as the photons leave the patient before full attenuation, leading to the irradiation of normal tissue along its path past its intended target location. The ability to spare nearby healthy tissue and have a conformal dose distribution is the highlighting feature of PBRT [47][48].

However, there are significant physical factors of PBRT that can hinder the reliability of this form of radiotherapy. The relative biological effectiveness (RBE) of proton therapy is typically

low, except at the end of the particle range. In practice, a fixed RBE value of 1.1 is used [49]. Yet, due to the true nature of the dose distribution of the proton beam drastically changing near the end of its track causes uncertainty in the RBE as the RBE should change along the proton's path with the increasing dose at the Bragg peak. The uncertainty in the RBE leads to uncertainty in the effectiveness of the dose delivered to the specified region over time. Also, the uncertainty in the range of the beam delivered during treatment can lead to the beam undershooting or overshooting the tumor, resulting in a geometrical miss of the tumor and the delivery of excessive dose to adjacent healthy tissues and critical organs that could potentially be at a health risk due to their proximity.

To mitigate these limitations of proton radiotherapy, effort has been placed in developing methods to measure the proton beam range during the treatment process based on the information acquired from the photons emitted during proton interactions within the patient [50][51].

3.2.1 Proton Interactions with Matter

Accelerated protons can interact with matter through various mechanisms in which the proton collides with either the orbital electrons of an atom or its nucleus. Coulombic interaction with the bounded electrons of the atom, nuclear reactions, and Bremsstrahlung processes can all take place, however Bremsstrahlung at therapeutic energies is nearly negligible [52]. Majority of the highly energetic protons will travel a nearly straight path as it loses energy typically to inelastic interactions with the atomic electrons which does not cause much deviation to the protons path, as it is much heavier in comparison to an electron. However, there are instances where the proton can be deflected by the large mass of the nucleus when passing close by, or the proton can undergo nuclear reactions with the nucleus, both of which can cause the proton to deviate from its intended

path or be absorbed altogether. Figure 3.3 illustrates the basic modes of interactions that the proton will likely undergo in a therapeutic scenario.

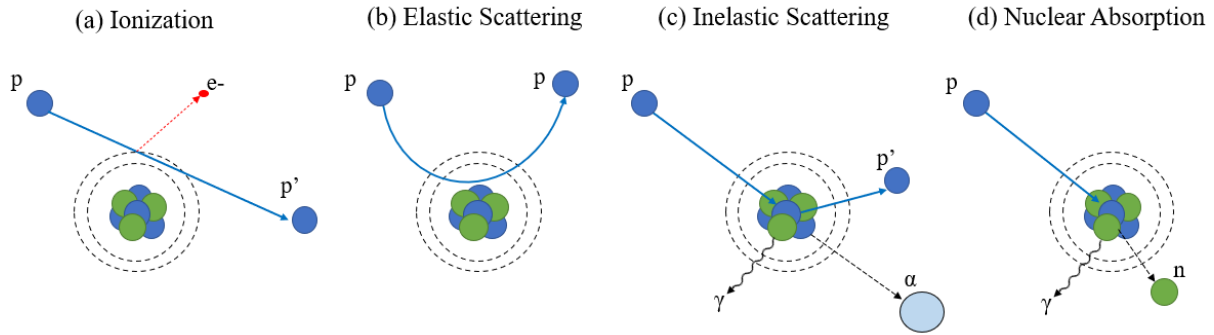


Figure 3.3: Illustrations of proton interactions: (a) Ionization of the target atom through Coulombic interactions, (b) Elastic scattering due to the repelling forces of the atomic nuclei and the proton, (c) Inelastic scattering causing secondary particle emission, (d) Nuclear absorption of the primary proton. (p = primary proton, e⁻ = electron, n = neutron γ = gamma ray, α = alpha particle)

3.2.2 Bragg Curve Characterization

As the proton undergoes nuclear interactions within a patient, the proton loses energy until its only mode of interaction is ionization with electrons near the end of its track. A proton will typically reach this state at about 100 keV, leaving little energy for the proton to travel much further, thus the maximum differential energy loss will be localized to this point. This slowing down process or bombardment of the proton can be theoretically described as the energy loss rate or the linear stopping power, S , which is defined as,

$$S(E) = -\left(\frac{dE}{dx}\right), \quad (3.1)$$

where dE , is the differential energy loss along the differential path length, dx . It is convenient to define the energy loss rate as independent of the mass and as a function of the average beam intensity and not a single particle. The stopping power of light ions or particularly, protons, is usually calculated under the following assumptions: (1) the light ion is moving much

faster than the target atoms, and more specifically, the electrons; and (2) the ion is much heavier than the target electrons.

The linear stopping power can be further developed to characterize the stopping power of a light ion beam within a homogeneous medium, i.e. water, tissue, or bone, which is ideal for most dosimetry problems. However, to characterize the proton energy loss for a specific therapeutic case, the energy loss rate equation becomes more complex and thus poses a challenge in approximating the true nature of the continuous slowing down or energy loss of the energetic particle.

The energy loss rate for an accelerated beam can be described using various formulas to fit the problem in question. The following approximations only consider the energy transfer from the projectile to the medium via continuous bombardment of the particle in motion, thus the statistical fluctuation or straggling of the residual energy over its path, $E(x)$, is not considered. Described here are three different methods increasing in complexity thus increasing in accurately describing the nature of a proton beam in any medium. The first is a function of mass density or the “mass stopping power”, secondly, the Bragg-Kleeman Rule (BKR), and lastly the Bethe and Bloch formula.

The mass stopping power formulates the energy loss as a function of the mass density, ρ , of the absorber material,

$$S(\rho) = -\frac{dE}{\rho dx} \quad (3.2)$$

This model is simple in approach but defines the differential energy loss of the ion as a function of the absorber material and assumes that the target is a homogeneous material. This approximation would not be the ideal choice for depicting the true energy loss and range of the

proton, since the energy loss of ions passing through matter could be a function of both nuclear stopping (ion-nuclei interaction) or electronic stopping (orbital electron-ion interaction) as dictated by Bohr [53]. Both modes of stopping will have different effects on the energy loss and trajectory of the proton and should be accounted for.

The energy loss rate formula based on the BKR was originally derived for alpha particles but provides an accurate description of the proton energy loss as well [52],[54],

$$S(E) = -\frac{dE}{dx} \approx AE_0^{1-p}, \quad (3.3)$$

where p is a constant that accounts for the dependence of the proton's energy on its velocity and A is the absorber material coefficient. Both constants can be derived by fitting to ranges derived from Monte Carlo based simulations or experimental data. The absorber material coefficient can be described using the following equation,

$$A = -\frac{1}{p\alpha\rho}, \quad (3.4)$$

which is a function of the absorber's density, ρ , the proton's velocity constant, p , and α , the material derived constant from measurements or theory. The stopping power, S , is typically given in units of MeV-cm²/g, where p unitless, and A , having units of cm²/g.

Lastly, the Bethe-Bloch formula is a more physically accurate description of the slowing down process of the proton in a uniform medium by solely accounting for the ionization processes, ignoring any energy loss by nuclear reactions with the target nuclei, as the dominant mode of interaction is the electronic stopping. For complete derivations, the following references are suggested [55], [56]. The Bethe-Bloch formula is described here as,

$$S(E) = -\left(\frac{dE}{dx}\right) = 2\pi N_A r_e c^2 \rho Z_{eff} \left(\frac{Z}{A}\right) \left(\frac{1}{\beta^2}\right) \left[\ln\left(\frac{2E_e \beta^2 \gamma^2 E_{max}}{I^2}\right) - 2\beta^2 - \delta - \frac{2C}{Z} \right] \quad (3.5)$$

where:

- N_A = Avogadro's number
- ρ = density of the absorber material
- δ = density correction
- Z = the atomic number of the absorber material
- A = atomic weight of the absorber material
- r_e = classical electron radius
- C = electron shell correction
- I = average excitation potential of the material atoms
- c = speed of light
- z_{eff} = the effective charge of the particle
- $\beta = v/c$ where v is the velocity of the proton
- $\gamma = 1/\sqrt{1-\beta^2}$

The energy loss rate according to Bethe-Bloch is thus directly proportional to the electron density of the absorber material and the velocity of the projectile. The electron shell and density correction factors involve relativistic theory and quantum mechanics, which become significant at very high or very low proton energies, which is absorber material dependent. Many have completed experiments and simulations to give accurate corrections for various high energy light ions stopping power for specific target mediums. See the International Commission of Radiation Units and Measurements (ICRU) Report-49 by Berger et al. for a complete article on stopping powers and ranges of protons and alpha particles [57]. Andersen and Ziegler also provide an extensive study for the proton specifically [58].

Ziegler et al developed a software package SRIM – Stopping and Range of Ions in Matter that utilizes the Bethe-Bloch formula to derive the stopping power and theoretical range of light ions, most notably, H, He, and Li [59]. Figure 3.4 plots the stopping power as a function of proton energy in water, tissue, and bone, using SRIM-2010.

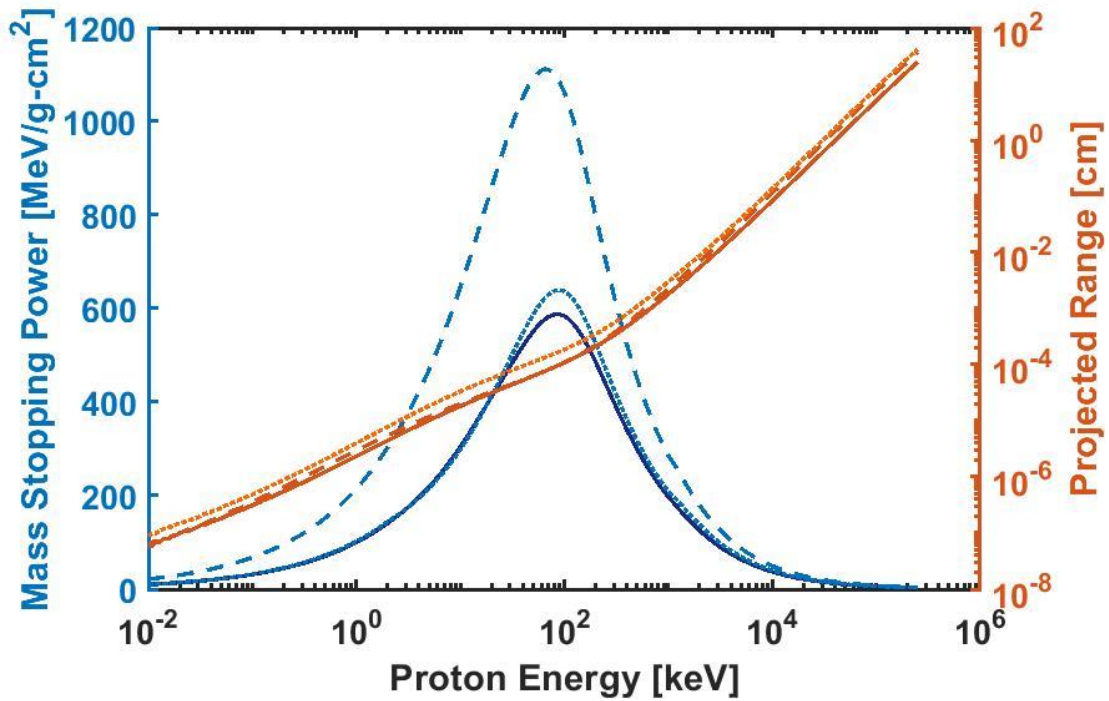


Figure 3.4: Mass stopping power and projected range curves calculated for three different materials. Bone equivalent plastic (solid line, $\rho=1.83 \text{ g/cm}^3$), Polyethylene (dashed line, $\rho = 0.97 \text{ g/cm}^3$), Tissue (dotted line, $\rho=1.03 \text{ g/cm}^3$)

The comparison of the electronic mass stopping power to the logarithmic range of the proton as a function of increasing energy shows that the trend is nearly the same for all three materials peaking at energies around 100 keV. The projected range profiles show a linear relationship between the logarithm of the proton energy and range. Thus the calculation of the proton's range can be described as a power law given some correction factor for the material [60].

Plotting the specific energy loss or stopping power of an accelerated proton in some known material, is referred to as the Bragg curve. The Bragg curve is also a very accurate description of the dose deposition of the central axis of a proton beam, following the beam's nearly straight trajectory until coming to rest. At this rest point, the dominant mode of interaction is ionization in this concise location and the proton abruptly loses the rest of its energy. The Bragg curve can then be converted to dose and used to display the dose deposited by the proton within the target or

patient over its entire trajectory. Figure 3.5 shows a theoretical Bragg curve for a 100 MeV proton beam in polyethylene.

This theoretical Bragg curve applies to the central axis of the beam however, in practice, not all protons will lose their energy the exact same way. Thus, there is expected perturbation about the derived Bragg curve profile. There are specific regions of the proton's Bragg Curve that will deviate from its theoretical stopping point as there are protons that will deviate from the nearly straight path due to the random nuclear processes. The following subsections will briefly describe those regions of interest along the Bragg curve and the uncertainty in these regions and other variations of the Bragg curve for tumor specific irradiation.

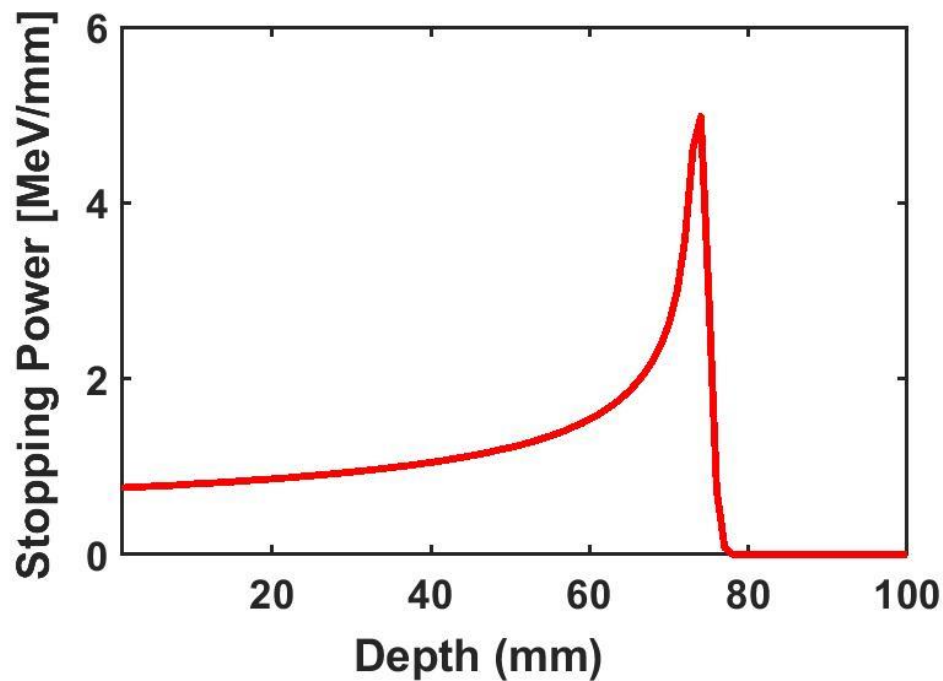


Figure 3.5: Theoretical polyethylene (density = 0.97 g/cc) Bragg Curve for a 100 MeV proton beam.

3.2.2.1 Bragg Peak

The Bragg peak signifies the differential depth where the largest amount of energy is released by the proton. Before this point, the high energy proton has given off a large portion of its energy before it reaches the Bragg peak range, around 1-2 MeV, thus losing the rest in a very short distance. The width, location or depth into the target, and height of the peak are all features that depend on the proton stopping power and energy uncertainty. The Bragg curve and peak are one-dimensional attributes describing the average energy loss of the proton beam along its central axis. However, due to the random interactions of each proton in the beam, the Bragg peak will have some spread radially and laterally about the beam central axis. The depth at which the Bragg peak occurs is very near the end of the beam's range but there are still residual ions that extend slightly beyond this point.

3.2.2.2 Distal Fall off Region

The distal fall off region of the Bragg curve extends from the Bragg peak depth location. The width or the extent of this region is not constant for proton energy or material and possibly depends more on the random fluctuations of the proton interactions than the rest of the Bragg curve. The distal fall-off ends where the stopping power or dose falls below a set threshold value, i.e. %1 of the max dose. This region corresponds to the residual energy left past the Bragg peak until the complete stop of the proton beam.

3.2.2.3 Range and Straggling

Due to the natural randomization of the nuclear processes the proton can encounter, we do not expect each proton in a therapeutic beam to travel a straight path for its projected range. For the most part, we assume that the slowing down of the beam is a continuous smooth process, neglecting slight deviations in the trajectory by focusing on the beam and not the individual

particle. Although the assumption is valid, summing these small aberrations from the random bombardment of each proton will lead to variations in the range, the energy loss rate, and the angular projection of that proton along the beam path. all of which can be termed as straggling. Straggling is the accumulation of many small stochastic fluctuations in the energy loss of the proton beam.

The range of the proton is defined as the distance traveled until the proton has lost all its energy, the proton comes to rest and no further dose is deposited. The mean range, R , of a proton can be approximated by integrating the reciprocal of the stopping power[61]

$$R = \int_0^{E_0} \frac{1}{S(E)} dE. \quad (3.6)$$

Equation 3.6 shows that given an initial energy, E_0 , the mean range is the depth at which 50% of the protons come to rest. Energy and range straggling heavily influences the shape of the proton Bragg curve and thus the fluctuation in the range. The energy straggling of each individual proton will alter the stopping point or range of that proton, contributing to the uncertainty of the projected Bragg peak for a monoenergetic beam. Several authors have shown that the energy straggling can be approximated to a simple power rule that gives the sigma as a function of the theoretical proton beam range; for example Chu et al describes the sigma as,

$$\sigma_{\Delta} \approx kR_o^m \quad (3.7)$$

where R_o is the range in water, in centimeters, for a monoenergetic proton beam, k is the constant of proportionality, and m is empirically determined for the absorber [62].

Figure 3.6 shows the trajectory of 1E6 protons with an initial energy of 100 MeV and the calculated range and straggle longitudinally, laterally, and radially about the singular beam in a

high-density polyethylene target ($\rho = 0.97 \text{ g/cm}^3$) using, the SRIM extension Transport of Ions in Matter (TRIM), SRIM/TRIM-2010.

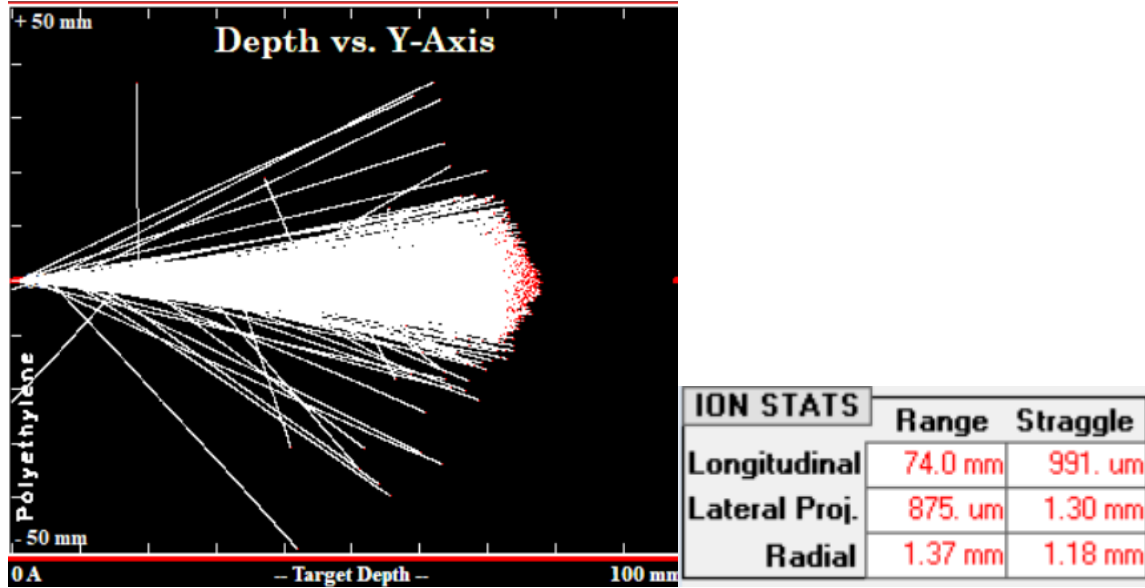


Figure 3.6: TRIM simulation of 100 MeV protons in polyethylene and the associated mean range and straggle of the beam intensity.

3.2.2.4 Spread-out Bragg Curve

With technological advancement in therapeutic proton beams, the depth-dose distribution can be modified for volumetric specifications. By intentionally modifying the Bragg peak location of each proton beam the summation of many singular beams can provide a 3-D region of maximum dose deposition. Clinical systems can either raster a modulated beam back and forth or magnetically steer very radially small beams with varying energies to extend the Bragg peak region and dose over the desired volume. Figure 3.7 gives an example, from Liu and Chang, of a spread out Bragg peak (SOBP) which can also experience the hills and valleys depending on the technology's method of spreading the dose [47].

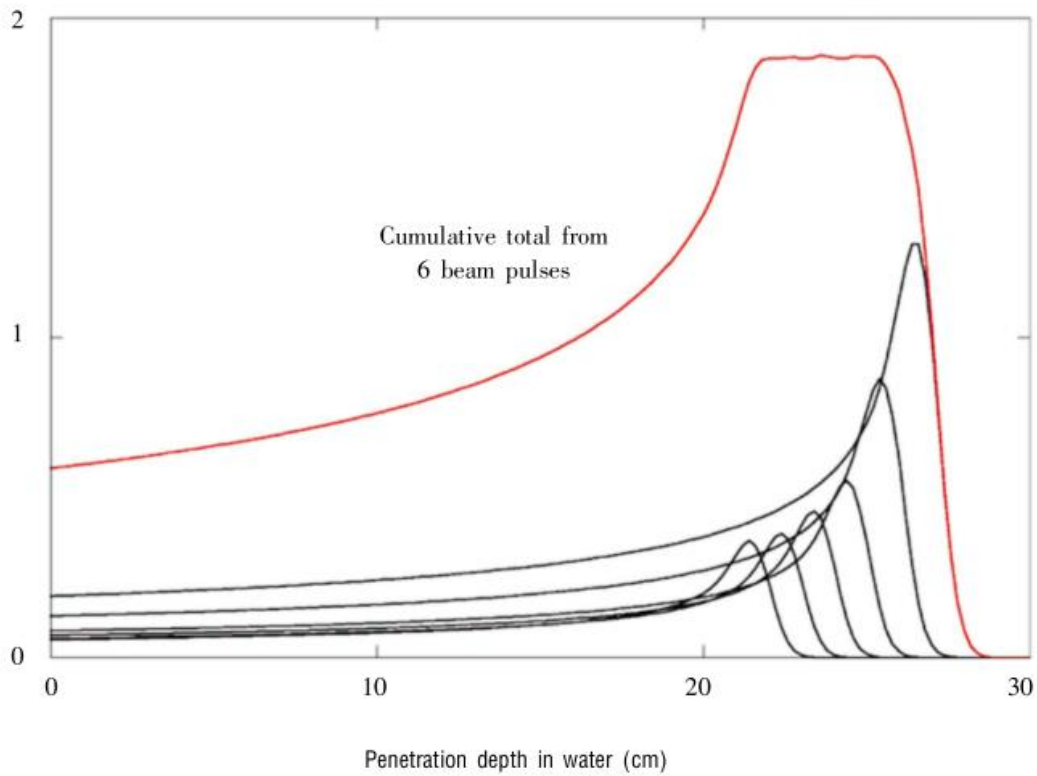


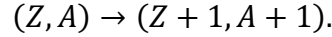
Figure 3.7: Cumulative total dose from 6 beam pulses to create a spread out Bragg peak, SOBP [47].

3.3 Prompt Gamma Ray Emission

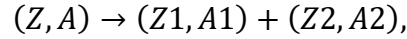
Along with the dominating interactions with the orbital electrons within the target medium the proton can also undergo nuclear reactions with the atomic nucleus which can cause the nucleus to become excited, break apart, or absorb the proton and become an entirely different nucleus. Although nuclear reactions only make up about 0.1% of the reactions an accelerated proton will undergo before coming to rest, these reactions can lead to a cascade of nuclear events emitting gamma rays on the order of 10^3 photons per 100 keV [63][64].

As the highly energetic proton travels through any given medium, it can undergo four different nuclear reactions with the target nuclei of mass number (Z) and atomic mass (A) leading to reaction products that are left in an excited state:

1. The proton can be captured by the target nuclei creating an unstable nucleus:

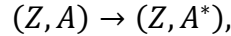


2. The proton can cause a two-body break up reaction:



in which the sum of $Z1$ and $Z2$ equals Z and the sum of $A1$ and $A2$ equals A . Where either or both products can be excited.

3. The proton can inelastically scatter with the target nucleus:



where the nucleus is now in the excited state and will emit some energy to reach its ground state.

4. The proton can cause spallation reactions where the proton energy surpasses the total binding energy causing full spallation of the nucleus, breaking it down to many small atomic number fragments. For example the 11-body reaction of $p^+ + {}^{12}\text{C} \rightarrow 5({}^1\text{H}) + 5n + \text{H}_2$.

The excited products of these interactions can decay by emitting gamma rays. These photons can be emitted as both prompt and delayed emissions, ranging in half-lives from orders of magnitude less than picoseconds to minutes post proton interaction [65].

For this work, the proton-induced reactions with oxygen and carbon are the focus as they are two of the most common elements in the human body. The target material used in the experimental analysis, shown in later chapters, is a high-density polyethylene (HDPE) plastic, C_2H_4 , with a density of 0.97 g/cm^3 , and deexcitation gammas are not expected from proton-hydrogen interactions. The nuclear deexcitation gamma-ray lines for proton interactions with ${}^{12}\text{C}$ and ${}^{16}\text{O}$ are shown in Table 3.1 and their measured half-life are adapted from the study conducted in [65].

Line (MeV)	Reaction	Transition	Mean Life (s)
0.718	$^{12}\text{C}(p, x)^{10}\text{B}^*$ $^{12}\text{C}(p, x)^{10}\text{C}(e)^{10}\text{B}^*$ $^{16}\text{O}(p, x)^{10}\text{B}^*$	$^{10}\text{B}^*0.718$	1.0E-9 27.8 1.0E-9
1.022	$^{12}\text{C}(p, x)^{10}\text{B}^*$ $^{16}\text{O}(p, x)^{10}\text{B}^*$	$^{10}\text{B}^*1.740 \rightarrow (0.718)$	7.5E-15
1.635	$^{16}\text{O}(p, x)^{14}\text{N}^*$	$^{14}\text{N}^*3.948 \rightarrow (2.313)$	6.9E-15
2.000	$^{12}\text{C}(p, x)^{11}\text{C}^*$	$^{11}\text{C}^*2.000$	1E-14
2.124	$^{12}\text{C}(p, x)^{11}\text{B}^*$	$^{11}\text{B}^*2.125$	5.5E-15
2.313	$^{16}\text{O}(p, x)^{14}\text{N}^*$	$^{14}\text{N}^*2.313$	9.8E-14
2.742	$^{16}\text{O}(p, p')^{16}\text{O}^*$	$^{16}\text{O}^*8.872 \rightarrow (6.130)$	1.8E-13
3.684	$^{16}\text{O}(p, x)^{13}\text{C}^*$	$^{13}\text{C}^*3.685$	1.6E-15
4.438	$^{12}\text{C}(p, p')^{12}\text{C}^*$ $^{16}\text{O}(p, x)^{12}\text{C}^*$	$^{12}\text{C}^*4.439$	6.1E-14 6.1E-14
4.444	$^{12}\text{C}(p, n)^{12}\text{N}^*$ $^{12}\text{C}(p, 2p)^{11}\text{B}^*$	$^{11}\text{B}^*4.445$	11E-3 5.6E-19
5.105	$^{16}\text{O}(p, x)^{14}\text{N}^*$	$^{14}\text{N}^*5.106$	6.3E-12
5.180	$^{16}\text{O}(p, x)^{15}\text{O}^*$	$^{15}\text{O}^*5.181$	<4.9E-14
5.240	$^{16}\text{O}(p, x)^{15}\text{O}^*$	$^{15}\text{O}^*5.241$	3.25E-12
5.269	$^{16}\text{O}(p, x)^{15}\text{N}^*$	$^{15}\text{N}^*5.270$	2.58E-12
5.298	$^{16}\text{O}(p, x)^{15}\text{N}^*$	$^{15}\text{N}^*5.299$	1.2E-14
6.129	$^{16}\text{O}(p, p')^{16}\text{O}^*$	$^{16}\text{O}^*6.130$	2.7E-11
6.175	$^{16}\text{O}(p, x)^{15}\text{O}^*$	$^{15}\text{O}^*6.176$	<2.3E-14
6.322	$^{16}\text{O}(p, x)^{15}\text{N}^*$	$^{15}\text{N}^*6.324$	1E-15
6.337	$^{12}\text{C}(p, x)^{11}\text{C}^*$	$^{11}\text{C}^*6.339$	<1.1E-13
6.476	$^{12}\text{C}(p, x)^{11}\text{C}^*$	$^{11}\text{C}^*6.478$	<8.7E-15
6.741	$^{12}\text{C}(p, x)^{11}\text{B}^*$	$^{11}\text{B}^*6.743$	4.3E-20

6.790	$^{12}\text{C}(p, x)^{11}\text{B}^*$	$^{11}\text{B}^*6.792$	5.6E-19
6.916	$^{16}\text{O}(p, p')^{16}\text{O}^*$	$^{16}\text{O}^*6.917$	6.8E-15
7.115	$^{16}\text{O}(p, p')^{16}\text{O}^*$	$^{16}\text{O}^*7.117$	1.2E-14
7.299	$^{16}\text{O}(p, x)^{15}\text{N}$	$^{15}\text{N}^*7.301$	1.4E-16
15.10	$^{12}\text{C}(p, p')^{12}\text{C}^*$	$^{12}\text{C}^*15.11$	1.5×10^{-17}

Table 3.1: Expected proton induced reactions on ^{12}C and ^{16}O .

As seen in Table 3.1, the expected gamma ray lines range in energies up to 15 MeV. The mean life of these reactions range in time from shorter than picoseconds to tens of seconds, many of which are close in energy, no more than 100's of keV apart. Both the lifetime and energy of these gamma ray lines will play a significant role in accurately detecting them for spectral analysis. For each of these reactions there is an associated cross-section that gives the probability that the proton will cause the reaction given that proton is at a particular energy. Detailed experiments and simulations have been conducted to provide the cross-section for various prompt gamma emissions, here are a few of those studies [65]–[69].

3.4 Proton Energy Threshold

For many of the reactions shown the proton would need a large amount of energy to not only overcome the binding energy of the nucleus but then enough energy to cause it to break apart or create some momentum to excite the nucleus to provide a gamma-ray from de-excitation.

If we consider the reaction

$$p + A \rightarrow b + B, \quad (3.7)$$

where p is our particle of interest, the accelerated proton, A is some target nuclei, and b and B are both reaction products. We must also remember that our reactions are not limited to just two

products and could possibly be a summation of more than two, i.e. $b + b1 + b2 \dots bN$. Typically, nuclear reactions are surmised to no more than 4 fragmented products.

Employing the law of conservation of energy and momentum proves that the minimum energy required, kinetically, or the threshold energy, E_{th} , of our proton to initiate the above reaction in 3.7 can be equated to

$$E_{min} = E_{th} = -Q \frac{(M_A + m_p)}{M_A}, \quad (3.8)$$

where M_A and m_p are the atomic mass of our target nucleus and nuclear mass of projectile particle, respectively. Q is the q-value or decay energy, quantifying the energy released during the decay process,

$$Q = E_i - E_f = (m_A - m_B)c^2. \quad (3.9)$$

Q is equal to the difference in the initial energy, E_i , and the final energy, E_f , of the nuclear reaction, where m_A is the rest mass of the reactants and m_B is the rest mass of our products, and c is the speed of light.

Equation 3.8 is valid for energies much less than the rest mass energy of the involved particles thus allowing us to treat the threshold energy equation classically or as non-relativistic. However, at high energies, the relationship between the rest mass energies of the particles must be accounted for using the relativistic equations for energy and momentum. Thus the threshold energy is calculated as

$$E_{min} = E_{th} = -Q \frac{(m_p + M_A + m_B + M_B)}{2M_A}. \quad (3.10)$$

For most inelastic scattering processes that result in the emission of a prompt gamma-ray the threshold energy is slightly higher than that of the deexcitation photon, as the proton only needs

enough energy to excite the nucleus so that it decays via the gamma ray. However for nuclear spallation reactions that results in fragmented products the threshold energy required is much higher. Knowing the threshold energy requirements for specific prompt gamma-ray lines can be useful information in deciphering where along the proton beam these photons will be emitted and thus correlating their emission to the range of the proton beam, the Bragg peak location, or even the dose distribution.

CHAPTER IV

LM-MLEM for Prompt Gamma Ray Imaging

4.1 Introduction

The goal of an imaging algorithm is to provide an estimate of the source distribution in space based on the observed data and the detection system response. Experimental imaging can be treated as a parameter estimation problem for an observed measurement for a given set detection parameters. Each photon interaction is treated as a Poisson random variable when estimating the source location due to counting statistics. Gaussian blurring of the calculated Compton ring for each photon interaction provides a noise model that introduces the uncertainty in the energy deposition and position of the interaction to accurately depict the real detection system's response. This noise model can introduce error in the final image reconstruction especially in the cases of low statistics.

Employing an iterative algorithm such as, Maximum Likelihood Expectation Maximization (MLEM) for Compton imaging is useful as it can provide an informative observation in the reconstruction of sparse datasets, which is the nature of Compton imaging events. For image estimation of Poisson measurements, iterative methods have the advantage compared to direct

Portions of this chapter is based on submitted work currently under peer review: V. Nwadeyi, J. A. Fessler, Z. He, "Region of Interest Image Reconstruction for Compton Imaging Using 3D Position Sensing CdZnTe," IEEE Transactions on Nuclear Science, 2021.

methods as they can provide a superior resolution through improvement of the source estimation from statistical inference [33].

This chapter will provide a derivation of MLEM for Compton imaging with the condition that the observation data set is list-mode data. List-mode data means that there is a defined finite number of events based on a preset number of accepted events and or preset measurement time [70]. Following the derivation of list-mode MLEM (LM-MLEM), the application of LM-MLEM to high energy and high flux Compton events will be assessed. The ultimate goal of this work, is to provide an image estimate of prompt-gamma ray photons, specifically the 4.44 MeV photon from Carbon interactions for proton beam range verification [71], [72].

When imaging prompt gamma-rays there is the issue of noise due to partial energy deposition events, the Compton continuum beneath the photopeaks, chance coincidence events, and the limitations of CZT detection efficiency at high energies, all of which interfere with the reconstruction of Compton cones[73], [74]. One method to overcome this noise interference in the imaging domain and save computational cost of the ML algorithm is to truncate the image space.

Truncating the imaging space can be a simple solution when prior knowledge of the source location is introduced. Truncated field of view (FOV) imaging is a method employed for many medical imaging applications where the source is much smaller than the FOV and high imaging resolution is desired [7], [75], [76]. Truncating the FOV is introduced in this chapter as a method to reduce computational cost and mitigate noise interference for MLEM reconstructions, while enhancing the pixel resolution of the final image reconstruction.

However, when employing MLEM for image reconstruction for a FOV that is too small, the source distribution estimate converges to the corner of the image space. To overcome this corner convergence, we redefined the LM-MLEM algorithm as ROI-MLEM to allow for the

update of the region of interest (ROI) space. This chapter derives ROI-MLEM and assesses its capability to provide image reconstructions in a pre-defined ROI space.

4.2 Derivation of List-Mode Maximum Likelihood Expectation Maximization

One method of source distribution estimation is to treat the image reconstruction as a parameter estimation problem, where the gamma-ray source distribution in space is the parameter estimated from a given set of detected observations. Thus our parameter estimation problem can take the form of a discrete imaging model in matrix notation, like the imaging model introduced in section 2.3,

$$\mathbf{T}\mathbf{f} = \mathbf{g}, \quad (4.1)$$

where \mathbf{f} is the source distribution image vector and the parameter to be estimated. To estimate \mathbf{f} , a set measurement, \mathbf{g} , and a response function, \mathbf{T} , is needed. \mathbf{T} contains the spatial probability that a photon would be recorded as an event of \mathbf{g} . The estimation problem can be rewritten as a function of the mean estimate of each event in our observation by discretizing the source estimate of \mathbf{f} to the number of photons emitted from each element of the image vector. Each element of \mathbf{f} can be seen as an independent random variable, and the sum of the Poisson random variables allows for 4.1 to be written as a model describing the mean of the i^{th} measurement,

$$\bar{g}_i = \sum_{j=1}^J t_{ij} f_j, \quad (4.2)$$

where the image vector, \mathbf{f} , is discretized into J imaging pixels, or voxels. The response function, \mathbf{T} , is a system matrix of size $I \times J$, comprised of elements, t_{ij} , over all image elements $\{1, 2 \dots J\}$ and for each event, i . That is to say that each row of \mathbf{T} is the reconstructed Compton ring for that event, or the probability of that event occurring in each element of \mathbf{f} . The mean observation $\bar{\mathbf{g}}$,

contains the attributes of each photon event in the list-mode data, i.e., $\{ \mathbf{g}_1, \mathbf{g}_2, \dots, \mathbf{g}_I \}$, where each \mathbf{g}_i can contain position, timing, and energy information about each photon and each interaction that photon underwent, depending on the detection system information output. The assumption that the mean of each observation element is an independent Poisson variable for each photon event can also be made.

Directly solving the system of equations in equation 4.2 could be attempted but would not result in a well-defined source estimate due to the low intrinsic count rates of photon detection. Instead the ML method tries to solve the problem from a statistical standpoint [77]. By determining the likelihood of observing \mathbf{g} as a function of \mathbf{f} , the problem can be carried out by maximizing the likelihood of the probability of observing each event of \mathbf{g} in \mathbf{f} , that is,

$$\mathbf{P}(\mathbf{g}_i|\mathbf{f}) = \prod_{i=1}^I e^{-\bar{g}_i} \left(\frac{\bar{g}_i^{g_i}}{g_i!} \right). \quad (4.3)$$

Thus the probability or likelihood of observing \mathbf{g} is a positive definite that can be simplified by maximizing the logarithmic likelihood of equation 4.3,

$$L(\mathbf{g}|\mathbf{f}) = \ln \mathbf{P}(\mathbf{g}|\mathbf{f}) = \sum_{i=1}^I -\bar{g}_i + \mathbf{g}_i \ln \left(\frac{\bar{g}_i}{g_i!} \right). \quad (4.4)$$

Expanding equation 4.4 and substituting \bar{g}_i , from equation 4.2 we get the following,

$$L(\mathbf{g}|\mathbf{f}) = \sum_{i=1}^I \left[\sum_{j=1}^J t_{ij} f_j + \mathbf{g}_i \ln \left(\sum_{j=1}^J t_{ij} f_j \right) - \ln (g_i!) \right]. \quad (4.5)$$

Equation 4.5 can be maximized, that is, maximize the log-likelihood of the source distribution estimate in our image vector, by taking the partial derivative with respect to an image vector

element, f_j , and setting equal to zero. However, equation 4.5 nor its derivative is a linear equation and would be difficult to solve directly.

Alternatively, equation 4.5 can be maximized iteratively by employing the expectation maximization algorithm [78]. This is a two-part process: the expectation step and the maximization step. (1) The expectation step calculates the expected value of the observation, \mathbf{g} , given the previous estimation of the source estimate, which we will denote as f^n , where the current iteration of the source estimate image vector is f^{n+1} , which is the image of interest. (2) The maximization step finds the maximum-likelihood of the source distribution estimate based on the expected value.

4.2.1 Expectation

The expected value of the source distribution can be described as a function of the probability of the photons emitted in the image space. Given the n^{th} estimate of the source distribution the probability can be calculated as,

$$P(j|i) = \frac{t_{ij}f_j^n}{\sum_{j=1}^J t_{ij'}f_{j'}^n}. \quad (4.6)$$

Equation 4.6 describes the probability for the event, i , to be emitted from pixel j . From our observation measurement, we can obtain g_i detected counts for each event i . Therefore the expectation of the number of photons that were detected for pixel j for each event i , ε_{ij} , given g_i and the n^{th} estimate of our source distribution, f^n , can be calculated as,

$$E(\varepsilon_{ij}|g_i, f^n) = g_i P(j|i). \quad (4.7)$$

The expected total number of photons to be emitted from pixel j and then detected based on the observation measurement is then given by substituting equation 4.6 into 4.7,

$$E(\varepsilon_j | g_i f^n) = \sum_{i=1}^I g_i E(\varepsilon_{ij} | g_i, f^n) = \sum_{i=1}^I g_i \left(\frac{t_{ij} f_j^n}{\sum_{j'=1}^J t_{ij'} f_{j'}^n} \right). \quad (4.8)$$

Thus equation 4.8 gives the expected value of the source distribution which describes the mean value of the number of photons emitted from each pixel in the image vector given the measurement dataset detected by the detector and the previous estimate of the source distribution. Rearranging equation 4.8 gives,

$$E(\varepsilon_j | g_i f^n) = f_j^n \sum_{i=1}^I \left(\frac{g_i t_{ij}}{\sum_{j'=1}^J t_{ij'} f_{j'}^n} \right). \quad (4.9)$$

which will be used in the maximization step.

4.2.2 Maximization

Given the Poisson nature of a photon measurement, the total number of photons detected from each image pixel j , ε_j , can be defined as a Poisson variable. Thus the maximum likelihood of the expectation of ε_j can be equated to its observed value of the mean value of the number of emitted photons in each pixel, $\bar{\varepsilon}_j$, i.e.

$$\hat{\bar{\varepsilon}}_j = E(\varepsilon_j | g_i f^n) = f_j^n \sum_{i=1}^I \frac{g_i t_{ij}}{\sum_{j'=1}^J t_{ij'} f_{j'}^n}. \quad (4.10)$$

To find the next iteration of the source distribution estimate, f_j^{n+1} , equation 4.10 is divided by the probability that a photon emitted from pixel j is detected as any event i , which describes the sensitivity of the system, s_j .

$$s_j = \sum_{i=1}^I t_{ij}. \quad (4.11)$$

Therefore, the iterative estimate of the source distribution, f_j becomes

$$f_j^{n+1} = \frac{\hat{\varepsilon}_j}{s_j} = \frac{f_j^n}{s_j} \sum_{i=1}^I \frac{g_i t_{ij}}{\sum_{j'=1}^J t_{ij'} f_{j'}^n}. \quad (4.12)$$

The source estimation problem is a function of list-mode data or a preset number of events, this means that in comparison to all possible measured events over all pixels, for each detection parameter (energy, depth, pixel resolution, etc.) that the observation data set, g , will be a very sparse vector, where each measured event will be ones and all other elements zeros. Thus the list-mode MLEM algorithm can be written as,

$$f_j^{n+1} = \frac{f_j^n}{s_j} \sum_{i=1}^I \frac{t_{ij}}{\sum_{j'=1}^J t_{ij'} f_{j'}^n}. \quad (4.13)$$

where the mean value of the observation.

4.3 Application for High-Flux and High-Energy Gamma-Ray Scenarios

Historically, LM-MLEM has been shown to be advantageous in imaging various radioactive sources, and only improves with adequate photon counting statistics. In comparison to SBP (simple back projection), MLEM provides a superior result with enhanced angular resolution for the same number of events. For example 10,000 photopeak events are reconstructed for a near

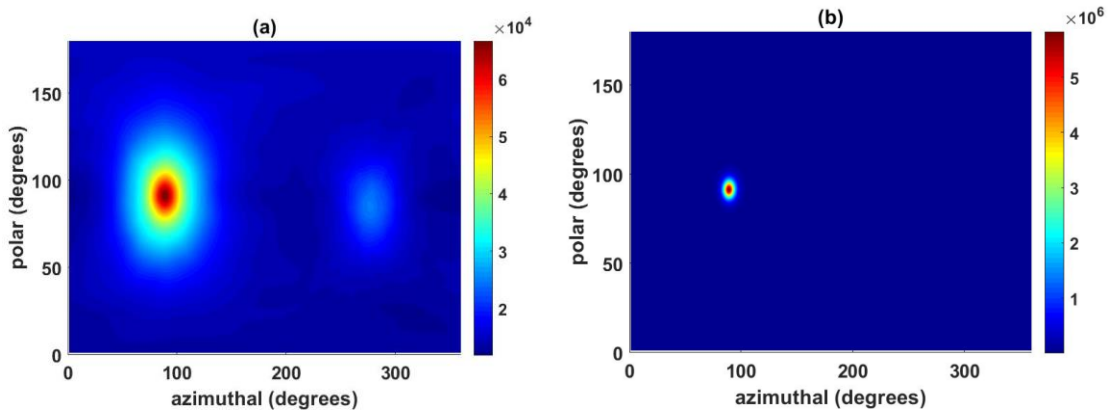


Figure 4.1: (a) SBP and (b) LM-MLEM reconstructions of the same 10,000 photopeak events from experimental Cs^{137} data.

field (30 cm) Cs¹³⁷ measurement. The SBP reconstruction and the 25th iteration of LM-MLEM are shown in Figure 4.1 for comparison.

MLEM iterates over the information and while doing so suppresses the noise associated with the uncertainty of the individual Compton rings, through enhancement of the pixels that reveal the most likely location of the source, as indicated by the intensity bar. Thus, improving the spatial resolution from a FWHM estimate of (34.87, 35.86) to (8.16, 8.03) in the polar and azimuthal directions, respectively.

4.3.1 High Energy and High Flux Source Imaging Using LM-MLEM

Due to CZT worsening energy resolution with increasing energy deposition, at photon energies above 2 MeV, the number of poorly reconstructed events will increase. The event reconstruction will inherently influence the development of the Compton cones, and in turn affect the image reconstruction using MLEM. At these higher photon energies, CZT is more susceptible to partial energy deposition events, chance coincidence events, and charge sharing events, which can skew the estimate of the Compton scattering angle used as the half opening angle in cone reconstruction and sequencing[18]. These events have also shown to be difficult in sequencing the order of the interactions, which can distort the lever arm of the Compton cone. When noise from these types of events is introduced in the image frame it can lead to high-frequency artifacts, shift variant and shift in-variant artifacts, all of which can hinder the ML image reconstruction.

In high-energy applications, there is often partial energy deposition events, which lead to a buildup of events in the Compton continuum which are multi-scatter events beneath photopeaks with a lower incident energy than the originating high energy photon. These partial events are then picked up as imageable events of a different photopeak. These Compton continuum events can

lead to noise in the image reconstruction causing a miscalculation of the cone opening angle or lever arm as the full energy deposition calculation is incorrect for those events.

If the incident energy of the photon is at least 1.022 MeV, pair production becomes a factor. The probability of collecting pair production events exponentially increases as the energy of the photon surpasses 1.022 MeV. This becomes an issue in imaging as the annihilation photons either escape the detector, leaving the energy deposition for the incident photon incomplete, or the annihilation photons are readily absorbed close to the photon's interaction and close in timing of the originating photon's interaction making it difficult to truly identify those events as pair production events or true Compton events near 511 keV. Recent work has been done in efforts to mitigate these events by simply discarding events that deposit energies near 511 keV or based on the cone opening angle that is associated with a two-pixel event where the 511 keV gamma is sequenced second [32]. However, in many cases this can lead to nearly a 50% loss of events and there is the possibility that some of these events may truly be real Compton scatter events. Also for most gamma-ray imaging problems, the data set may be too sparse even before discarding those ill-recorded events.

When the emission rate of the source exceeds, 30,000 events per second, the sources are described as high flux sources and typically refers to sources that exceed 10s of Curies in isotropic emission. For high-flux applications where the source is emitting many photons within a short period of time, chance coincidence events become the predominant cause of noise events that are translated to the image space. Under rapid bombardment of impinging photons CZT can become saturated as the number of triggers surpasses its timing window, not allowing enough time for full data collection. When this happens the events default to becoming Compton continuum events or low trigger events that are appended to other Compton events as a part of their scatter. The

mischaracterization of the rapid-fire events leads to error in the image reconstruction from miscalculation in the Compton ring reconstruction.

High flux emissions are very apparent in prompt gamma-ray imaging where there are many photons impinging on the detector with varying incident energies [5]. When there are photons with an energy above the photopeak of interest, it is possible these photons will cause a rise in the Compton continuum below the photopeak, as there are partial deposition events that will be recorded with lower energies and binned beneath the photopeak. These events have the potential to result in Compton cones that are pointed in the wrong direction and away from the source. It can be quite difficult to separate these events from true photopeak events.

In direct or Fourier transform imaging methods, it is possible to subtract images of the noise from the image of the photopeak by imaging Compton continuum events from both the left and right side of the photopeak. However, the continuum removal is not as simple as with iterative methods such as MLEM.

Experimentally, it has been shown that for high energy photon data that the energy resolution is much worse than it is predicted by simulations carried out by Geant4. This could be due to the charge sharing effects that are known to arise with larger electron clouds due to larger energy depositions from high energy photons. Figure 4.2 shows image reconstructions of a PuBe source at 30 cm distance from the H3D S400 X detection system and a Geant4 simulation of the same geometry.

Chapter 6 discusses in more detail why there is such a discrepancy in the energy resolution at high photon energies in CZT. Nonetheless, for both image reconstructions we see shift-variant noise artifacts that hinders the source reconstruction, forming a lower intensity ring around the source estimate and a ring opposite of the meridian of the 4π image. These ring artifacts are a

product of pair production events that are recorded as full energy deposition events and will be constant regardless of the source position in space.

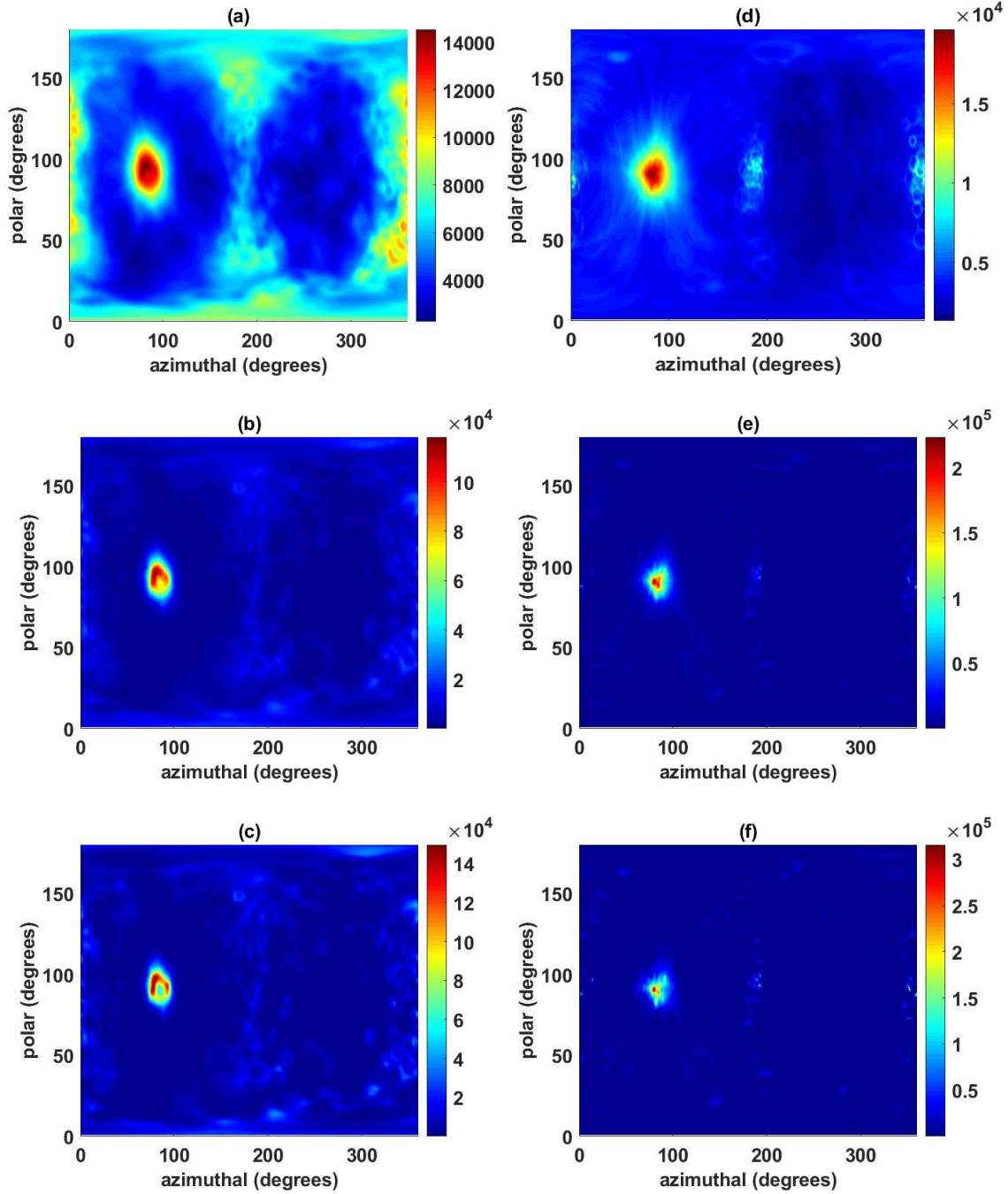


Figure 4.2: 4.44 MeV photopeak image reconstructions from an experimental PuBe source measurement (left column) and Geant4 simulations (right column). Both reconstructions use 5000 photopeak events. Shown are iterations 1 (a and d), 10 (b and e), and 20 (c and f).

As the number of iterations increases the source distribution starts to separate for both image reconstructions. At high energies and under a high flux of photons the risk of losing source distribution uniformity is also increased as the number of imageable photopeak events wane with energy resolution and detection efficiency. Pair production events can also be removed by setting a threshold on the opening angle of the events. Depending on the incident photon energy and sequencing of events the annihilation photons result in an opening angle near 90° [32]. However the same risk of removing true Compton scattering events apply.

4.4 Truncated Field of View Imaging Using Standard MLEM

To mitigate the noise artifacts in the imaging space without the removal of too many events, one method could be to truncate the imaging FOV. Truncated FOV imaging has been employed for many medical applications where the FOV is much larger than the expected source distribution, or the source location is well known prior to the image reconstruction [7], [76], [79]. In the case of 3D position sensing CZT detection systems, there is no restriction, collimation, or preference to the incident direction of the incident gamma rays. Because CZT can record events from any direction 4π Compton cone reconstructions are projected back to the imaging space about the detector and are used for MLEM imaging [33]. 4π imaging has proven to be very useful in unknown source localization and far distanced imaging [14], [80], [81]. However, in cases such as proton beam range verification, where submillimeter resolution is desired and the expected FOV is well defined given the patient or target parameters, 4π imaging can be computationally expensive. In these scenarios the desired FOV is much smaller than the given 4π space but requires many pixels to achieve the resolution requirements, meaning conventional LM-MLEM will spend unnecessary computational time reconstructing an image in space where the source is not expected to be seen. Reconstructing that imaging space greatly increases the size of the data system matrix

when convolving the total number of reconstructed Compton cones with the number of pixels required to achieve a high-resolution result over the entire imaging space.

Truncating the image space will discard events that do not reconstruct to the desired FOV, require less pixelation for the same imaging resolution, aiding in the improvement in the image reconstruction of the source distribution. Table 4.1 shows the trend in the time to reconstruct the 1st iteration or image estimate for the same measured data over varying FOV sizes. For each FOV less than 4π the azimuthal and polar dimensions are equal.

Image size ($\Phi = \theta$)	Num Pixels	Reconstruction time (s)	pixel resolution (cm)
360°	720	1450.8	0.8
180°	606	749.9	0.05
90°	328	29.09	0.05
60°	222	25.06	0.05
45°	168	11.77	0.05
30°	112	8.87	0.05

Table 4.1: Time to reconstruct the first iteration of the same photon data for varying FOV sizes.

However, when applying standard MLEM to reconstruct a space too small about the detector, there will be artifacts along the edges or in the corners of the new FOV.

4.4.1 Corner Convergence Error

When using MLEM as an approach for imaging a space smaller than 4π , the image could become susceptible to artifacts along the edges or corners of the image. These artifacts affect the detection of the real source as they increase in intensity with each iteration of MLEM. Events such as chance coincidence, charge sharing, pair production, partial energy deposition events, or mis-

sequenced events can all lead to corner and edge artifacts where the rings produced from these events are cropped when intersecting in the smaller FOV.

Figure 4.3 demonstrates the error in the amplified corner convergence of the MLEM reconstructions when sizing down the imaging space for the reconstruction of 718 keV photopeak events using an imaging space truncated to $60^\circ \times 60^\circ$ about the hotspot.

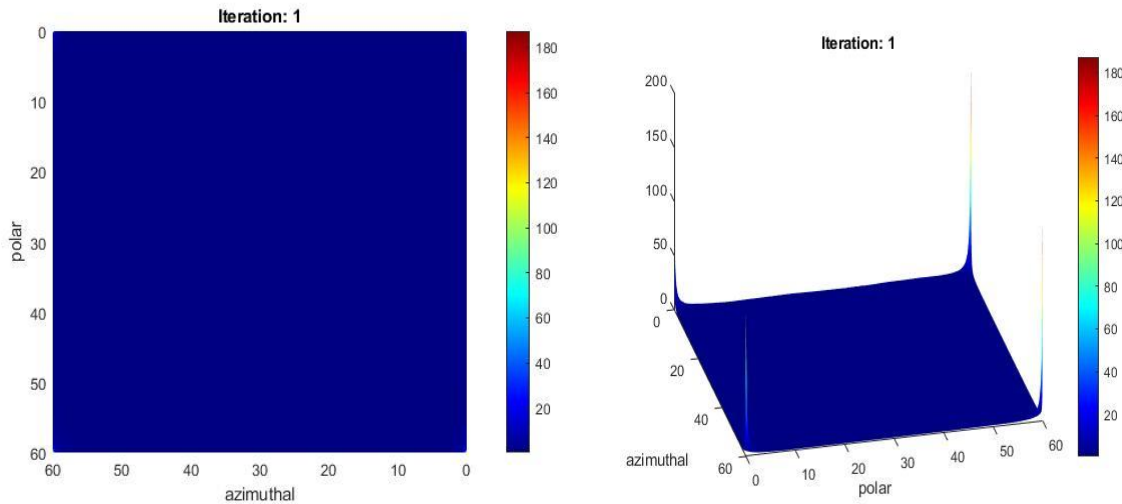


Figure 4.3: MLEM reconstruction of a truncated imaging space using the 718 keV photopeak in a $60^\circ \times 60^\circ$ FOV. The image is turned axially to show the image in depth accentuating the corner artifacts (right column).

Although the image seems uniformly low across the entire FOV, except in the corners, there is valuable data within the pixels. To assure that there is data within these image reconstructions the outermost 10 pixels are removed along the edges of the image in Figure 4.4. This removed less than 3° overall along each side of the image and allowed for the removal of the strong corner artifacts and the rescaling of the intensity of the image to a much lower value.

Figure 4.4 shows that there is valuable information about the source location in these truncated imaging spaces but was heavily diminished by the amplified corner/edge artifacts when using standard LM-MLEM. For example, when comparing iteration 15 from both the 60° and the 40° image reconstructions, one can see there are very strong artifacts along the top of the 40° image that are not seen about the source location from 50° to 10° in the 60° image.

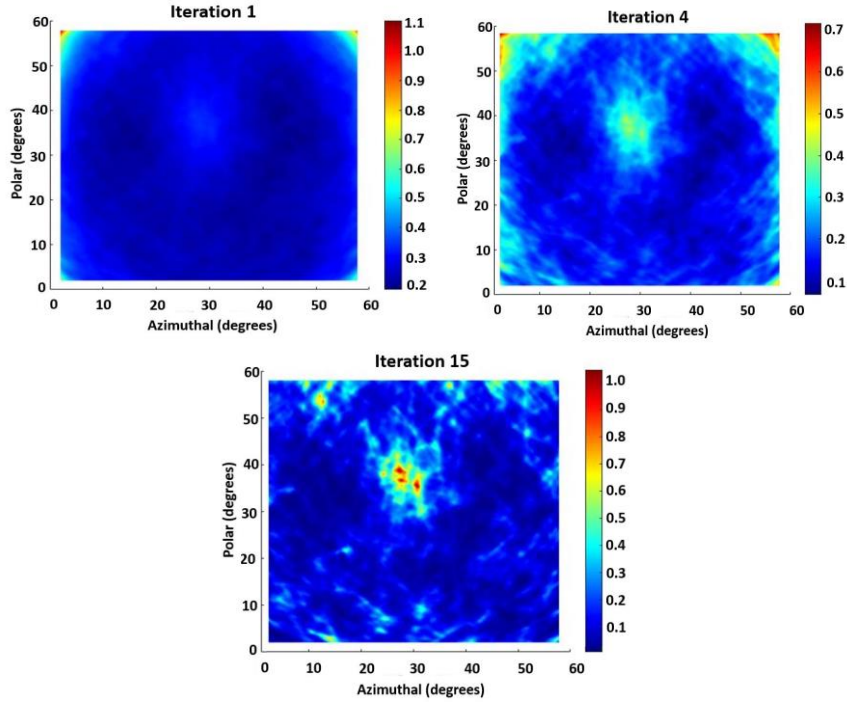


Figure 4.4: MLEM reconstructions of truncated imaging spaces using the 718 keV photopeak. The 10 outermost pixels are removed along the edges of the $60^\circ \times 60^\circ$ imaging space, reducing the FOV to $57.8^\circ \times 57.8^\circ$. (*Proton beam profile enters the target with respect to the image from top to bottom*)

As the FOV reduces in size, the corner and edge convergence become more prominent and completely diminishes the reconstruction of the true source distribution, as the corner artifacts increase in intensity with each iteration. This convergence is due to an ill-weighting of photon events that result in large portions of the Compton rings not being accounted for in the system

matrix of the truncated FOV. This phenomenon can be explained by breaking the updated LM-MLEM equation into two components:

1. *Back Projection*: This is the summation of all measured events or the mean expectation of the total number of photons emitted from each pixel.
2. *Forward Projection*: This is the sum value of each Compton cone based on the previous iteration, or the likelihood estimation for each event.

4.4.2 Back Projection Analysis

The back projection is defined as:

$$\sum_{i=1}^I \frac{t_{ij}}{\sum_{j'=1}^J t_{ij'} f_{j'}^n} \quad (4.14)$$

which sums the value for all events of each matrix element, t_{ij} , divided by the forward projection.

If the first projection or initial estimate of the source distribution, is uniform, that is, $f_j^n = f_j^1 = 1$, then this means that the initial estimate of the source distribution is equal for all pixels in the image space. Therefore, the first iteration of MLEM is equal to the back projection of all the Compton rings calculated from the list-mode events. Figure 4.5 shows the back projection over all pixels, J , in a 4π imaging space and in a 60° FOV for the same list-mode data of experimental 4.44 MeV photon events, from a PuBe source, recorded by CZT.

When comparing the first iteration of the back projection for the 4π projection to the 60° projection, the 4π projection shows a hotspot for the source distribution and other Compton rings in the image space that are developing noise artifacts, but the 60° FOV results in a uniform back projection with amplified peaks at the corner.

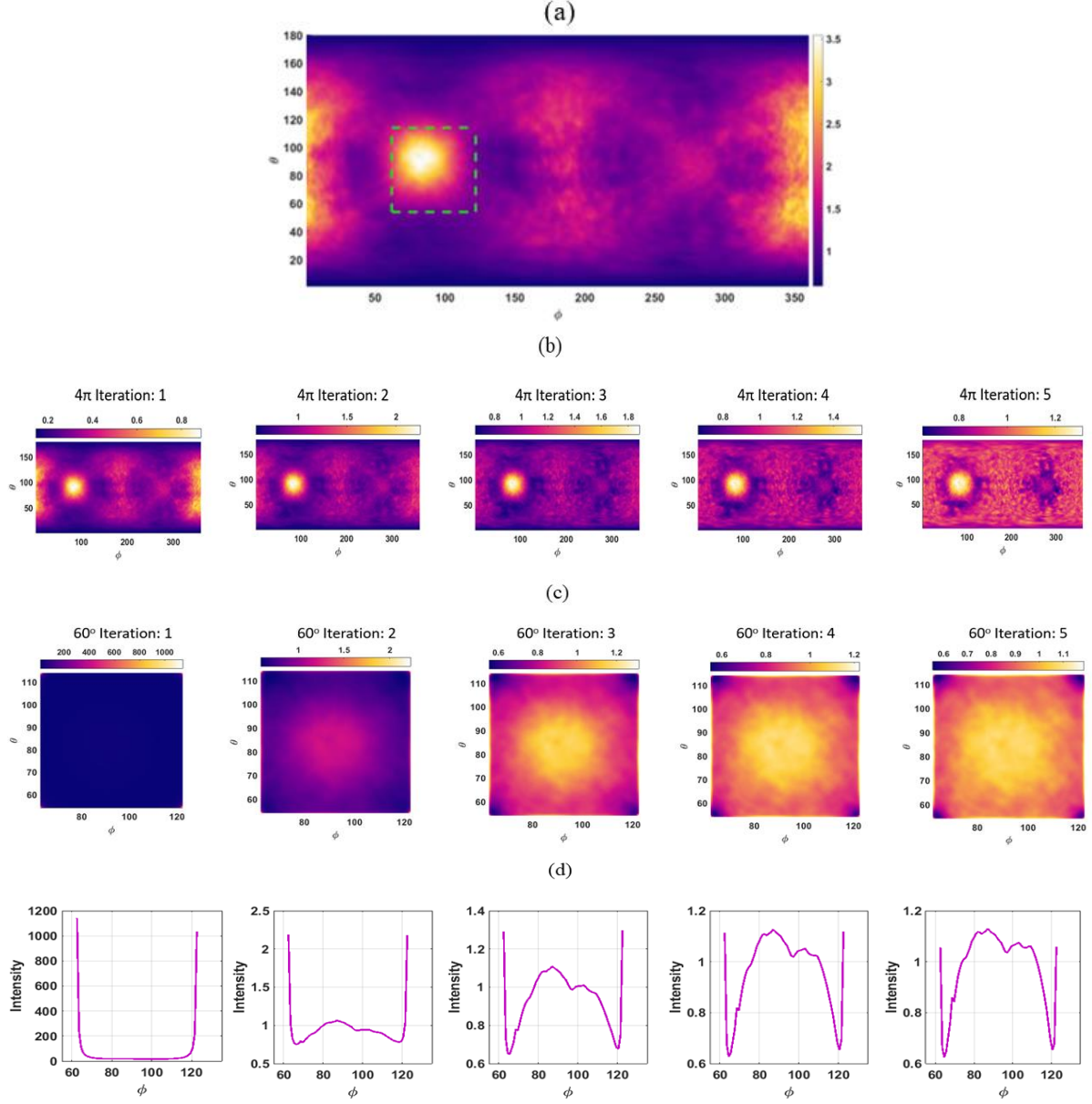


Figure 4.5: (a) The 1st iteration of a 4π MLEM image reconstruction of 4.44 MeV photons from experimental PuBe data. (b) The back projection of all Compton rings in the 4π space, developed using (4.14), prior to reconstructing the first iteration. (c) The back projection in a truncated 60° FOV of all Compton rings that intersect the FOV outlined by the dotted green line in (a). (d) A line plot of the intensity along the first row each back projection shown in (c), highlighting the sharp corner convergence at 62° and 122°

Referring to Figure 4.5(d), the line graph represents the top row of pixels in the 60° FOV, showing that for the first back projection, the intensity of the image is maximized at the corners and begins to stabilize around a maximum intensity of one, with each iteration. The intensity color

bar for the 4π back projection shows a mean expectation up to a maximum value less than 1, as expected, since the initial image estimate is set to one for all pixels. However, the initial estimate of the background summation in the 60° FOV sharply increases to a very high value. The following iterations in the truncated FOV subsequently drop to a lower probability estimate as shown by the color intensity bar, at attempts to reflect the more accurate estimation of the source distribution in the image space. However, the estimation of the source distribution in the subsequent back projections have no effect on the final image reconstruction, which is dominated by the mean expectation estimate of the first calculation of the back projection prior to the first iteration, where the convergence points to the corners of the truncated image space as the most likely location of the source distribution.

To investigate the cause of the increasing value of the corners in the back projection of the truncated field of view, analysis of the forward projection step of the MLEM equation is needed, as this convergence is most prominent in the first iteration.

4.4.3 Forward Projection Analysis

The forward projection contributes to the likelihood estimate of each Compton event used for calculating the back projection,

$$\sum_{j'=1}^J t_{ij'} f_{j'}^n, \quad (4.15)$$

and provides an estimate of the probability for each, as a function of the previous source distribution estimate. Any truncation of the FOV from 4π will alter the projection of each Compton ring in the smaller imaging space. Thus, the value of each forward projection would change due to the change in the FOV. If the FOV is truncated, so will parts of the Compton ring that do not intersect the new image space. Such truncation would lead to inaccurate estimates of the

probabilities. The truncated information still defines the probability of the source distribution for that reconstructed photon event, however, is not accounted for in the smaller FOV using LM-MLEM. The truncation of the Compton ring causes the forward projection to deviate from the original probability density of the ring in 4π . This deviation can lead to two possible limits as the forward projection is calculated for each event, i , over all pixels within the redefined image space:

$$\text{Limit 1: } \sum_{j'=1}^J t_{ij'} f_{j'}^n \gg 1$$

$$\text{Limit 2: } \sum_{j'=1}^J t_{ij'} f_{j'}^n \ll 1$$

Limit 1 occurs when the reconstructed Compton ring is truncated such that majority of the pixels in the truncated FOV are within the most probable locations of the Compton ring. For example, this limit can be approached for a ring that is very wide due to gaussian blurring caused by large uncertainty in the event energy deposition or sequencing.

Limit 2 is often associated with events that reconstruct near the edges or in the outer perimeter of the truncated FOV. In this case the trailing end of the Compton ring's Gaussian curve is reconstructed within the smaller imaging space. This outermost edge of the Compton ring is the least likely location that the photon could have originated from and very few pixels of the truncated space will reflect these lower probability estimates, depending on how far away the Compton ring is projected outside of the truncated image space.

Figure 4.6 is a 2D histogram of each Compton ring's (reconstructed in Figure 4.5) forward projection value as a function of the pixels it intersects in both the 4π imaging space and the 60° FOV. Normalizing each forward projection value bin by the number of events recorded between each limit shows the significant disparity between the likelihood estimate of the forward projection for the same Compton rings reconstructed in a 4π image space and the 60° image space. When imaging in 4π , all reconstructed Compton cones result in a forward projection estimate value

greater than one. When truncating the image to 60°, the likelihood estimate predicted by the forward projection of many of the events shift to values much less than one. Simply discarding events that result in a low forward projection probability estimate may prove to be disadvantageous as many of those partial Compton rings can contribute to the characterization of the source distribution. The majority of these low probability events in the truncated imaging space are reconstructed to the outer most pixels (at 62° and 122° in the polar and at 54° and 114° in the azimuthal). However, there is at least 17% of these events that are reconstructing to the inner pixels of the truncated FOV in the azimuthal direction and at least 23% in the polar direction.

In both limit scenarios the forward projection for each of these types of events will result in an improperly weighted back projection where all pixels corresponding to the Compton ring's location will falsely approach a value of one. That is to say,

$$\frac{t_{ij}}{\sum_j^J t_{ij} f_j^n} = \frac{(values(j) \gg 1)}{Cone\ Sum\ value \gg 1} \approx 1\ for\ all\ j$$

or

$$\frac{t_{ij}}{\sum_j^J t_{ij} f_j^n} = \frac{(values(j) \ll 1)}{Cone\ sum\ value \ll 1} \approx 1\ for\ all\ j.$$

While on the other hand, events with a forward projection estimate in between the limits, or those Compton rings that reconstruct perfectly within the truncated FOV, will be properly weighted, but result in a value less than one. The final calculation of the back projection, in the truncated space, will then correspond to the location of the limit bound events only, which are most likely to reconstruct in the corner pixels of the image space, as shown by Figure 4.6.

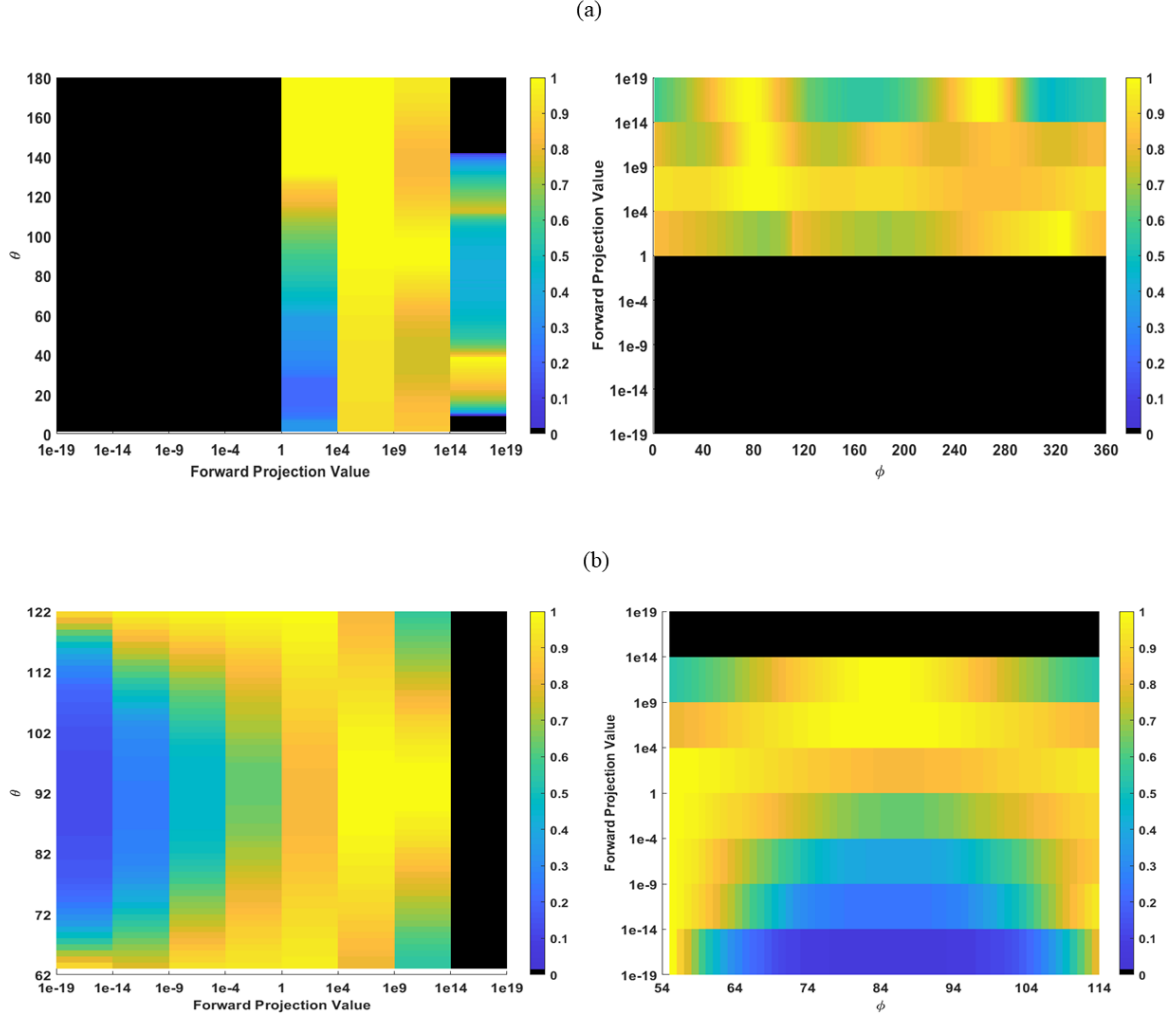


Figure 4.6: (a) A 2-D histogram of the forward projection value calculated using (3) for each Compton ring reconstructed in 4π shown in Fig.1(a). (b) A 2-D histogram of the forward projection value of all Compton rings intersecting the truncated 60° FOV. The forward projection value is binned in the azimuthal and polar directions for each pixel that the Compton ring intersects. All blacked out regions indicate that zero of the Compton rings resulted in a forward projection value of that magnitude in the respective pixel locations.

4.5 ROI-MLEM

Imaging within a specified ROI will allow for analysis of events that only reconstruct within the desired location, and in doing so enhance the algorithmic convergence to the expected source location. However, to achieve a clear representation of the estimated source distribution using

MLEM, some modifications are needed to the algorithm to compensate for the truncation of the Compton rings in the smaller FOV.

In this work, ROI-MLEM was developed to reconstruct only the Compton rings that intersect a desired region within the 4π imaging frame about the detector, allowing for enhanced pixel resolution and reduced computational cost when comparing to standard MLEM for a 4π space with the same resolution. Implementing ROI-MLEM, the computational expense of the iterative process will be reduced as the high-resolution needs depend only on the pixelation of the ROI and not the entire 4π FOV. Therefore, the system matrix size required for ROI-MLEM is much smaller in comparison to 4π imaging for the same resolution, as we are not only reducing the number of overall image space pixels but the number of events that will have nonzero values, as there are a smaller number of events crossing the truncated space. The methodology of ROI-MLEM adapts that of Ziegler et al in which a mask is applied to a 4π FOV to allow for reconstruction of the ROI alone [76]. Derivation of ROI-MLEM deviates from Ziegler's application in that the Poisson nature of Compton rings precludes subtraction of the unwanted image space about the defined ROI.

Erroneous convergence to the amplified values at the corners of the image space, when using MLEM in a truncated FOV is in part due to the ill-weighted probability of each Compton ring that partially intersects the truncated FOV and produces an incorrectly amplified estimate in the image space. The algorithm needs to be revised to compensate for the full probability of each Compton ring regardless of its appearance in the region of interest or truncated FOV. Thus, the ROI-MLEM reconstruction method is based on the reframing of the MLEM algorithm shown in equation 4.13, where the system matrix for each event must be defined in two parts. One part defines the event probability (Compton ring) within the ROI and the second part defines the same

event in 4π which will be denoted as the ‘background’. The forward projection of the standard algorithm can then be broken into the summation of two components:

$$\sum_{j'=1}^J t_{ij'} f_{j'}^n = B_i + \sum_{j'=1}^{J^R} t_{ij'}^R f_{j'}^{n,R}. \quad (4.16)$$

This restructuring of the forward projection allows for the iterative update of the source distribution within a smaller imaging space. Here, $t_{ij'}^R$, defines the ROI system matrix elements, or the probability that the detected event originated from pixel j of the ROI space. The ROI can then be imaged using a fine pixel mesh grid, where $j \in \{1, 2, \dots, J^R\}$, where J^R is the total number of pixels defining the ROI space. Redefining the forward projection enables high spatial resolution imaging for the desired ROI space alone.

The background is summed as a scalar value for each photon event, B_i , and is expressed as,

$$B_i = \sum_{k=1}^K \mathbf{f}_{k,\text{mask}}^B t_{ik}^B. \quad (4.17)$$

Equation 4.17 is the sum value of the background system matrix, t_{ik}^B , which is the probability of each event over a coarse mesh of K pixels in the 4π space, where $k \in \{1, 2, \dots, K\}$. This is multiplied by $\mathbf{f}_{k,\text{mask}}^B$, which is the projection of the background image space. The final equation of the ROI-MLEM algorithm is expressed in 4.18, and now updates over the ROI space alone as the rest of the 4π space is accounted for in B_i :

$$f_j^{R^{n+1}} = \frac{f_j^{R^n}}{S_j^R} \sum_{i=1}^I \frac{t_{ij}^R}{B_i + \sum_{j'=1}^{J^R} t_{ij'}^R f_{j'}^{R^n}}, \quad (4.18)$$

where, s_j^R , represents the sensitivity of the detector system to the photons emitted from all pixels in the ROI and $f_j^{R^n}$ is the source distribution estimate image vector that is now a function of the ROI space alone.

4.5.1 Background Constant

The background projection, $\mathbf{f}_{k,\text{mask}}^B$, is the product of the reconstruction of the first ML iteration or back projection, using the standard ML equation, of each event, i , in the background FOV, by an apodizing mask that is formed by convolving a uniform mask and a \cos^2 function that allows for a smooth transition to the ROI space in which the pixel values are zeroed, similar to Ziegler [76]. Creating this mask, ensures that the drastic change in the probability density function of the Compton ring in the background and the ROI space does not create artifacts at the edges of the ROI. Figure 4.7 depicts the development of $\mathbf{f}_{k,\text{mask}}^B$ for the image reconstruction of a simulated gamma-ray point source.

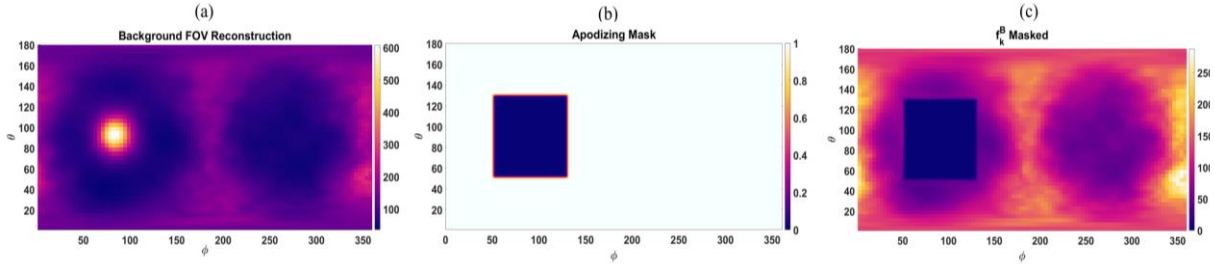


Figure 4.7: (a) 1st LM-MLEM iteration of the background FOV which is multiplied by the (b) apodizing \cos^2 mask that smoothly transitions to the ROI where all pixel values go to zero in the (c) masked background projection.

The purpose of the background constant, B_i , is to suppress the ill-weighted Compton rings that intersect the ROI space in only the edge and corner pixels. The background constant is only calculated to provide the initial probability estimate of each Compton ring, this ensures that the probability of each event in the 4π space is accounted for as we iterate over the smaller imaging space. The Compton rings intersecting in the edges or corners of the ROI will be associated with

a large constant, as opposed to those Compton rings that fully reconstruct in the ROI that will correlate to a low background that will not suppress the overall estimate of that event in the ROI imaging space.

4.5.1.1 Apodizing Mask Considerations

When selecting the ROI from the 4π imaging frame the edges of the ROI must be smoothly transitioned from the background 4π imaging pixels, such that the transition in data from those edge pixels do not become amplified in the image reconstruction. This allows for the ROI to be reconstructed without causing any artifacts along the edge of the ROI frame. For this work, a uniform mask slightly larger than the dimensions of the ROI is created then convolved with a \cos^2 function such that the values in the center remain at unity corresponding to the exact dimensions of the ROI and the edge pixels of the mask transitioning into the background space fall to zero. An example of this is dramatized in Figure 4.8 which would be employed like the example shown in Figure 4.7.

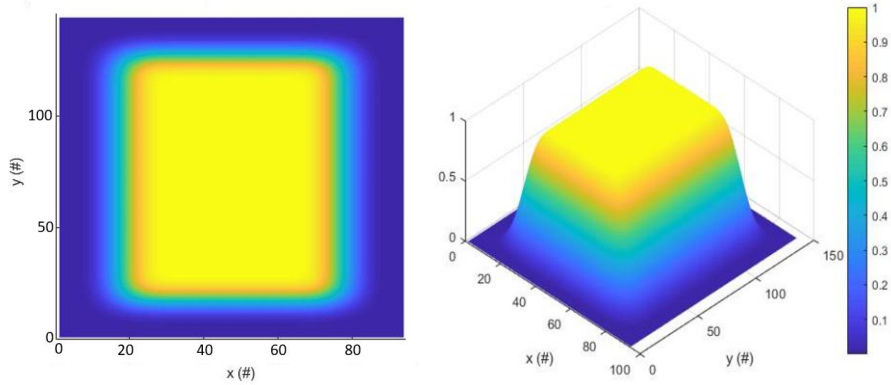


Figure 4.8: Exaggerated Cosine Apodizing Mask

This mask can be used as the first estimate of the source distribution, $f^{1,R}$, and then inverted and applied only to the background system matrix used for the background constant, f_k^B , evaluation.

4.5.2 Comparative Analysis of Standard MLEM and ROI-MLEM

All image reconstructions shown using ROI-MLEM are chosen based on the iteration with the max SNR value,

$$\text{SNR} = \frac{P_{\text{signal}}}{P_{\text{noise}}}, \quad (4.19)$$

where, P_{signal} is the summed value of all pixels in the image that correspond to a signal value of at least 50% of the max intensity of the image, normalized by the number of pixels that are at least 50% of the max intensity. P_{noise} is the standard deviation of all remaining pixels in the image that have a value less than 50% of the max intensity of the image.

To compare standard LM-MLEM SNR to the ROI-MLEM SNR the signal pixels of the LM-MLEM reconstructions are chosen from the inner most pixels of the image excluding the outer edge pixels. This alleviates the signal being read as only the corners and allows for evaluation of the source distribution calculated by MLEM.

4.5.2.1 Simulation and Experimental Cs 137 Results

For proof of concept, image reconstructions of a simulated 10 cm Cs¹³⁷ line source are compared using both MLEM and ROI-MLEM in a 90° FOV. Using the 662 keV energy line ensures a noise-less simulated data set for CZT detection, which should favor the image reconstruction using both ROI-MLEM and standard MLEM. Both reconstruction methods used 40,000 photopeak events in an energy window of 657 keV to 667 keV and utilized 300×300 pixels for a pixel resolution of 0.3°. Figure 4.9 shows the image reconstruction for the 22nd iteration of both the ROI-MLEM and MLEM.

The image reconstructions show that the ROI-MLEM algorithm results in a clearer and more uniform representation of the simulated line source. At the same iteration, MLEM starts to break apart the source distribution, causing noise artifacts that deviate from a single uniform source

distribution. which could be due to the altered convergence rate of MLEM in the truncated space, which focuses on the amplified corners. It should also be noted that the ROI-MLEM reconstruction shown in (a) of Figure 4.9 does not eliminate the corner convergence but controls the value of those pixels allowing for a better estimation of the true source distribution, whereas the LM-MLEM image shows that the corners have a value an order of magnitude higher than what is estimated for the source.

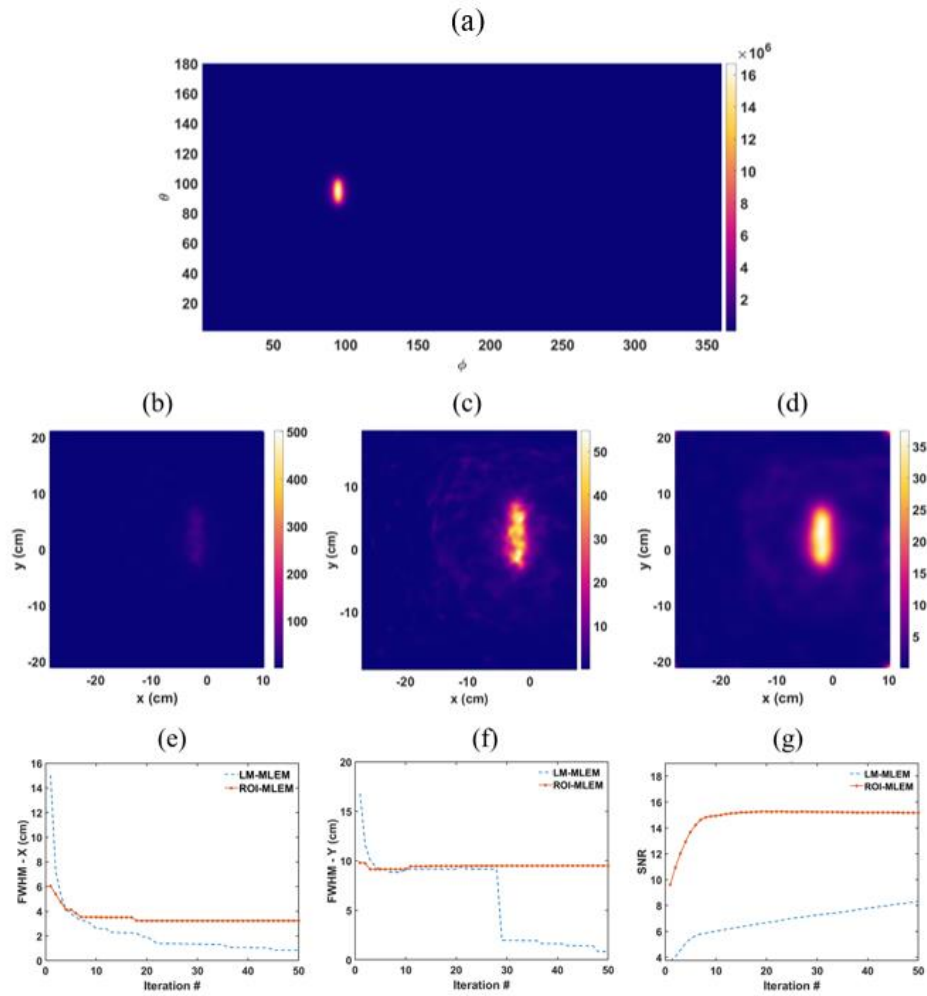


Figure 4.9: (a) 4π image reconstruction, (b) LM-MLEM, (c) LM-MLEM with the outermost 10 edge pixels removed, and (d) ROI-MLEM, 22nd iteration reconstructions of a simulated 10 cm Cs^{137} line source. (e) and (f) compares the FWHM values in the Y and X directions, respectively of (c) and (d) reconstructions, for both imaging algorithms, and (g) compares the SNR values for 50 iterations of both methods.

Method	SNR	FWHM-X (± 0.28 cm)	FWHM-Y (± 0.28 cm)
LM-MLEM	6.77	1.40 cm	9.17 cm
ROI-MLEM	15.28	3.24 cm	9.49 cm

Table 4.2: Comparison of the SNR and FWHM of the image reconstructions developed using LM-MLEM and ROI-MLEM of the 10 cm Cs¹³⁷ line source simulation. The FWHM error is taken as twice the pixel pitch.

The full 4π reconstruction shown in Figure 4.9 (a) shows that the source distribution is more comparable to that of the ROI-MLEM reconstruction.

Table 4.2 indicates the FWHM values in both directions taken through the peak centroid of each image reconstruction and the SNR value for the 22nd iteration shown in Figure 4.9. ROI-MLEM results in a closer estimate of the sources true length but a wider estimate in the x-direction of its width. This could be due to the inherent gaussian uncertainty of the Compton rings in the near field [33], and ROI-MLEM enhancing those rings that converge within the ROI and not near the edges. Although the MLEM reconstruction results in a thinner line source it suffers from a poorer uniformity in the sources intensity which also affects the fit applied to the FWHM calculation. With each iteration the FWHM and SNR calculations for the LM-MLEM reconstruction is unstable and does not plateau which can lead to complications when choosing the best iteration, whereas the ROI-MLEM convergence does plateau indicating that further iteration does not improve the image.

Comparatively, ROI-MLEM is used to image experimental Cs¹³⁷ data. Four experimental one-hour Cs¹³⁷ check source measurements were taken with a source-to-detector distance of 30 cm away from the H3D S400X system (see chapter 2 for system details). The source was measured at

a stationary position in front of the detector and then moved to the right by 3 mm, 5 mm, and 10 mm for each additional one-hour measurements.

The optimal ROI-MLEM iteration reconstructions, based on the SNR value, are shown for each measured position of the Cs¹³⁷ source in Figure 4.10. Iterations 25, 25, 26, and 27 resulted in the max SNR iteration for the “No Shift”, “3 mm”, “5 mm”, and “10 mm” reconstructions, respectively. The ROI is designed as a rectangular frame spanning 60° in the polar and 90° in the azimuthal, utilizing 300 × 450 pixels resulting in a 0.3° (0.02 cm²) pixel resolution.

The reconstructions show that the position resolution is not fine enough to separate the sources if they were reconstructed in the same image, as the average FWHM in the X-direction (left to right) for each measurement is 4.93 cm ± 0.04 cm. The FWHM of each source reconstruction is much larger than the shift increments as seen in (c) of Figure 4.10.

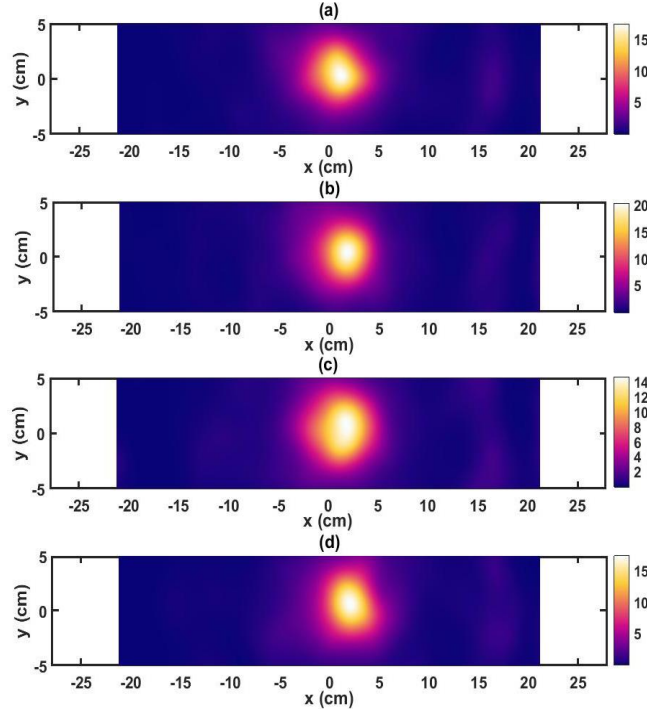


Figure 4.10: ROI-MLEM reconstructions of the Cs^{137} shifted source measurement. (a) No Shift, (b) 3 mm shift, (c) 5 mm shift, (d) 10 mm shift.

However, taking a 1D slice through the peak centroid shows that the source's location can be estimated from taking the difference between the no shift estimate and the shifted measurements peak centroid values in Table 4.3, derived from Figure 4.11. For each slice, a Gaussian fit is applied and the peak location of both the data and the fit are compared. The average error based on the three shifted source locations is 1.7 mm and 1.4 mm for the Gaussian fit and data curve, respectively.

Shift	Peak Location (mm)		Difference (mm)	
	Fit	Data	Fit	Data
No Shift	11.5	12.6	--	--
3 mm	17.3	16.8	5.8	4.2
5 mm	18.2	18.9	6.7	6.3
10 mm	21.0	21.0	9.5	8.4

Table 4.3: Source distribution location estimation based on the peak centroid location in the x-direction of the 1D profiles of the image reconstructions shown in Figure 4.11

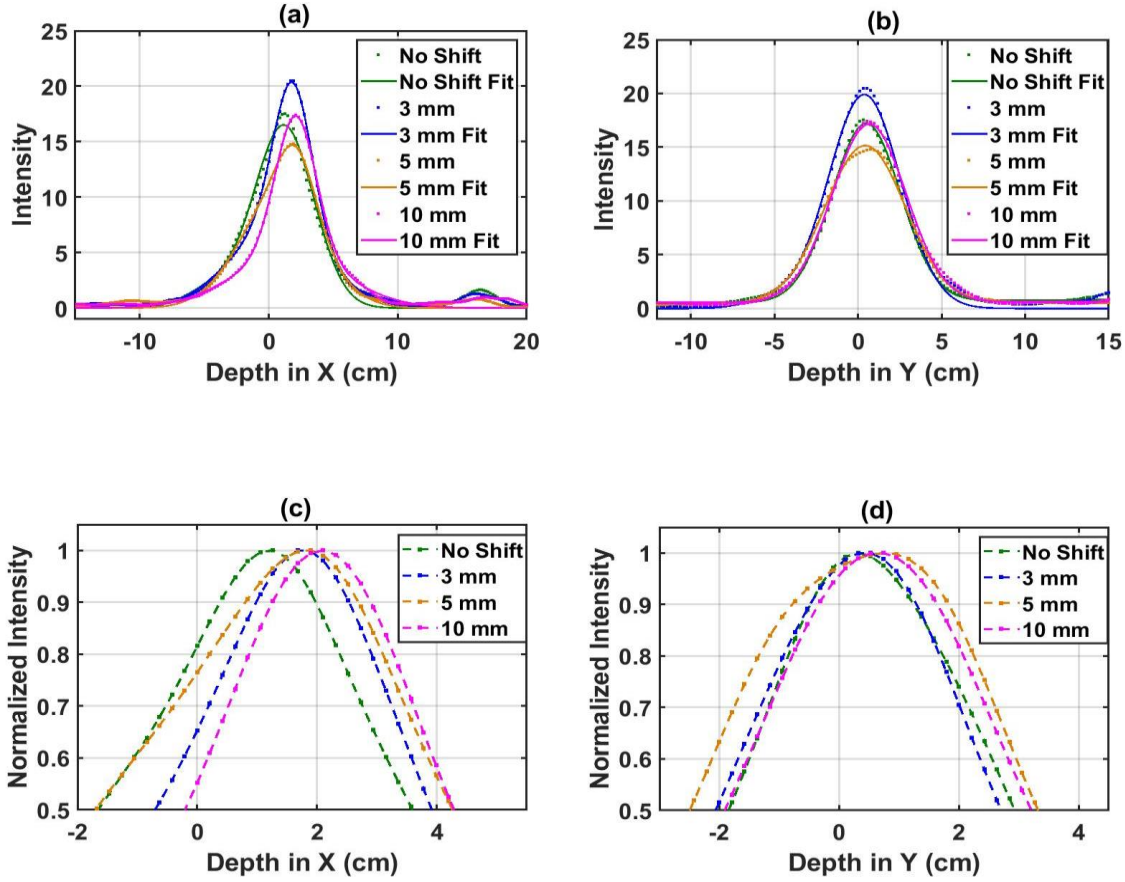


Figure 4.11: 1-D profiles through and Gaussian fit of the peak centroids in the X (a) and Y (b) directions for the image reconstructions shown for the Cs^{137} shifted source measurement. (c) and (d) shows the top 50% of the intensity normalized by the peak value in the X and Y directions, respectively.

ROI-MLEM has shown its capability to reconstruct a simulated extended source well enough to provide an estimate of the source shape and extent with an absolute error of 5.1%. This algorithm also shows its usefulness in estimating source location with submillimeter pixel resolution, resulting in an average 1.7 mm error when applying a Gaussian fit. The following subsection discusses the application of ROI-MLEM on more complex data sets where the noise in the event reconstruction affects the source distribution in the rendered image reconstruction.

4.5.2.2 High Energy and High Flux Applications

The capability of imaging 4.44 MeV photons using ROI-MLEM was tested from a PuBe source measurement taken with the S400X system at a 30 cm distance over the span of 6 hours. The PuBe source was placed in a thin lead source holder and was shifted 1 cm to the right halfway through the measurement, the other detector plane was placed as close as possible to the PVC to detect more of the 6.1 MeV events, the detection setup is pictured in Figure 4.12. For the image reconstruction of the PuBe source, only the single module events from the detector directly facing the source were used for image reconstruction.

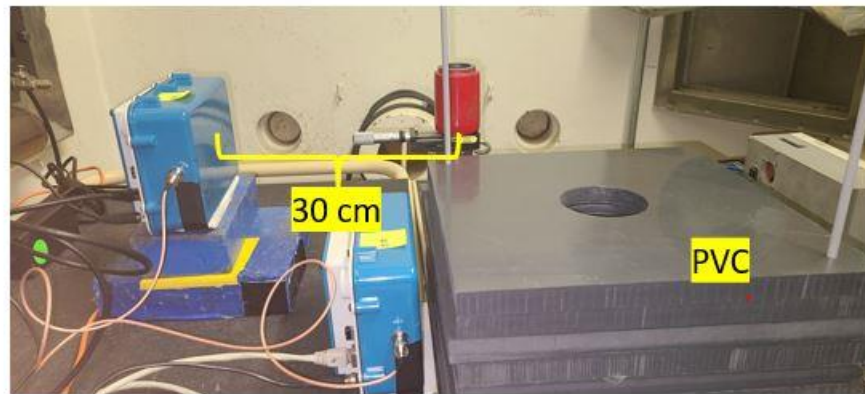


Figure 4.12: PuBe source measurement setup.

Figure 4.13 shows the recorded energy spectra from both modules before (left) and after (right) shifting the source, highlighting the degradation in energy resolution at the 4.44 MeV photopeak.

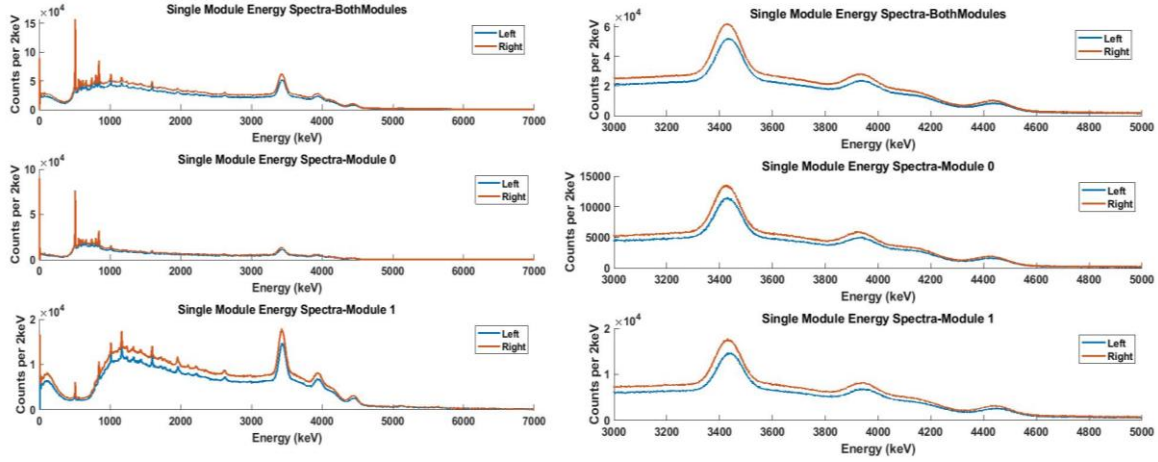


Figure 4.13: Single module events energy spectra from PuBe measurements. The 4.44 MeV photopeak and escape peaks are focused on in the spectra to the right.

Figure 4.14 shows the image reconstruction of the PuBe source for both the left and right position reconstructed in a 4π FOV and a ROI space, $90^\circ \times 90^\circ$. The ROI-MLEM reconstruction mitigates the interference of the noise artifacts seen in Figure 4.5 (a) which displays the 4π image reconstruction using standard MLEM.

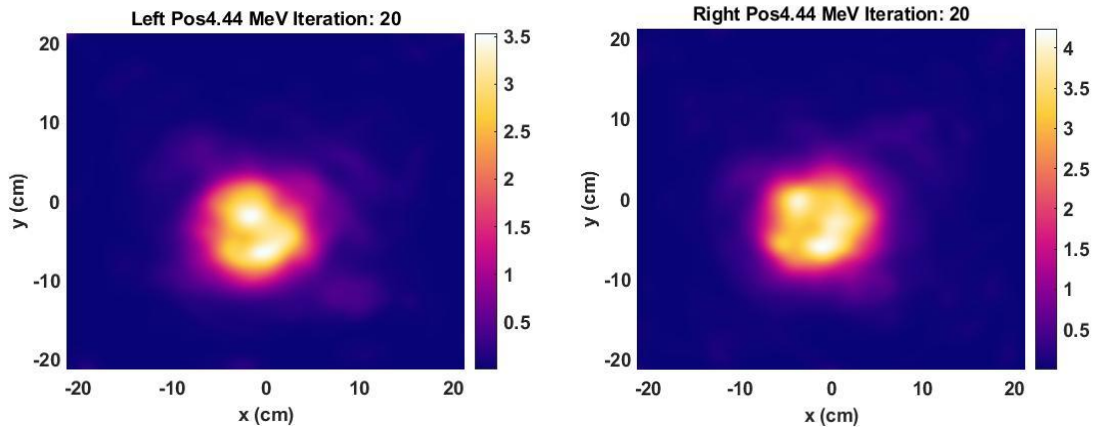


Figure 4.14: ROI-MLEM image reconstruction of the 4.44 MeV photopeak from Mod 0 for both the left and right positions of the PuBe source.

Computationally, the 4π image reconstruction is limited to a pixel resolution of 0.8 cm for an imaging radius of 30 cm, making it impractical to use for measuring the 1 cm shift of the

extended PuBe source. Using the ROI images a 1-D slice through the peak centroid along the x-axis can be taken to measure the reconstructed shift of the source from the location of the peak in each image, as shown in Figure 4.15. The images show that we can reconstruct 4.44 MeV photopeak images and see at least a 1 cm shift of the source at a 30 cm distance. The 1-D slice plot shows that the shift of the peak centroid is 0.93 cm which results in a 7% error of less than 1 mm.

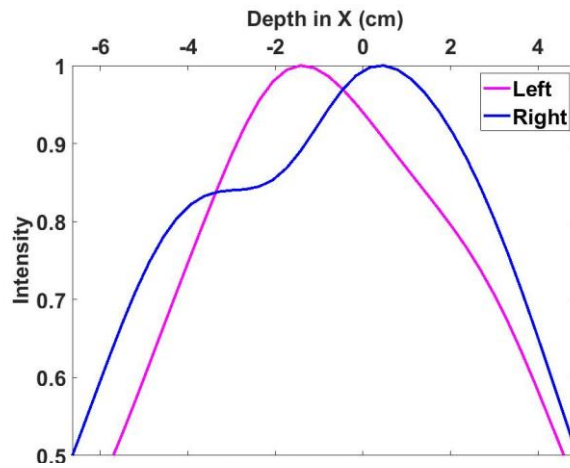


Figure 4.15: 1-D Slice through the peak centroid of both ROI-MLEM reconstructions shown in Figure 4.12.

The PuBe source used in this example exceeds 10s of Curies but is for the most part monoenergetic and did not saturate the detection system. However, the following chapter will show the complications of imaging high flux photons that range in energy from several hundred keV to 10s of MeV.

4.5.2.3 Computational Performance

Table 4.4 reflects the reduction in computational expense when reconstructing the 4.44 MeV photopeak events using ROI-MLEM. The time to reconstruct the first iteration is reduced by 61% when comparing the 4π reconstruction from Figure 4.5(a) to the ROI image reconstruction in Figure 4.14(a) of the left side measurement, using the same number of events. The 4π image

reconstruction pixel resolution is limited by the computational constraints of the computing system used for this work, however, is comparable to the resolution of the other tested imaging frames. When comparing the same 90° FOV reconstructions using standard MLEM and ROI-MEM, the timing and computational use differs slightly, ROI-MLEM being greater due to the computation used for the background system matrix constants, which is only computed once, and the values are stored for use in the following iterations. The background constant, used for the images shown in Fig. 8, is calculated using a 40 pixel resolution (4050 pixels over a 4π space). This calculation can be optimized for each imaging problem, based on resolution requirements, and improving accuracy of estimating the Compton ring, adding little expense in the computation.

Here we have seen ROI-MLEM prove to be particularly useful in imaging high energy sources, providing submillimeter accuracy, and shortening image reconstruction time.

	# Of Pixels ($\Phi \times \Theta$)	Pixel Res.	Time (s)	RAM Usage†
MLEM 4π	720×360	0.5°	338	41.3%
MLEM 60°	120×120	0.5°	21	10.0%
MLEM 90°	300×300	0.3°	116	11.1%
ROI-MLEM 90°	300×300	0.3°	132	11.7%

Table 4.4 Computation performance comparison of the time to reconstruct the 1st iteration

CHAPTER V

Proton Beam Range Verification Methods

5.1 Motivation

It has been proposed that the gamma rays emitted during proton beam therapy could be of diagnostic value in understanding the energy deposition of the proton along its path. For proton therapy, the 4.44 MeV gamma-ray emitted from Carbon deexcitation, is of particular interest for proton beam range verification (PBRV). The 4.44 MeV photopeak has shown to correlate to the Bragg peak of the proton beam thus giving insight to the location of the largest differential dose deposition [61], [82]. If the image of the 4.44 MeV can accurately describe the location and distribution of the proton beam, this could aid in reducing the uncertainty in the dose deposition of the beam. The risk to nearby healthy organs to the tumor location could also be mitigated and the prompt gamma-ray analysis could potentially aid in the understanding of the radiobiological effectiveness (RBE) of the proton beam as a function of depth in the patient.

However, imaging just the one photopeak has its challenges as the influx of photons created from the proton beam are not monoenergetic. Typically the energy of the emitted photons range in energy from several hundred keV to 15 MeV and have an associated cross-sectional dependency on the target material composition and proton energy [65]. Adding another layer of complexity, is the emission rate of the photons of interest. They are typically referred to as “prompt gammas”, as many are emitted, including the 4.44 MeV from carbon, on the order of picoseconds post proton-nuclei interaction. For a radiation detector, this large range of photon energies coupled with the

fast emission rate, easily causes complications in data collection, mostly due to noise from incomplete energy collection, saturation of the detection system due to timing limitations, and chance coincidence photons causing a misread of multi-photon interactions as single events [32], [73].

The motivation of this work is to discuss and analyze CZT's capability of not only detecting these photons, but methods employed for imaging specific photopeaks and full spectrum analysis to aid in best correlating the prompt gamma ray emission to the Bragg curve profile of the intended proton beam. The ROI-MLEM algorithm derived in Chapter 4 is used as the imaging modality of choice, however, SBP and standard LM-MLEM images are presented when necessary for comparison or to display the extent of the noise created in the imaging domain from prompt gamma-ray detection.

5.2 Prompt Gamma Correlation to the Proton Beam

Theory shows that the gamma-ray emissions from proton beam therapy can provide information about the dose profile of the proton beam given a specified material, with aims to show this correlation *in-vivo* and in real time so that adjustment to the treatment plan can be readily made or verified prior to the patient's therapy treatment [83], [84]. This theory can be realized through the understanding of the proton energy threshold associated with the prompt gamma (PG) emission for a monoenergetic proton beam. In Chapter 3, the proton interactions that cause the emission of prompt gamma rays are detailed and outlined for specific elements that are known to be in the human body. Here we will analyze the dependency of the gamma ray emission on the proton energy by discussing the thick target yield approximation. Understanding the dependency of the emission profile will provide insight when analyzing the geometrical distribution of the gamma-ray emission derived from Monte Carlo based simulations. Analyzing the geometry of the

PG emission profile can aid in comparing the distribution of the photons as a function of energy, proton trajectory, and target material. Building integrity in the correlation of the PG profile to the proton depth profile provides a solid base in the argument that imaging these photons in practice can provide practical information in determining the location and dose profile for clinical practice and safety.

In this text, the problem is contained to a first order degree of difficulty, that is, our target of interest is homogeneous but close to that of human density and composition, (e.g. plastic phantoms, water tanks). Clinically, we would expect the proton beam to travel through different layers of material before coming to rest, which could easily add layers of complexity to our problem given the number of elements and change in density in each material coupled with the change in proton energy. For this reason we focus on the beam trajectory through a single material with the assumption that all protons come to rest in that material. This study is done for the proton beam's profile for multiple materials, namely, high-density polyethylene (HDPE), bone equivalent plastic (BEP), and adipose tissue. Furthermore, the study focuses on monoenergetic pencil proton beams. Although in clinical practice, spread-out Bragg peaks (SOBPs) are desired as they can encompass 3-D volumes thus covering the entire tumor, most SOBPs are achieved by pulsating pencil beams. So it is assumed that the knowledge we gain in theory and experimental analysis from a pencil beam geometry can be readily applied to a SOSP study where multiple beams of different energies are utilized.

5.2.1 Thick Target Yield Approximation Derived from Threshold Energy

The threshold energy to produce nuclear reaction fragments and particles, is the minimum kinetic energy that the colliding particles must have and is always greater than or equal to the rest energy of the desired production fragments, also known as the Q-value. As the accelerated proton

travels through the medium, it will come in contact with various elemental atoms or nuclei which will vary in rest energy all while the incident energy at each collision for the proton is changing. The rapid state of these collisions combined with the change in proton energy can make it seemingly difficult to depict where along the proton's path that a certain particle would be emitted from for a specific collision, provided the energy of the collision is at least at threshold.

In practice, the formation of radioactive particles and other emissions from isotopic reactions with charged particles are defined by a reaction cross-section. Some research takes the approach of experimentally quantifying the thick-target yield (TTY) and production yield with the use of heavy charged particle beams [85], [86]. However, the cross-section values do not give a direct correlation to quantify the gamma-ray emissions that can accompany the reaction of interest. [87]. The difficulty lies in the continuous change in the charged particle energy as it slows down, which complicates the estimation of when particular reactions will occur along its path.

Alternatively, the TTY approximation can be derived as a macroscopic cross-section to provide a correlation between the nuclear reactions and the properties of the target and assess the quantity of particles formed [88]. Here we define the TTY and derive it in terms of threshold energies to provide an approximation of the depth at which the proton reaches the threshold, and the specific nuclear reactions will no longer take place past this depth.

The reaction probability can be defined as,

$$Y = \frac{N_p}{N_i}, \quad (5.1)$$

where N_p and N_i are the number of produced particles and incident particles, respectively. Following Aikawa et al., the TTY can be derived from the differential reaction probability dY at a differential length, dx , in the target,

$$dY = \sigma \left(\frac{\rho N_A}{A_T} \right) dx, \quad (5.2)$$

which is a function of σ , cross-section [cm^2], target density (ρ) [g/cm^3], mass number (A_T) [g/mol], and Avogadro's number (N_A).

Remembering that the stopping power of the accelerated charged particle, is largely in part a function of the target density and particle energy, i.e.

$$S(E) = -\rho \left(\frac{dE}{dx} \right). \quad (5.3)$$

Deviating from Aikawa, we can then obtain the TTY as a function of depth in the target by rearranging the stopping power and substituting it in equation 5.2,

$$\frac{dY}{dE} = -\frac{\sigma \rho}{S(E)} \left(\frac{N_A}{A_T} \right). \quad (5.4)$$

For our problem we are concerned for only the depth at which the projectile reaches its threshold energy, E_{th} . As this tells us approximately where the reaction production ceases as any depth beyond this point results in an energy too low to cause the reaction of interest. Knowing this, we can rearrange equation 5.4 to solve for the TTY as a function of depth.

$$Y(E) = -\frac{\sigma \rho}{S(E)} \left(\frac{N_A}{A_T} \right) dE. \quad (5.5)$$

For the intended goal of associating the TTY with the production of PGs we can utilize the measured cross-section for specific PG reactions, e.g those calculated in [3], making the cross-section a function of the charged particle energy and the target nuclei. We can solve equation 5.5 as a function of differential path length, using the general form of the stopping power, $-dE/dx$,

$$Y(E) = \frac{\rho N_A}{A_T} \sigma_Y(E) dx. \quad (5.6)$$

Here we can solve for the TTY from the projectile's incident energy until the depth at which it reaches the specified E_{th} for our reaction of interest. Aikawa, demonstrates in equation 5.7 that for a given projectile and target material the TTY can be analytically derived as an integration from the incident energy of the projectile, E_{in} , to zero where the incident particles come to rest within the target, with the assumption that the incident beam current is almost constant [88],

$$Y(E_{in}) = \frac{N_A A_p}{A_T} \int_0^{E_{in}} \sigma(E) \frac{1}{S(E)} dE. \quad (5.7)$$

Equating equation 5.6 to 5.7 and integrating from the incident energy of the projectile to its threshold energy provides a means of estimating the depth at which the reactions will stop, occurring in the medium for the specified E_{th} . That is,

$$Y(E_{in} \rightarrow E_{th}) = \frac{N_A A_p}{A_T} \int_{E_{th}}^{E_{in}} \sigma(E) \frac{1}{S(E)} dE = \frac{\rho N_A}{A_T} \int_{x_{th}}^0 \sigma_Y(E_{th}) dx, \quad (5.8)$$

and rearranging and simplifying gives an equation solving for the approximate depth at which the projectile reaches its threshold energy, x_{th} ,

$$\frac{A_p}{\rho \sigma_Y(E_{th})} \int_{E_{th}}^{E_{in}} \sigma(E) \frac{1}{S(E)} dE = -x_{th}. \quad (5.9)$$

Note that the cross-section within the integration, $\sigma(E)$ is simply the cross-section of the reaction across all energies and not necessarily the emission of the PGs, as we have shown in Chapter 3 that different PGs can occur from the same reaction, and multiple reactions can induce the same PG. We also must note here that the cross-section is valid only for proton-nuclei interactions, meaning that they do not consider multi-element compositions but assume a target of one element.

We can use equation 5.9 as a means of estimating the point at which the reactions that causes the emission of specific PGs stop within the target. Knowing where these emissions occur

along the beam path aids in correlating the geometric distribution of the PGs to the beam path and Bragg Curve.

Figure 5.1 gives the estimated, x_{th} , for the 718 keV emission from $^{12}\text{C}(p, x)^{10}\text{B}^*$ as a function of the incident proton energy. The cross-section table from [65] is used and fitted with a 4th power polynomial to estimate the cross-section at various energies, shown in Figure 5.2 and the $S(E)$ is calculated SRIM 2010.

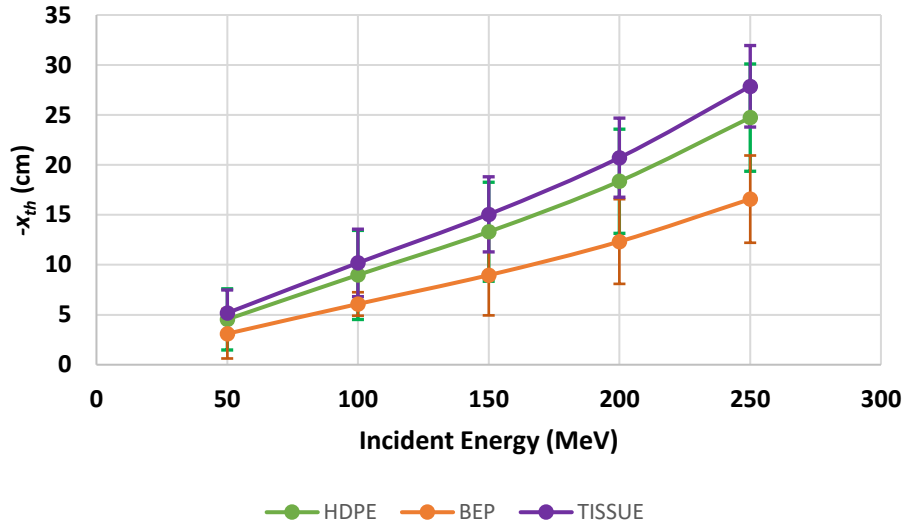


Figure 5.1: Threshold depth estimate based on the 22.1 MeV threshold energy of the $^{12}\text{C}(p, x)^{10}\text{B}^*$, 0.718 MeV emission. The materials estimated are HDPE ($\rho=0.97 \text{ g/cm}^3$), Bone Equivalent Plastic ($\rho=1.82 \text{ g/cm}^3$), Tissue ($\rho=1.03 \text{ g/cm}^3$).

The error in the threshold depth calculation is largely in part due to the incomplete cross-section values and the fit of the polynomial. Another possible reason for the large error bars is that depth of the reaction rate for a proton-nuclei reaction within a multi-element target is being estimated. The cross-section values are based on the single carbon element however the calculations are dependent on the density and stopping power of materials with different concentrations of ^{12}C .

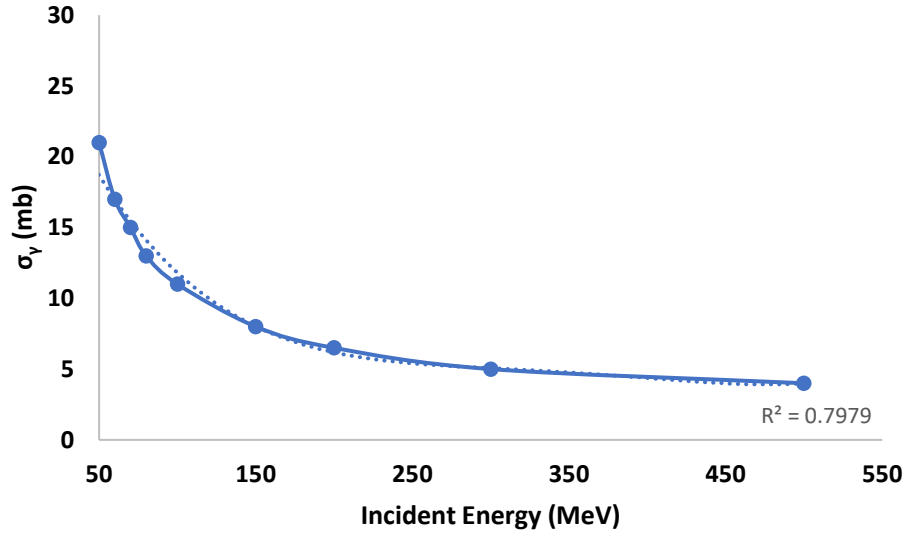


Figure 5.2: $^{12}\text{C}(p, x)^{10}\text{B}^*$, 0.718 MeV Cross-section experimentally given by Kozlovsky [61] . Fitted with a 4th degree polynomial.

5.2.2 Spatial Distribution Analysis

To analyze the spatial distribution of the emission of PGs emitted from proton interactions, both Geant4 (G4) and MCNP simulations were developed. In Geant4 the *Polaris3 – Prompt Gamma Compton Camera Simulation (PGCCS)* developed by Peterson et al. was used to analyze the PG emission from various low Z targets and the detection capabilities of the Polaris J3 system (detailed dimension in Chapter 2). MCNP6 is used in this text to analyze the PG and neutron emissions in the same low Z targets used in the G4 simulations.

Table 5.1 provides the atomic information of each target material studied, (1) HDPE, (2) Bone Equivalent Plastic (BEP), and (3) tissue.

Elements (%)	HDPE ($\rho=0.97$ g/cc)	Bone Eq. Plastic ($\rho=1.82$ g/cc)	Tissue ($\rho=1.03$ g/cc)
H	0.33	0.06	0.11
C	0.67	0.54	0.26
N		0.22	0.03
O		0.03	0.60
F		0.17	
Ca		0.18	
Na			0.001
P			0.002
S			0.003
Cl			0.002
K			0.002

Table 5.1: Elemental composition of Simulated Targets

5.2.2.1 MCNP Simulation Analysis

In these studies single pencil proton beams are used ranging in energies from 50 MeV to 250 MeV in 50 MeV increments, for the same target dimensions, $50 \text{ cm} \times 10 \text{ cm} \times 10 \text{ cm}$, with the beam traveling along the central x-axis as shown in the schematic of Figure 5.3. CZT was not employed in this simulation as the focus was the originating and scattering locations of the photons, neutrons, and protons within the target. Here we discuss a 3-D, 2-D, then 1-D (along the beam path) analysis of each target material.

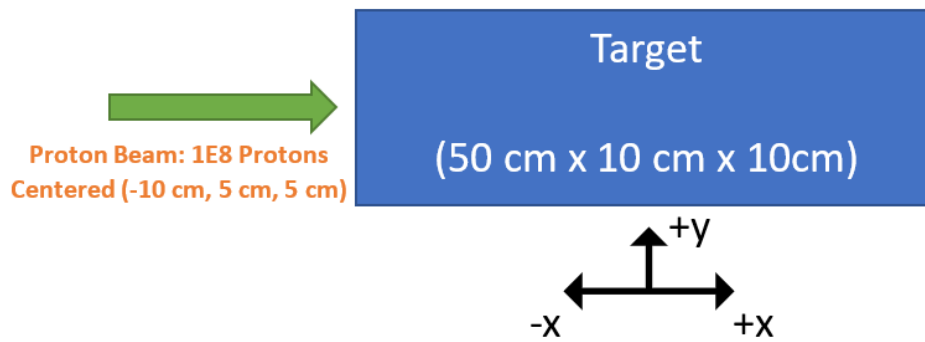


Figure 5.3: Schematic of MCNP6 simulations of various low Z targets and a 0.25 cm radius proton pencil beam incident from the central -x axis.

To obtain a 3-D emission profile of the particles of interest a volumetric mesh F4 tally was used encompassing the entire target, if the particle surpassed the energy threshold and crossed the voxel then it is tagged and tallied in that voxel. Figure 5.4 shows the 3-D distribution of the neutron, photon, and proton emission for 50 MeV proton beam for each target material, as planar slices in the z-direction.

A consistent trend is evident in the spatial distribution of the of particles for all studied materials. The gamma ray flux is very similar to that of the proton tracks within each target, staying concentrated along the beam path. However, the neutron emission shows a different profile.

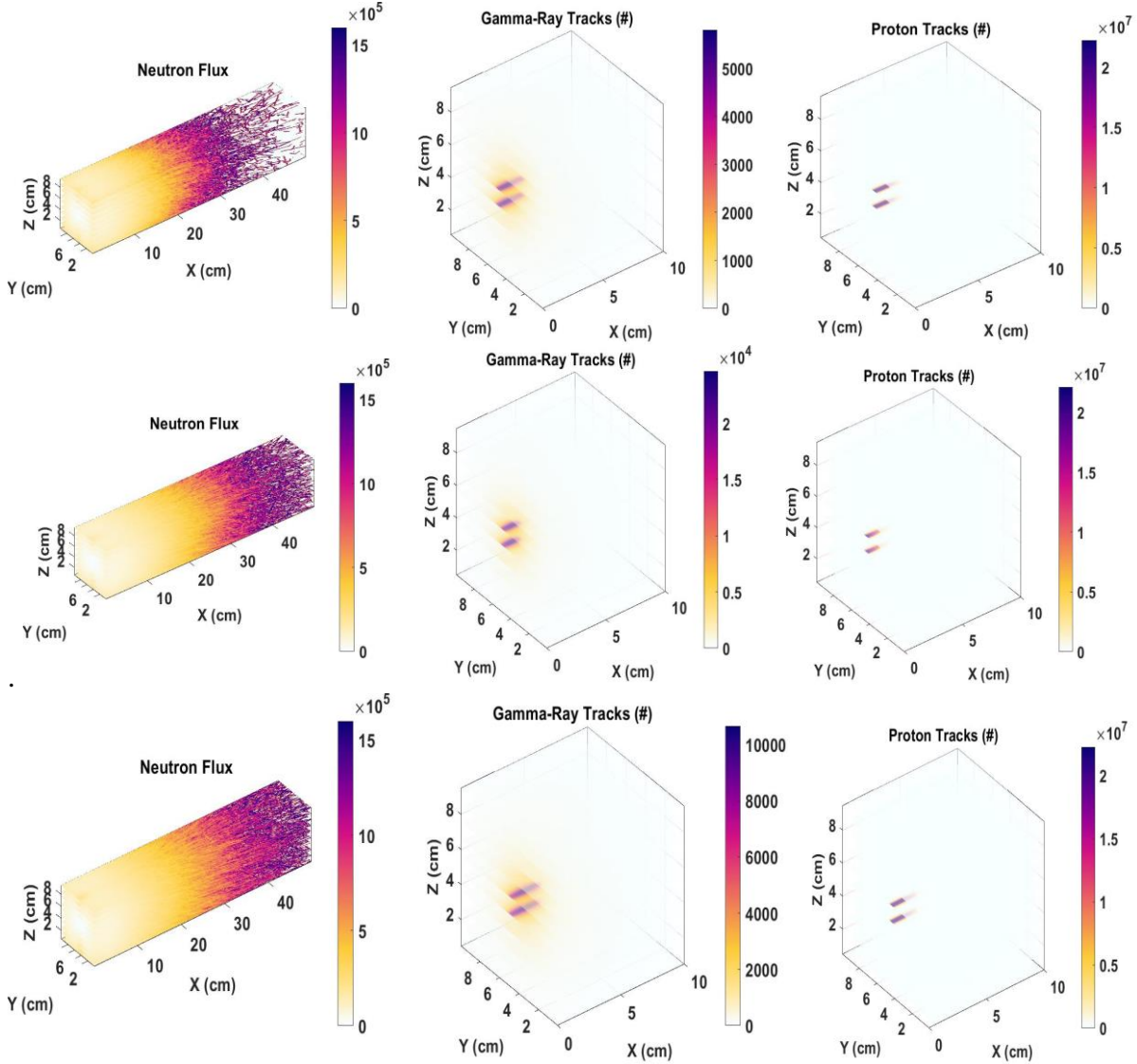


Figure 5.4: 3-D Distribution for HDPE (top row), BEP (middle row), and Tissue (bottom row) targets simulated in MCNP6. The intensity bar corresponds to the number of tracks tallied in each voxel. The 3-D target is truncated for the gamma and proton tracks in the X direction to 10 cm.

As stated in chapter 3, neutrons are capable of inducing many of the same nuclear reactions seen from proton interactions, with a very different cross-section, which implies that there is the possibility that the photopeaks we focus on for imaging could have events associated with neutron interactions. The 3-D neutron profile shows that majority of the neutrons travel far past the beam's end point, many escaping the target. The HDPE target indicates a cutoff point suggesting that some of the emitted neutrons come to rest near 40 cm into the target, which could be due to the high

concentration of hydrogen slowing down the neutrons. This is confirmed by the dose profiles shown in Figure 5.5 from the neutron presence in each target material which is approximately three times higher in the HDPE than the other two materials. However, this means that the photons that are created from the neutron emission will only lead to noise in the image space, as they do not follow the trajectory of the of the proton beam.

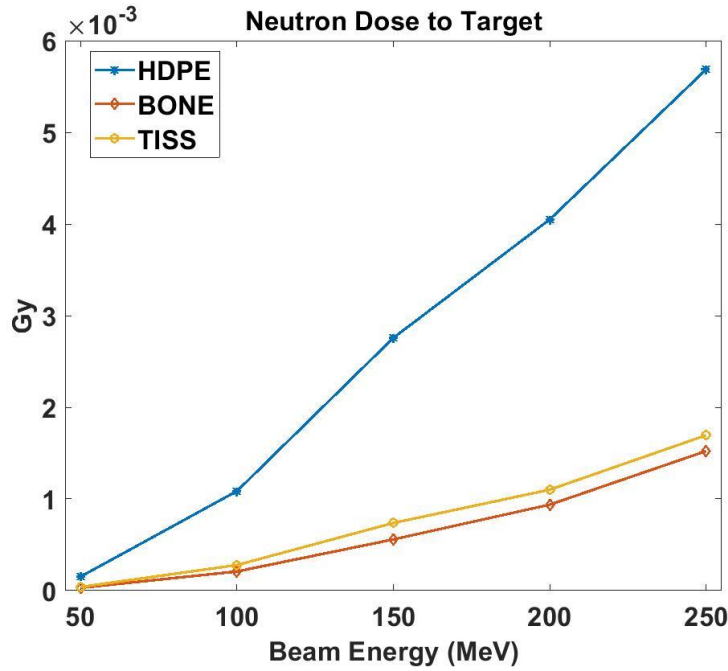


Figure 5.5: Neutron dose calculated by MCNP6 using a F6 tally, as a function of proton beam energy.

Examples of the 2-D profiles are shown in Figure 5.6, Figure 5.7, Figure 5.8 and to give a better representation of the lateral spread in the neutron, photon, and proton distribution profile, respectively for the 100 MeV, 150 MeV, and 200 MeV proton beam simulations.

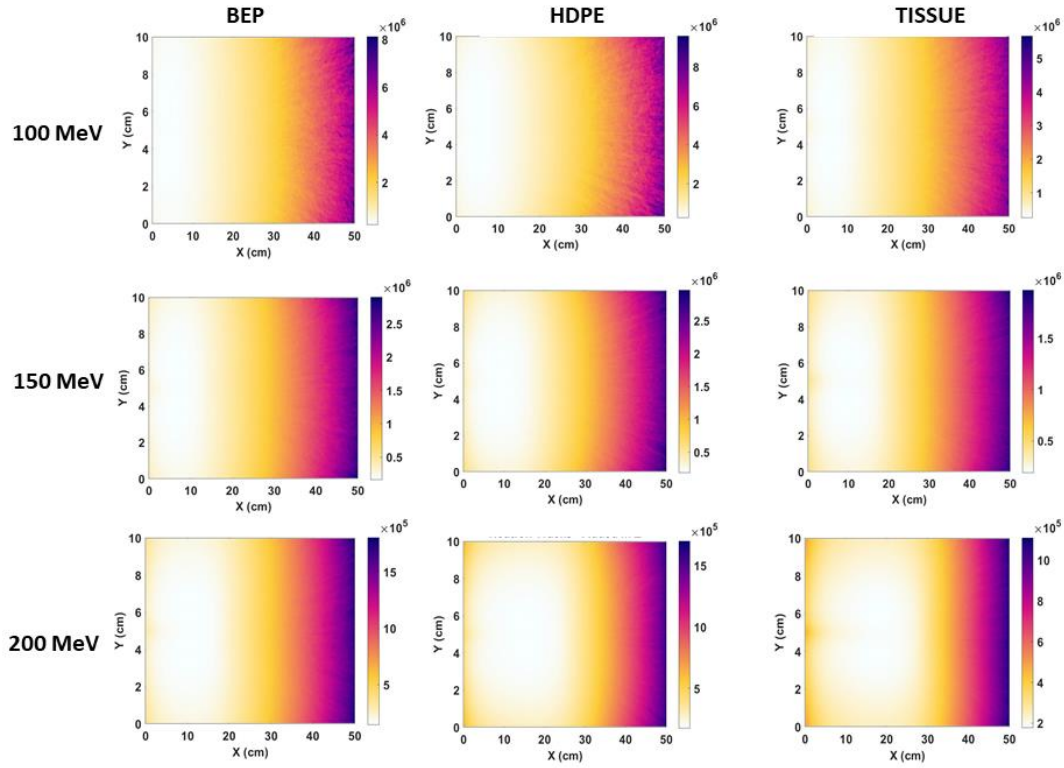


Figure 5.6: 2-D neutron mesh tally profile simulated in MCNP6

The neutron tracks show that they do not correlate to the proton's emission profile and are more prominent further from the beam's origin. When comparing the photon's lateral spread to that of the protons, we see that its much broader along the y-axis than the protons. This plumage in the photon's distribution could suggest that many are born far from the beam's central axis which could be in part due to the secondary neutrons causing further nuclear reactions or from protons that straggle from their trajectory, as shown in Figure 5.7. This straggle typically increases radially with proton beam energy about the central axis of the beam.

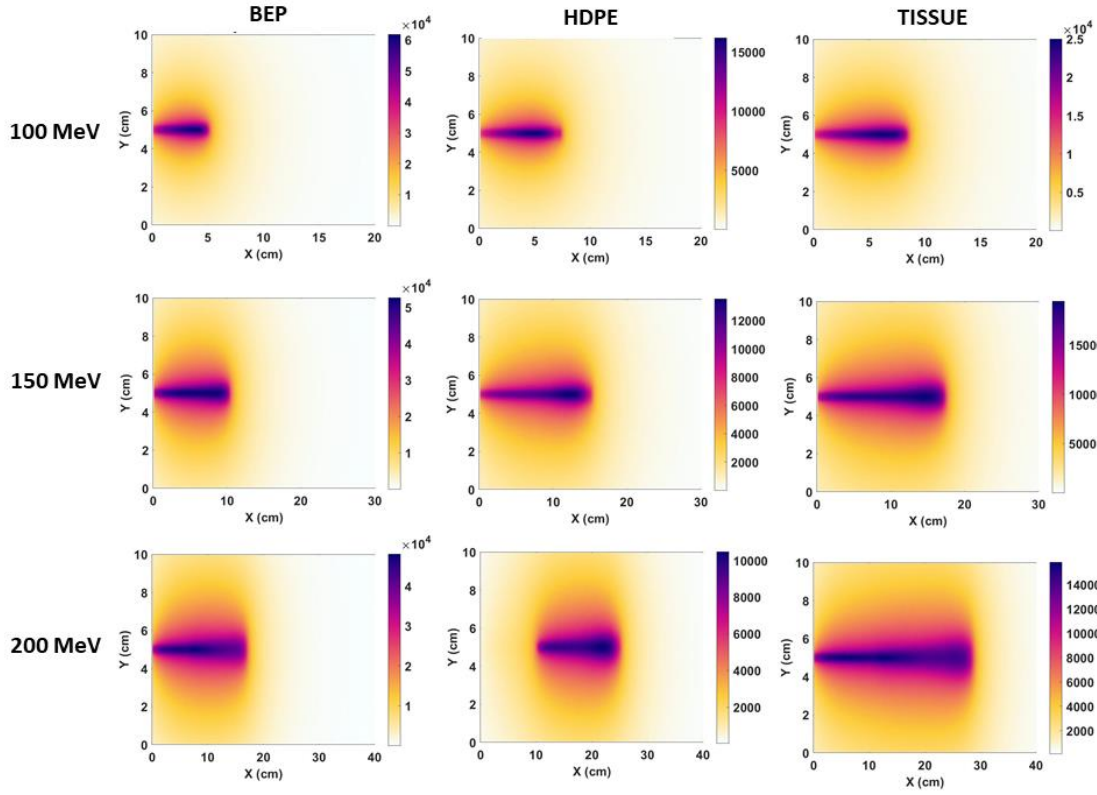


Figure 5.7: 2-D gamma mesh tally profile simulated in MCNP6

As the widening of the proton beam increases with energy so does the lateral spread of the gamma-ray distribution. With increase in proton energy the gamma-ray distribution shifts further from the incident edge of the target and does not become prominent until a further depth into the material, as seen in the 200 MeV distribution for the HDPE target in Figure 5.8. This could be due to the low cross-section of proton-nuclei reactions at very high energies for ^{12}C . Thus the proton will mostly travel a straight path scattering off electrons, until it loses enough energy to slow down and cause gamma emitting reactions.

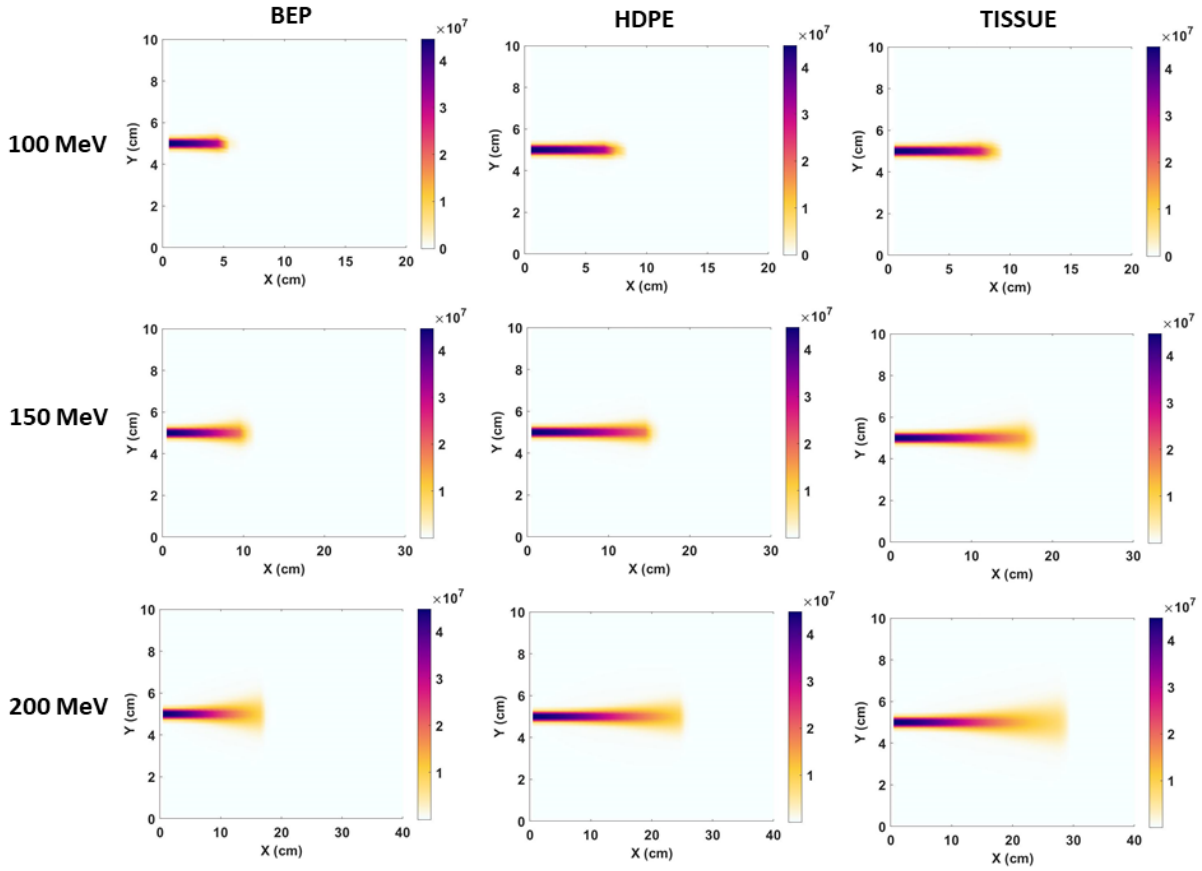


Figure 5.8: 2-D proton mesh tally profile simulated in MCNP6

The straggling of the proton beam distribution is most prominent near the end of its track at high energies. At 100 MeV the beam stays nearly consistent and concentrated about its central axis across all materials. As the incident energy increases so does the chance of scatter thus causing deflection from the intended path of the proton.

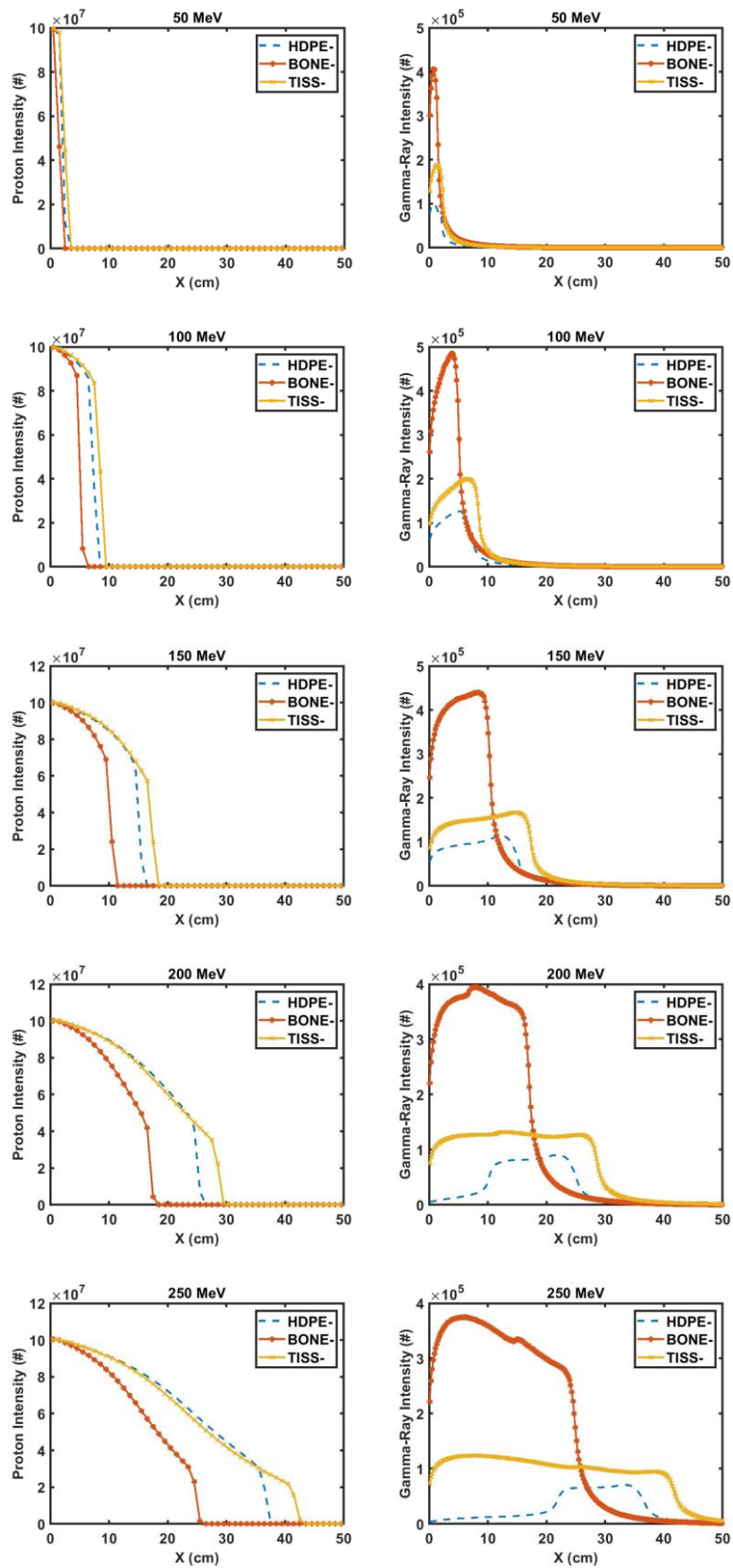


Figure 5.9:1-D profiles along the central beam axis of the photon and proton intensity.

Lastly, 1-D profiles are compared for the proton and gamma distribution to ensure that there is correlation between the proton trajectory and the emission of the photons. Figure 5.9 compares the intensity of all three particles along the central axis of the proton beam. At the point at which the protons come to rest within the target we can see that the gamma ray tracks follow suit. There are also stark differences in the gamma ray distribution profile across the three materials as a function of energy. As the energy of the proton beam increases, in the HDPE target, the most intense location of gamma-ray profile begins to shift closer to the end of the proton beam, suggesting that very little nuclear reactions happen near the beginning of the proton track. This is plausible as at the higher energies the protons may be less susceptible to proton-nuclei interactions or scattering until it slows down enough to cause an energy transfer to the atoms of interest.

The MCNP study shows that the expected noise in the spatial distribution of the gamma-rays produced during a proton beam irradiation should be expected more so laterally than longitudinally along the beam's path. This associative noise with the PG emission could be in part due to the neutron emission that can go to produce more gamma rays or the straggle of the incident protons. It is also worth mentioning that in practice, the tertiary emission of gamma rays from the neutrons could happen much later after the therapeutic beam shuts off causing residual noise in time.

5.2.2.2 *Geant4 Simulation Analysis*

Geant4 simulations using the *Polaris3 – Prompt Gamma Compton Camera Simulation (PGCCS)* can provide the originating location of each detected gamma ray produced from all protons, neutrons, and other secondary particle induced reactions. For each simulation the proton beam energy was increased by 50 MeV from 50 MeV to 250 MeV and the originating location distribution and reaction types that caused the gamma-ray emissions were analyzed.

For each simulation, a beam intensity of $5E8$ protons was used to irradiate a 50 cm x 20 cm x 20 cm target along the x-direction. The proton beam radial width was 0.125 mm and the Gaussian spread in the beam energy was 4 keV. The gamma rays tracked are the ones that cross the CZT detector system that is 10 cm below the target parallel to the beam, shown in Figure 5.10.

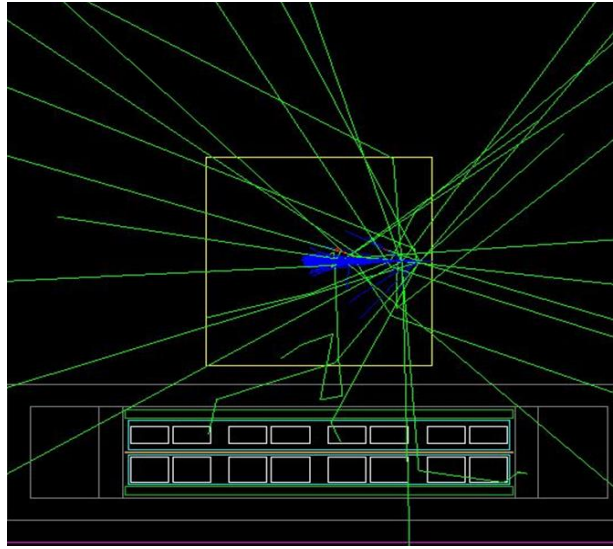


Figure 5.10: Schematic of the HDPE using *PGCCS*.

To understand the noise in the photon emission the data was separated by the particle that induced the reaction: proton induced, neutron induced, and ion induced. Figure 5.11 shows an example of this for the HDPE target and the 250 MeV proton beam irradiation. The neutron induced reactions resulted in less than 20% of all photon emissions for all beam energies and targets and were more so prevalent in the bone equivalent plastic simulations.

Although, the number of neutron-induced photons is low in comparison to the number induced by protons, the deviation of the neutrons from the beam trajectory can lead to a more spread-out PG emission. When imaging PG lines that are induced by both neutrons and protons there can be additional noise in the image space correlated to the neutron induced interactions. Across all simulations the effects of heavy ion-induced gamma-rays were minimal.

The proton induced profile shows that most of the detected photons collected by the Polaris J3 detector originate below the first 100 mm of the proton beam, this could be due to the centering of the detector below the target, or that as the protons continue to travel, the photons near the end of the track tend to leave the source in directions away from the detector.

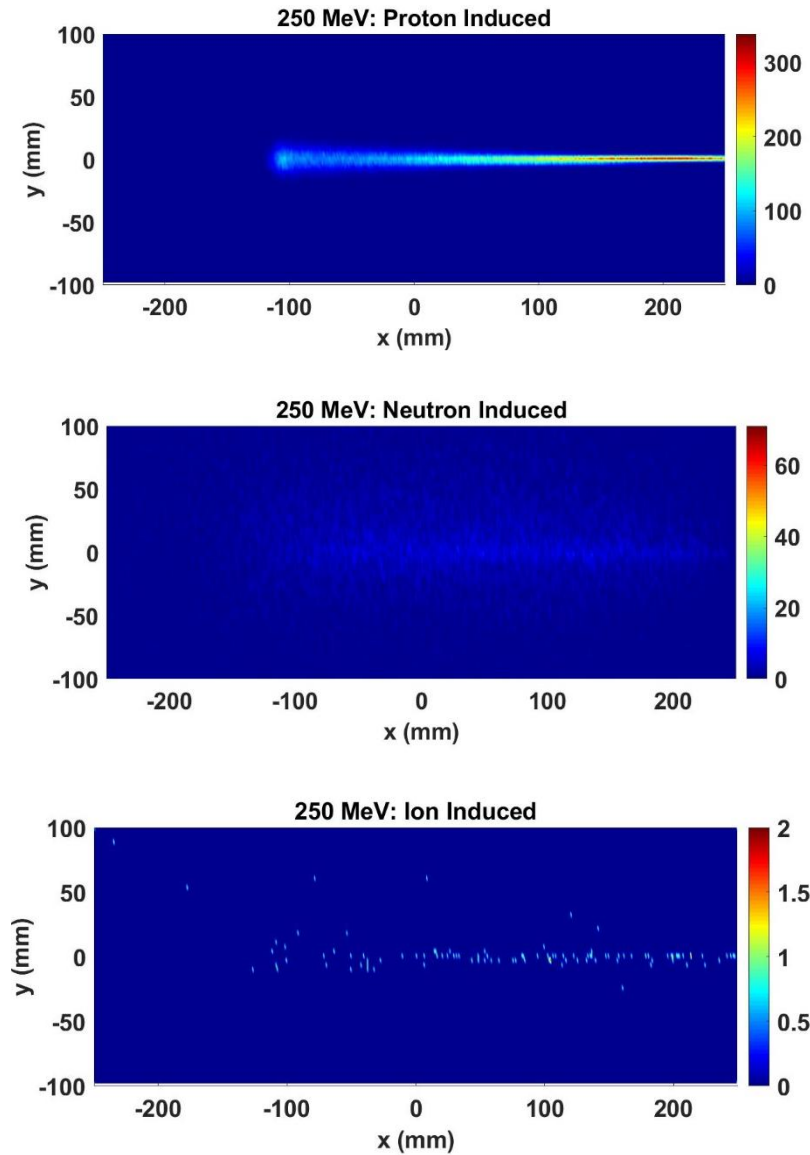


Figure 5.11: 2-D distribution of gamma rays emitted from nuclear reactions induced by protons, neutrons, and ions within the HDPE target. The intensity bar corresponds to the number of photons emitted in the voxel (0.5 cm³)

To focus on the PG's that will be used for image reconstruction, a 1-D profile, shown in Figure 5.12, illustrates the 718keV, 4.44 MeV, and the 511 keV annihilation photons distribution as a function of energy to assess their usefulness in determining the proton beam's range and endpoint. The 511 keV emission is included as we can see these photons directly from proton interactions and from pair production events produced by the PGs. All three materials consistently demonstrated that the 4.44 MeV peaks are well within the Bragg peak region, the 718 keV distribution tends to plateau as a flattened curve as the proton energy increases, and the 511 keV emission could also serve as a good estimator of the beam's length.

However in practice, the 511 keV emissions are not only prompt but can also be delayed on the order of minutes, which leads to noisy and less-informative reconstructions than what is seen in Figure 5.12 for the HDPE distribution.

Figure 5.13 and Figure 5.14 illustrate the 1-D profiles for both the BEP and tissue targets, which show similar profiles with slightly distinct features. The 718 keV emission profile shows that in the higher density material, BEP, we see sharp peaks slightly shorter in depth in comparison to the 4.44 MeV and 511 keV profiles, suggesting that in imaging there should be a brighter hotspot near the end of the track. Versus, the lighter materials which have a broader and more flattened curve which suggests the expectation of a more uniform distribution in future image reconstructions of this energy line.

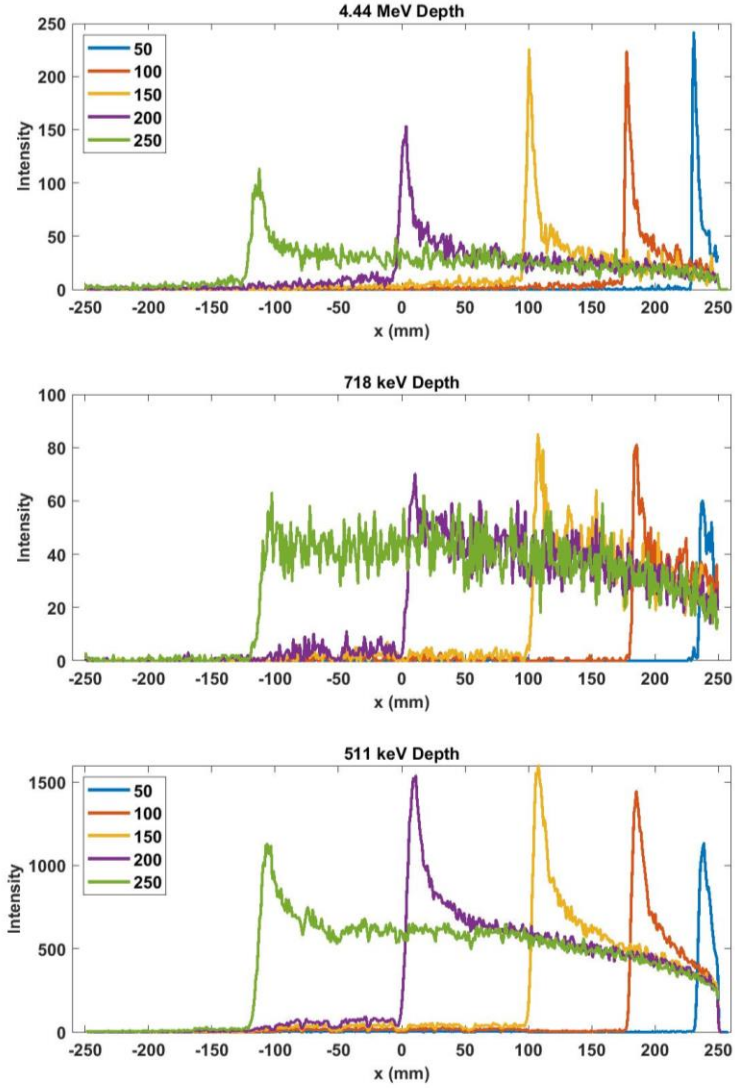


Figure 5.12: 1-D distribution of the 4.44 MeV, 718 keV, and 511 keV depth profile along the proton central axis as a function of proton beam energy in the HDPE target simulated in *PGCCS*.

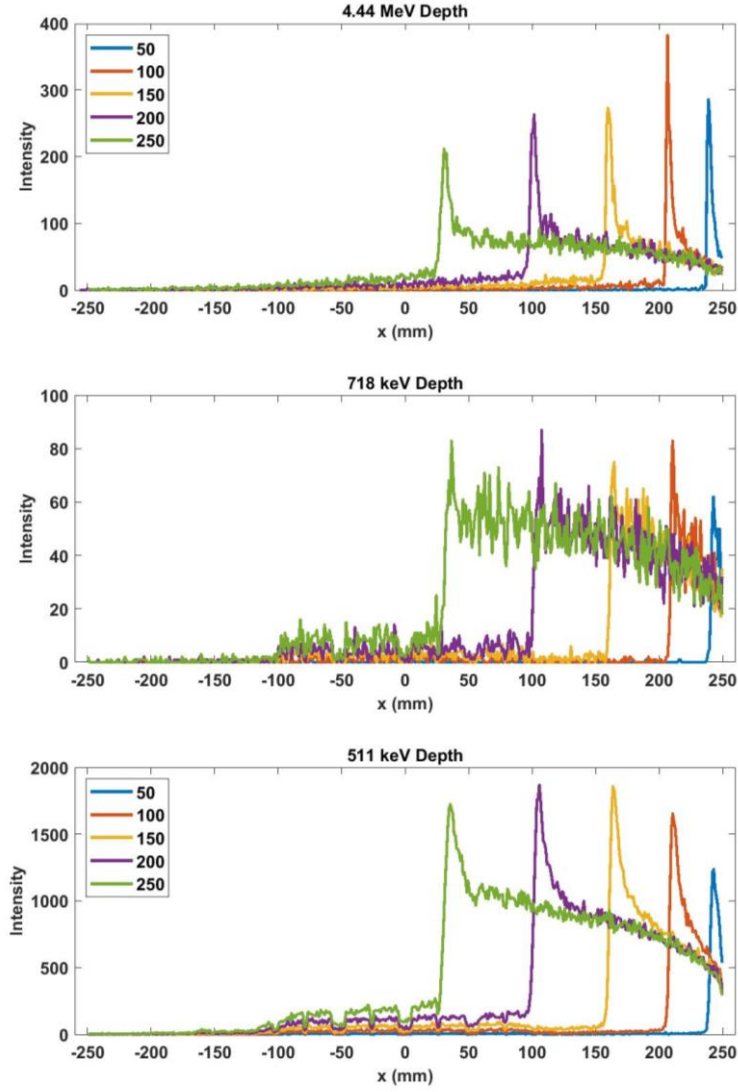


Figure 5.13: 1-D distribution of the 4.44 MeV, 718 keV, and 511 keV depth profile along the proton central axis as a function of proton beam energy in the BEP target simulated in *PGCCS*.

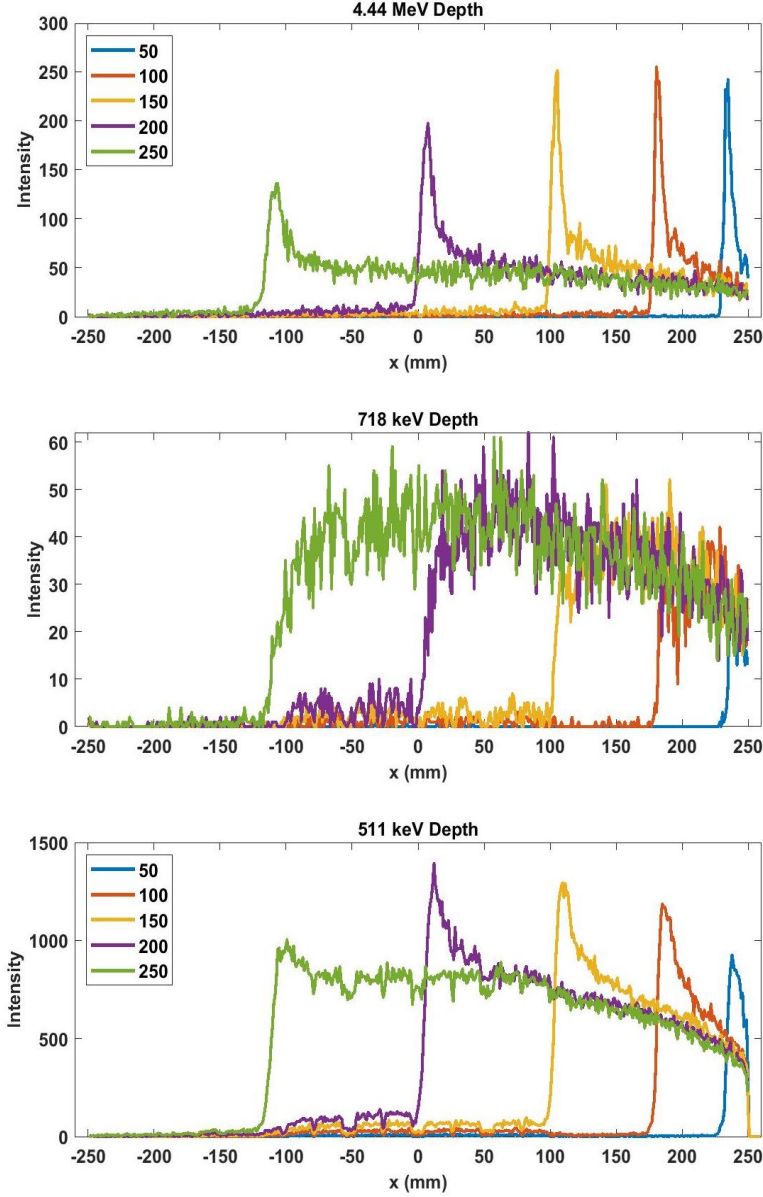


Figure 5.14: 1-D distribution of the 4.44 MeV, 718 keV, and 511 keV depth profile along the proton central axis as a function of proton beam energy in the tissue target simulated in *PGCCS*.

Across all three materials the 4.44 MeV profile is much more prominent near the end of the beam path than the rest its profile giving promise to being able to reconstruct a clear hotspot near the Bragg Peak location. Using this energy line for MLEM reconstructions suggest that the latter region of the profile could be lost with each iteration as the focus of the reconstruction would

be the maximum likelihood location of the 4.44 MeV's origin which points to the end of its profile from these simulations.

5.2.3 Spectral Analysis

A spectral analysis of the prompt gamma emission from homogenous targets is studied to validate the effectiveness of detecting these photons.

5.2.3.1 MCNP Analysis

MCNP simulations were used to obtain a spectrum of the emission of the photons from three different target materials. A F2 tally provided the surface fluence of the gamma-ray emission from each surface of the target as function of energy as shown in Figure 5.15, Figure 5.16, and Figure 5.17 for the HDPE, BEP, and tissue targets, respectively.

These spectra show the gamma-ray emission from each target material as a function of proton beam energy. As the composition of the target material becomes more complex (list of elements for each target is shown in Table 5.1) so does the energy spectra which shows an increase in gamma-ray lines associated with the de-excitation of the various elements in the targets. There are also photopeaks that show only after a certain proton beam energy which can be leveraged in future work when determining the beam's endpoint and Bragg peak based on the energy threshold required to create certain prompt-gamma ray lines. These spectra show that the change in material can be easily identified by unique lines in the spectra, many of which fall within CZT's dynamic range of 3 MeV.

Under many of the photopeaks, for example the 4.44 MeV emission from carbon, there is a broaden hump which signifies the down scatter of these events prior to leaving the target. This could also be a function of the incomplete physics model for secondary particle tracks at such high

energies in MCNP simulation packages. For example, the 718 keV peak from carbon is not present in the energy spectra shown nor is it found in the proton cross-section tables for MCNP.

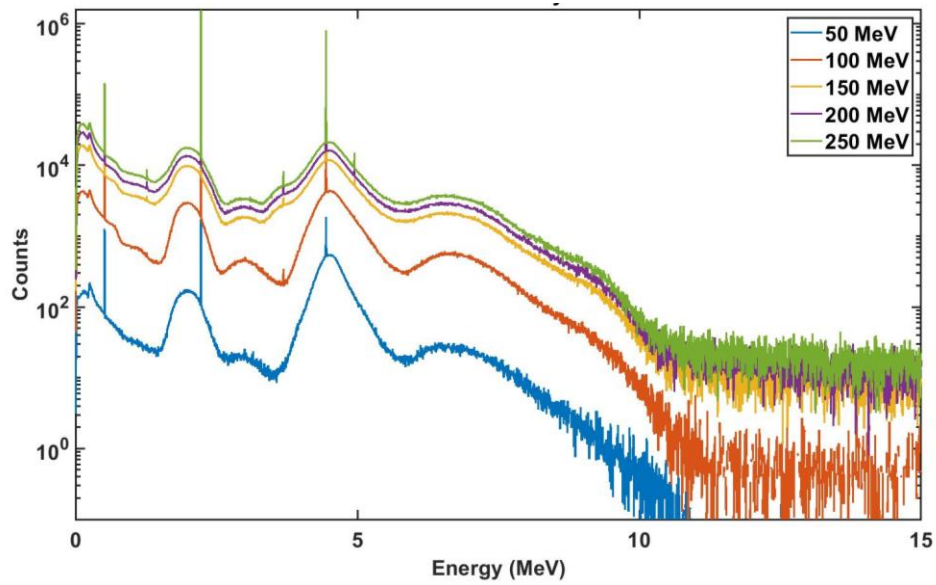


Figure 5.15: MCNP6 gamma-ray energy spectra from proton beam irradiation of the HDPE target.

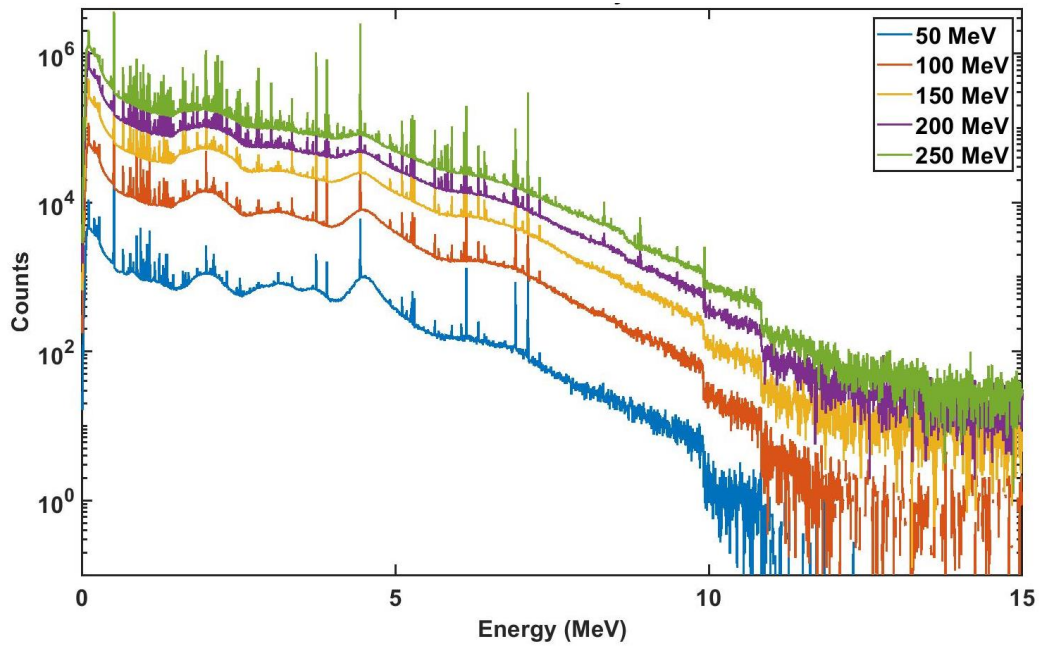


Figure 5.16: MCNP6 gamma-ray energy spectra from proton beam irradiation of the BEP target.

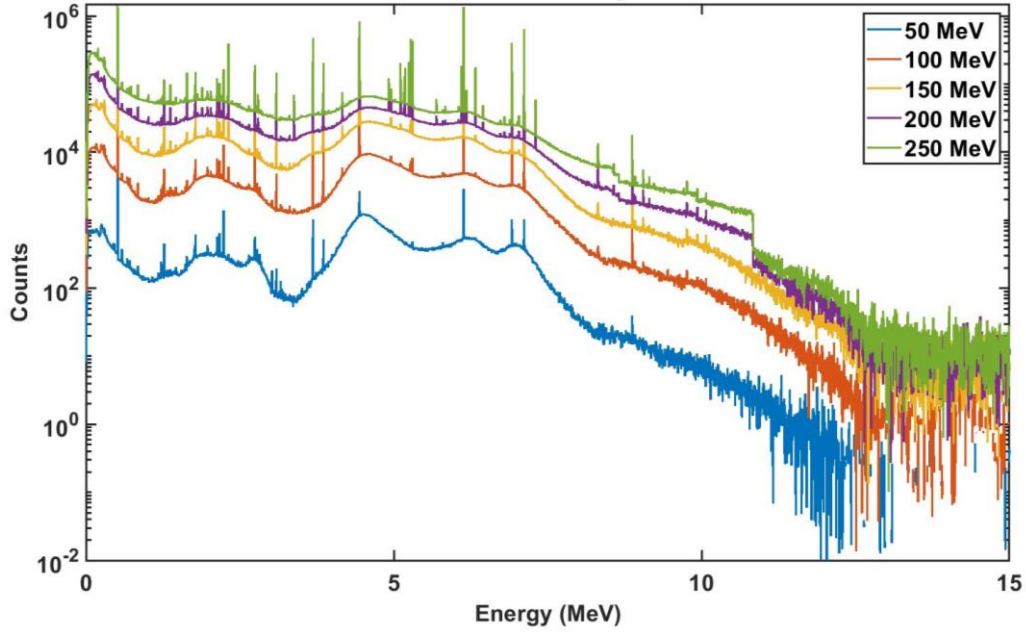


Figure 5.17: MCNP6 gamma-ray energy spectra from proton beam irradiation of the tissue target.

5.2.3.2 Geant4 Analysis

A HDPE target was simulated for the spectral analysis using the *PGCCS*. In this simulation the beam utilized $5e9$ protons, and the energy is incremented by 5 MeV from 20 MeV to 100 MeV and is shot parallel to the Polaris J3 detection geometry similar to the schematic shown in Figure 5.10

Figure 5.18 shows the energy spectra for each simulation and a zoomed in view of the 718 keV and the 4.44 MeV photopeaks as these are the proton-carbon interactions of interest for beam range verification. The energy spectra show a consistent increase in the overall number of events as the incident proton energy increases as expected, with a higher energy the higher the probability of scattering events before ionization at the end of the proton's track.

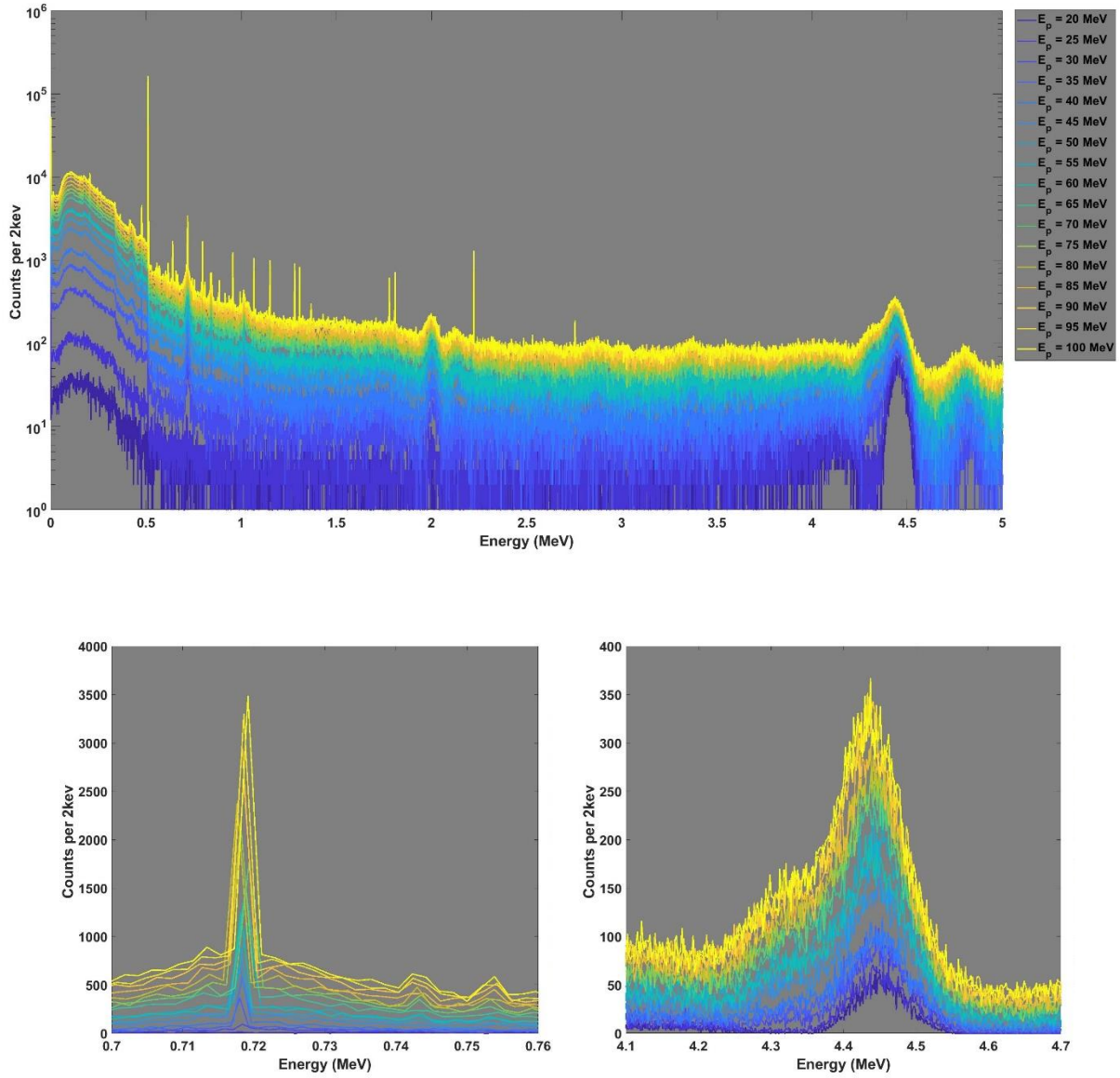


Figure 5.18: Polaris J3 recorded energy spectra of the HDPE Simulation up to 5 MeV. Bottom figures show the 718 keV (left) and the 4.44 MeV (right) photopeaks.

The origin data was used to analyze the geometrical distribution of the 718 keV and the 4.44 MeV emissions within the HDPE target. Their 1D profile was compared to SRIM simulations of the expected stopping power or Bragg curve associated with the incident beam energy and

composition and density of the target. Figure 5.19 shows the 3D distribution of the 718 keV and 4.44 MeV emissions for the 20 MeV, 70 MeV, and 100 MeV proton beams.

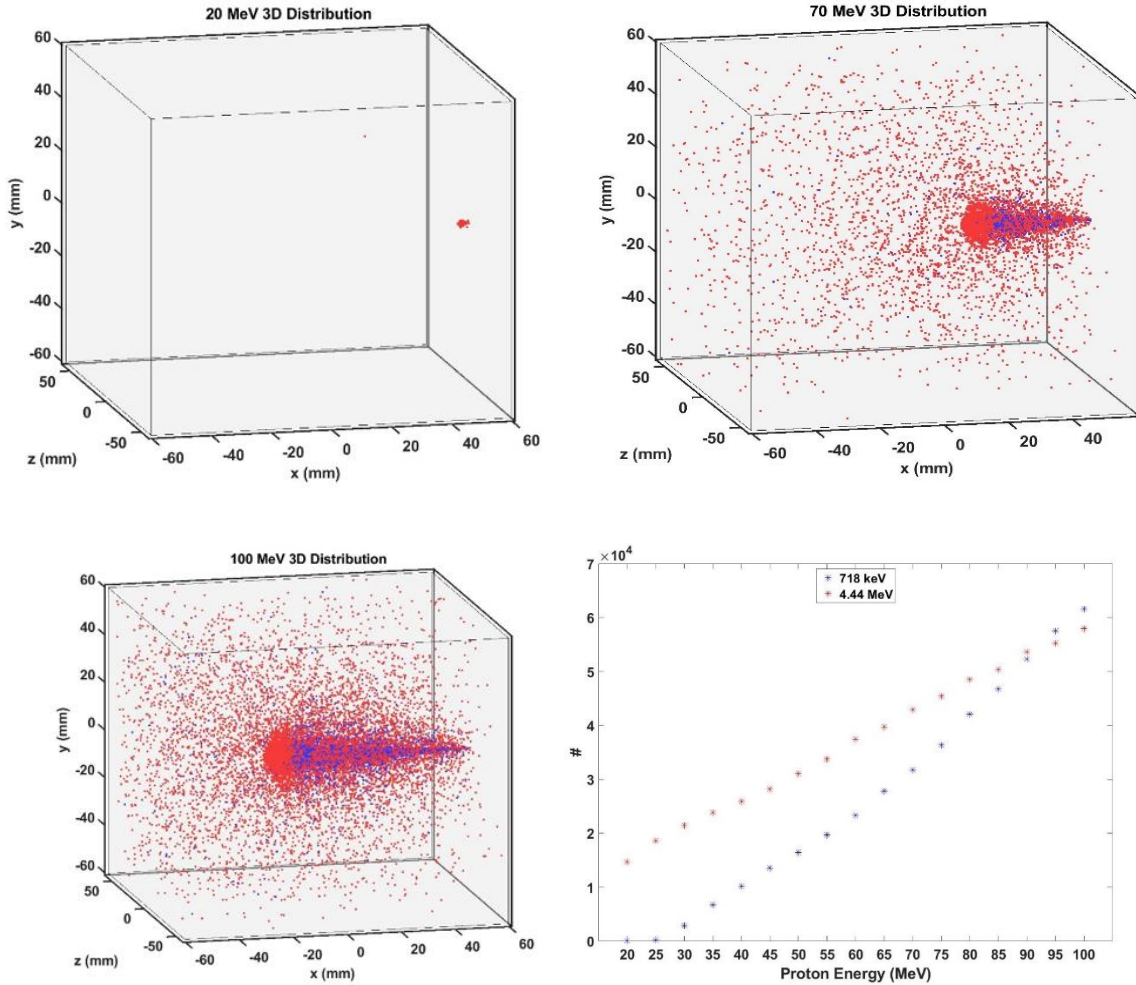


Figure 5.19: 3-D distributions of the originating locations of the 4.44 MeV (**red**) and the 718 keV (**blue**) photons within the HDPE target that were detected by the Polaris J3 system. The bottom right figure shows the number of emitted 718 keV and 4.44 MeV photons for each proton beam energy.

Figure 5.19 shows that while the 4.44 MeV emission is the most prominent for most beam energies it also results in a more widespread area of scatter than that of the 718 keV. For example in the 100 MeV proton beam simulation the 718 keV results in more emissions detected by H3D-J however, within the target, the 3-D distribution shows that most of the 718 keV's are found to

be more centralized around the beam versus the 4.44 MeV which shows more events throughout the entire target, with the largest concentration near the end of the beam path. This could be due to their different proton energy thresholds, the 718 keV has a threshold of 22 MeV which means that the proton must deposit at least that much energy to induce this photon, so theoretically, the proton should not be too far from its normal trajectory before depositing this much energy within a reasonable incident energy window. On the other hand, the 4.44 MeV can be seen from a proton energy of at least 5.1 MeV which means a 100 MeV proton could scatter quite a bit away from its path before creating this photon.

Figure 5.20 shows the normalized intensity depth profile of both the 718 keV and 4.44 MeV lines for the 70 and 100 MeV proton beams in comparison to the Bragg curve calculated by SRIM2008 along with the peak difference between the 1D profile and the Bragg curve for all simulations.

The depth profiles are normalized for the number of events at every 0.2 mm step for both emissions divided by the sum of all 718 keV and 4.44 MeV events at that step. There are no 718 keV emissions for the 20 MeV beam simulation as this beam energy is below the 718 keV energy threshold. The peak difference plot in Figure 5.20 reveals that the average distance between the 4.44 MeV peak and the Bragg peak is $1.80 \text{ mm} \pm 0.56 \text{ mm}$ and $8.94 \text{ mm} \pm 1.06 \text{ mm}$ for the 718 keV peak location.

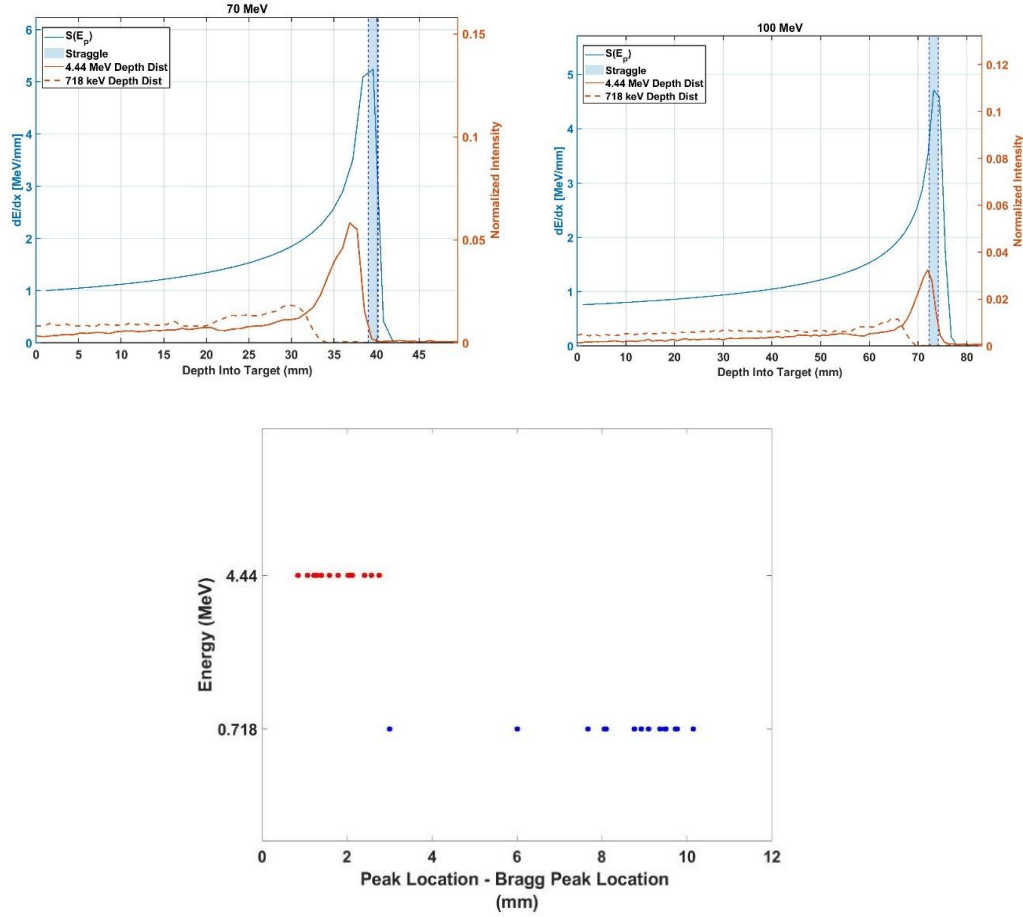


Figure 5.20: 1-D Profile of the 718 keV and 4.44 MeV photon emission within the simulated HDPE target with respect to the Bragg curve for each beam energy within a C_2H_4 target calculate by SRIM. The bottom left figure shows the peak difference between the 718 keV and the 4.44 MeV profiles with respect to the Bragg peak, respectively.

The difference in the depth at which we see the Bragg peak and the peak of the two photon energy lines does not vary much with proton beam energy, spanning roughly 2 mm for each photon.

5.2.4 Analysis Summary

The theoretical analysis show that the photon emission from proton interactions within various targets closely follow that of the proton's trajectory. There is an obvious spread or noise

associated with the PG emission that could be in part due to both the neutron emission from proton interactions and the straggle of the proton beam itself.

Of the three targets simulated, HDPE, BEP, and tissue, the results show that there are many photopeaks for each that can be used for imaging analysis and differentiation between materials for future work with heterogeneous targets.

When focusing on the HDPE target, specifically studying the 4.44 MeV and 718 keV emissions, the PG profiles closely follow that of their theoretical yield. The 4.44 MeV profile ends closer to the Bragg peak location than the 718 keV emission as its threshold energy is as low as 5.1 MeV whereas the 718 keV emission will need 22 MeV for its nuclear reaction. This information can be leveraged in imaging as the 4.44 MeV profile shows a sharp rise near the end of its track suggesting that in images, the full profile of the beam will be lost to the iterative algorithm of MLEM which will inherently converge to the 4.44 MeV peak. Whereas the 718 keV profile shows a more flattened and evenly distributed profile suggesting that although it may not end at the Bragg peak, its profile could lend information about the full length of the beam provided we estimate the difference between the threshold location of the 718 keV emission and the Bragg peak location.

5.3 Verification Method I: 718 keV Imaging

The 718 keV photon emitted from carbon-proton spallation can be an advantageous PG for PBRV in imaging as its energy is within the dynamic range of CZT, close to that of 662 keV where CZT boasts a 0.3% energy resolution. At this energy, event reconstruction should be robust enough to allow for well reconstructed Compton cones for imaging, despite the background noise associated with PG detection. Simulations show that for the most part the 718 keV emission is nearly even along the entire beam profile for various materials. This type of emission profile could

serve well in determining the full extent and dose profile of the latter portion of the proton beam before it's Bragg peak.

In Chapter 3 we derived the threshold energy as the result of a simple two-body breakup reaction and described it as the following,

$$E_{th} = -Q \frac{(m_p + M_A + m_B + M_B)}{2M_A}. \quad (5.10)$$

Where Q is the Q -value of the reaction or the decay energy of the reaction, which is multiplied by a function of the mass of our target material (M_R) and reaction product (M_B), and the atomic mass of our projectile (m_p) and the rest mass of our reactants (m_A) and products (m_B).

For the analysis of the 718 keV emission from $^{12}\text{C}(p, x)^{10}\text{B}^*$, we will depend on the threshold energy of this reaction to provide a means of estimating the proton's depth of rest. Treating this reaction as a simple two-body problem implies that it will always have the minimum or negative Q -value, and therefore occur at the minimum threshold energy.

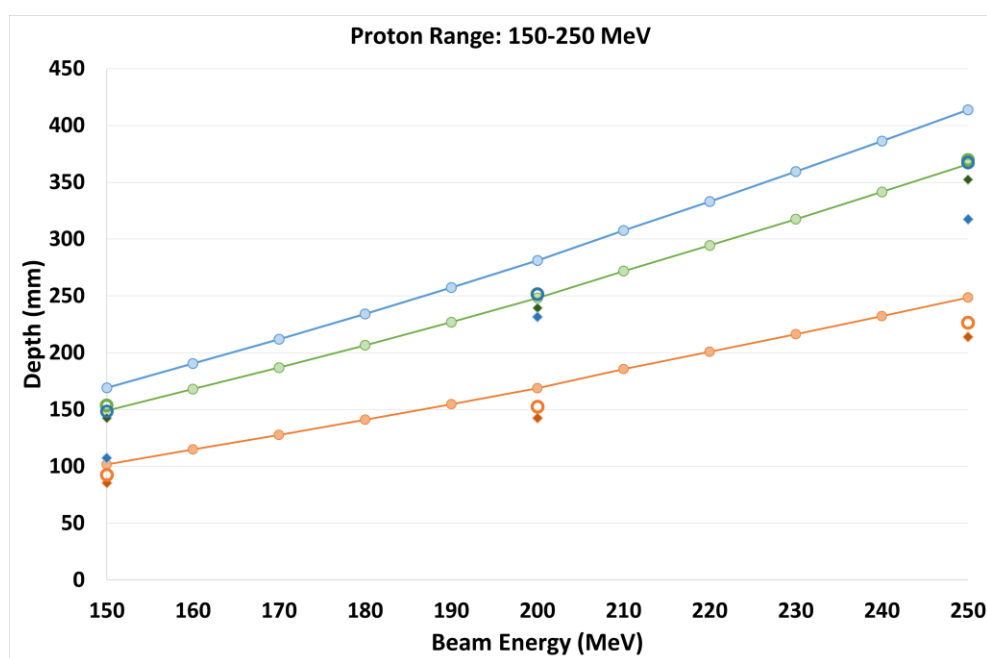
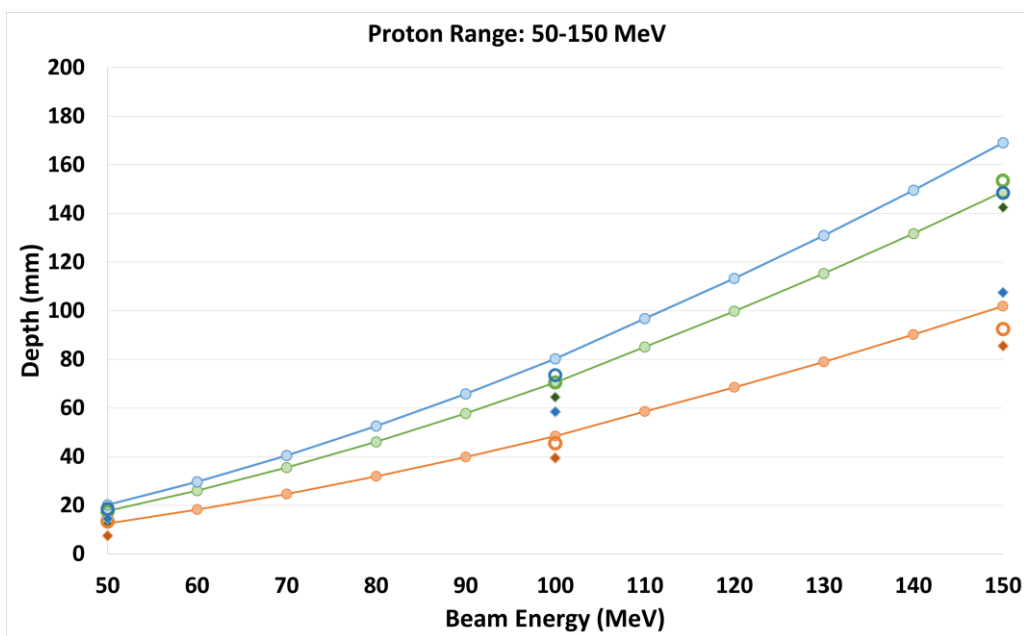
At sufficiently high energies, spallation will take place and all fragments lighter than the target nucleus can be produced. The $p^+ + ^{12}\text{C} \rightarrow ^{10}\text{B}^* + ^3\text{He}$ reaction emits the 718 keV gamma from the first excited state of ^{10}B . The electron capture decay of ^{10}C can also produce the 718 keV line, which decays in 19.255 s to the 718 keV level of ^{10}B 98.53% of the time (the other 2% is given to the 1.022 MeV line). The excited ^{10}B will then promptly emit the PG in 718.35 keV energy. In practice, when the proton beam comes to rest, the prompt gammas from ^{10}B will stop immediately, while the decay from ^{10}C will decrease with a half-life of 19.255s. Thus for our simplified problem, the 718 keV emission will have a $Q = -(19692.852 + 718.35) \text{ keV}$ and $E_{th} = 22124.980 \text{ keV}$ from the $^{12}\text{C} \rightarrow ^{10}\text{B}^*$. Whereas any ^{10}C produced from ^{12}C during the irradiation of the target will have a threshold of 25320.84keV. Since the focus is the imaging of the PGs we will focus on the 22.1 MeV threshold produced directly from $^{10}\text{B}^*$. Although, we must keep in

mind that the latter can cause residual or late photons in practice, which could lead to potential noise, when imaging multiple beams of the same target.

5.3.1 Bragg Peak Fit for High Threshold Energy Prompt Gammas

Figure 5.21 shows the correlation of the peak and drop-off or stopping point of the 718 keV photons emitted from *PGCCS* simulated proton beams on HDPE, BEP, and tissue targets. These profiles are compared to the estimated depth at which the proton will reach 22 MeV on average. We derive this depth from SRIM2010 simulations which provide the proton energy loss as a function of depth. As the proton beam energy increases so does the discrepancy between the 22 MeV depth calculated by SRIM and the peaking and stopping point of the 718 keV profiles.

The largest error is found in the tissue profile followed by the HDPE target which shows its largest deviation at the 250 MeV proton beam. However, all three targets show that the 718 keV emission closely follows its theoretical threshold, the largest discrepancy being in the peak values which could be due to the flattening of the 718 keV profile making the peak value difficult to decipher from the rest of its emission profile. Also, Kozlovsky shows the 718 keV cross-section peaks at around 28 MeV [65]. Therefore, if following the experimental cross-section, we should expect the peak to be further from the beam's end than the threshold depth of the 718 keV profile.



- | | | |
|----------------------|-------------------------------|-----------------------------|
| ● 22 MeV-HDPE SRIM | ◆ 718 keV Peak - HDPE PGCCS | ○ 718 keV Stop - HDPE PGCCS |
| ● 22 MeV - BONE SRIM | ◆ 718 keV Peak - BONE PGCCS | ○ 718 keV Stop - BONE PGCCS |
| ● 22 MeV-TISSUE SRIM | ◆ 718 keV Peak - TISSUE PGCCS | ○ 718 keV Stop-TISSUE PGCCS |

Figure 5.21: Comparison of the *PGCCS* 718 keV peak location to the *SRIM2008* calculate depth at which the proton beam reaches 22 MeV.

Focusing on the HDPE target alone and comparing the 718 keV profile peak and stopping point to the Bragg Peak for each simulated proton beam shows that there is an apparent relationship between the beam's Bragg peak location and the depth at which it reaches the threshold energy for the 718 keV emission, as shown in Figure 5.22.

This correlation indicates that the 718 keV peak and distal fall off or “stop” point follows the trendline of the Bragg Peak calculation as a function of proton beam energy very closely. This implies that if we can obtain an accurate estimate of the 718 keV emission end point and peak values that we can use either of these locations to estimate the proton Bragg peak's location by fitting those values to the exponential curve for this specific material. Along with finding the Bragg peak location, the 718 keV profile should also provide information about the full profile or length of the beam given the spatial analysis discussed in the previous section.

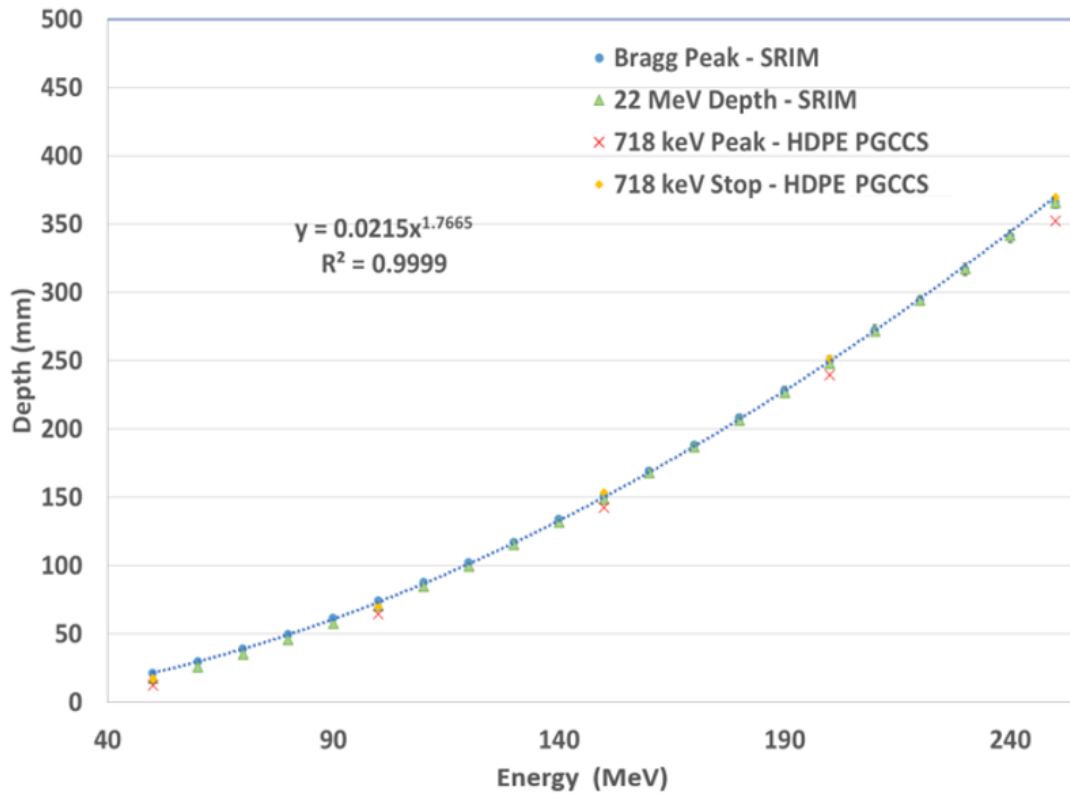


Figure 5.22: Comparison of the 718 keV peak and stop depths recorded from PGCCS to the SRIM2010 calculated Bragg peak locations for an HDPE target.

5.3.2 Experimental Analysis

Two S400x digital CZT systems and two M400 analog CZT systems were used for proton beam measurements at the Maryland Proton Therapy Center (MPTC) in Baltimore, Maryland. In this series of measurements, the detectors were placed at 96 cm and 30 cm from the isocenter of the high-density polyethylene (HDPE) target, $\rho = 0.97 \text{ g/cm}^3$. The further distance was used as a precautionary measure to ensure that the systems will not be oversaturated at high proton beam energies and dose rates. Figure 5.23 depicts the measurement setup used for both the digital and analog systems provided by H3D at the MPTC. For imaging analysis we will focus on the 30 cm separation distance measurements detailed in Table 5.2. The dimensions of the HDPE block used for these proton beam measurements are $38.1 \text{ cm} \times 25.4 \text{ cm}$ and 5.0 cm thick.

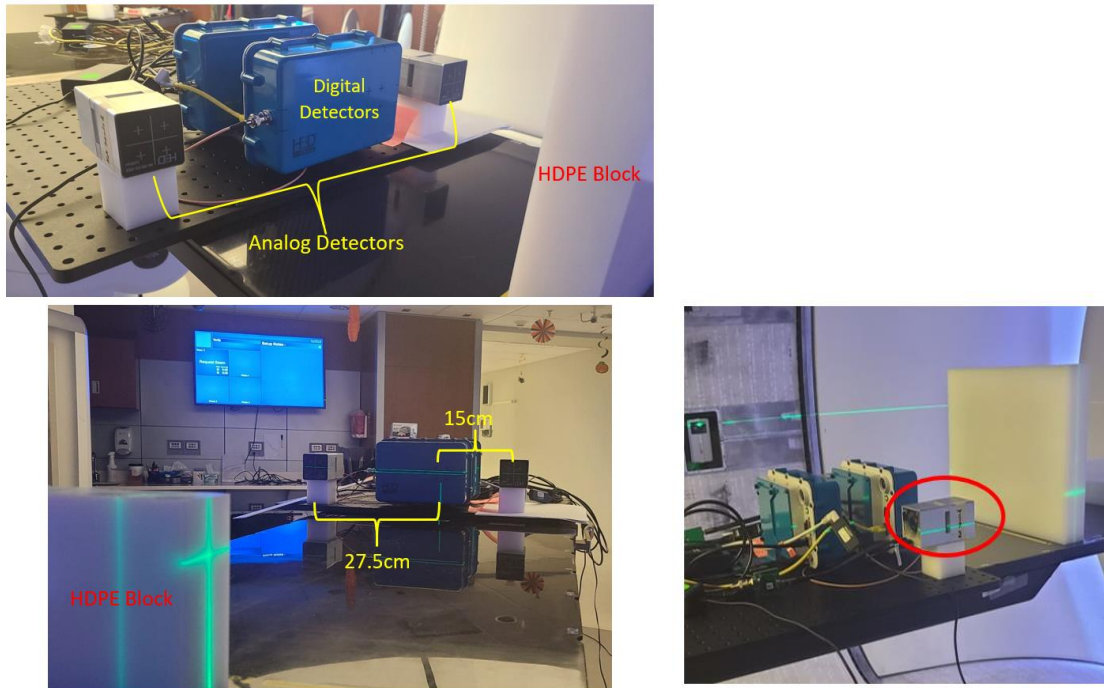


Figure 5.23: Proton beam measurement setup for the analog and digital systems. The top image shows the 30 cm separation setup, and the bottom figure shows the 96 cm separation measurement setup. (The green cross on the HDPE Block indicates the location of the proton beam entrance.)

Beam #	Energy	Dose Rate	Total Dose
AM 9	100 MeV	50 kMU/min	100 kMU
AM 10	100 MeV	50 kMU/min	100 kMU
AM 11	100 MeV	100 kMU/min	100 kMU
AM 12	100 MeV	150 kMU/min	100 kMU
AM 13	150 MeV	150 kMU/min	100 kMU
AM 14	200 MeV	150 kMU/min	100 kMU

Table 5.2: Summary of Beam Measurements at 30cm Separation Distance **kMU** = kilo-Monitor Units

The M400 system circled in red in Figure 5.23 is used for ROI-MLEM imaging of the listed proton beam measurements denoted as “AM” for Analog Measurement. All measurements were imaged using the 718 keV photopeak. ROI-MLEM was used to reconstruct images in a 40 cm \times 27 cm image space about the center of the target profile.

Figure 5.24 shows the ROI image reconstruction for AM 9-12, cropped to the size of the target (HDPE) profile of 38.1 cm \times 25.4 cm. These measurements only varied in dose rates as the proton beam energy remained constant at 100 MeV. Each image reconstruction shows a consistent overshoot of the expected beam range of 7.4 cm (calculated by SRIM2010). This could be due to the maintenance issues experienced with the gantry the day of the measurement or a misalignment of the target for these consecutive measurements. Although, the accuracy in estimating the beam’s true depth within the target is hindered by this unexplained overshoot, there is promise in the precision of the reconstruction across these measurements.

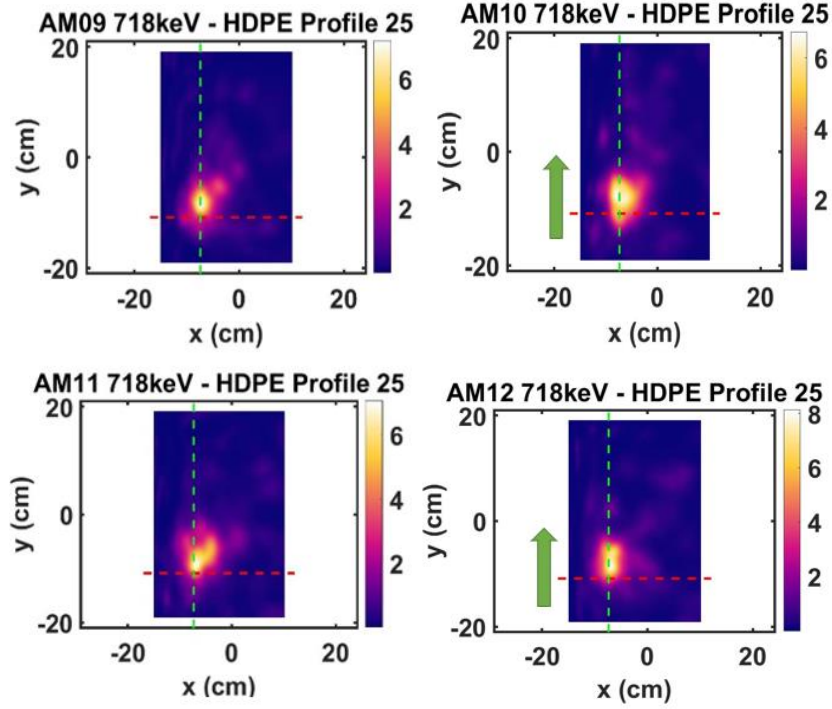


Figure 5.24: ROI-MLEM image reconstructions of the 718 keV photopeaks from measurements AM 9-12. The pixel resolution averages 0.025 cm^2 . The red line indicates the distal fall-off of the proton beam and the green line represents the trajectory of the beam, the green arrow indicates the direction.

Figure 5.25 provides a comparison of the peak location of the 718 keV image reconstruction shown in Figure 5.24. A 1-D profile is taken through the maximum intensity of the image reconstruction along the beam's trajectory and compared to the region at which we expect to see the beam enter and come to rest with in the target.

The uncertainty in the peak centroid of each image reconstruction shows to be less than 1 cm at a 30 cm image distance. Although all four measurements reconstruct past the expected beam location, we can verify that CZT and ROI-MLEM imaging can provide reproducibility in the PG emission depth estimate of multiple proton beams on the same target.

For these measurements, the FWHM for each 1-D profile was measured to estimate how well we can predict the full range of the proton beam. The calculated average FWHM is $6.89 \text{ cm} \pm 0.65 \text{ cm}$. According to SRIM and G4 simulations, for a 100 MeV proton beam, the expected

beam range is 7.4 cm and the expected threshold depth for the 718 keV emission is 6.99 cm. This shows that when using the FWHM, we can estimate the full range of the beam profile with 6.8 % error when directly correlating the FWHM to the beam range, and we are within 1.4% error when using the FWHM to estimate the 718 keV threshold depth.

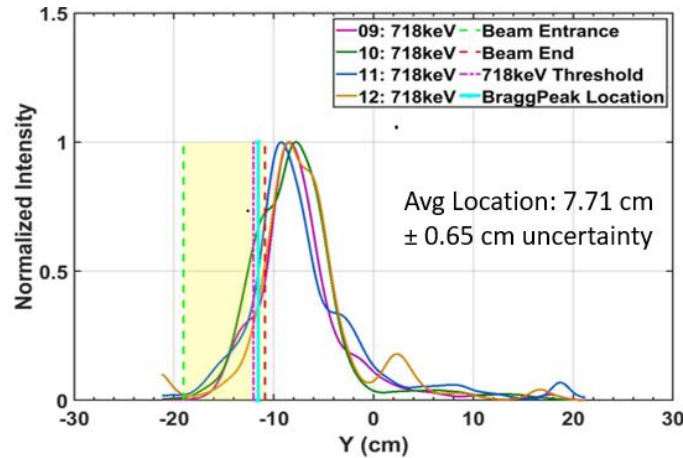


Figure 5.25: 1-D profile comparison of the 718 keV image reconstructions for measurements AM 09-12.

Measurements AM 13 and AM 14 were taken at the highest proton beam energies and dose rates allowed by the proton beam gantry. For these measurements, the M400 systems experienced its highest dead time rate at approximately 75% while the S400x systems were nearly completely saturated at 95%, (see Chapter 6 for further detail on detector performance). Figure 5.26 shows the image reconstruction of both AM 13 and 14 for the 718 keV photopeak.

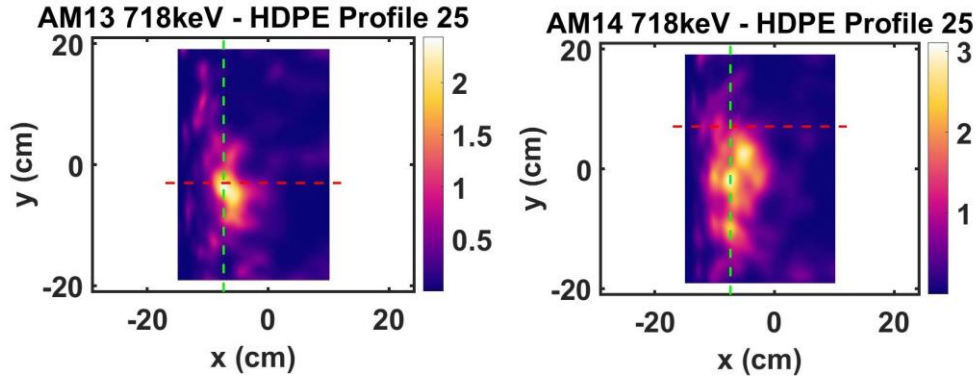


Figure 5.26: ROI-MLEM image reconstructions of the 718 keV photopeaks from measurements AM 13 and AM14. The pixel resolution averages 0.025 cm^2 . The red line indicates the distal fall-off of the proton beam and the green line represents the trajectory of the beam, the green arrow indicates the direction.

In the image reconstructions of the proton beam measurements with the highest proton beam energy and dose rates we see an apparent increase in the noise reconstructed in the image space. However, there is promise in these results as the majority of the intensity in the images reconstruct below the expected distal fall-off of the proton beam. As the length of the proton beam's depth into the target increases so does the potential of the source reconstruction, the uniformity is lost and the hotspot begins to break apart and separate into smaller hotspots rather than a singular uniform extended source distribution, as shown in the AM 14 reconstruction. This separation of the source distribution is in part due to the noise in the image space and lack of counting statistics in the photopeak leading to a less even distribution of events along the entire path of the beam. It is also worth noting that for such a high dose rate, the detection time was less than a minute for both measurements leaving little time for data collection hindering the statistics.

Figure 5.27 compares the 1-D profile of AM 13 and AM 14 to their expected Bragg peak locations and threshold depth for the 718 keV emission.

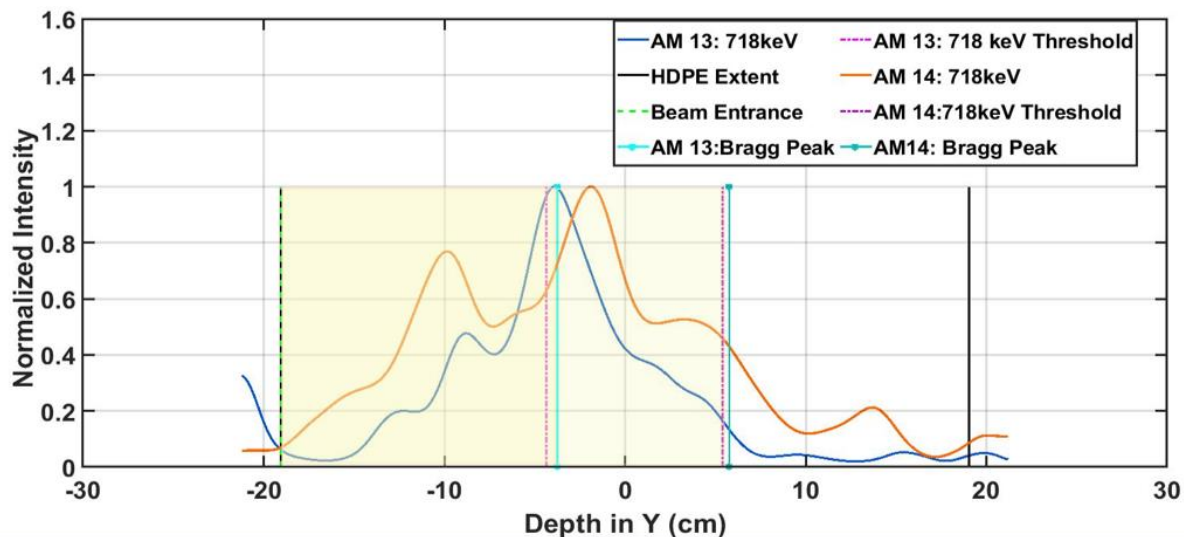


Figure 5.27: 1-D profile comparison of the 718 keV image reconstructions for measurements AM 13 and AM 14.

The 1-D profiles reveal a slight increase in depth for the AM 14 emission profile in comparison the AM 13, however it does not align with the threshold location. These profiles also show very similar features around the -10 cm depth and trailing decay past the peak locations, these similarities and closeness in depth of the peaks could be due to the residual photons emitted from AM 13 being recorded in AM 14 data. During data collection there was less than a 30 second rest period between beams. It is plausible that at such a high proton beam energy and dose rate that there were enough 718 keV emissions from $^{10}\text{B}^*$ and the slower decay of ^{10}C that were collected from the AM 13 irradiation that could have been recorded during the AM 14 irradiation. This could have easily skewed the data collection to closer reflect that of the previous measurement. We also see that the AM 14 profile does not drop to less than 50% intensity until its theoretical threshold depth.

From the image reconstructions shown, it is quite difficult to pick a stopping point of the 718 keV emission due to its hill-and-valley Gaussian like curvature, therefore we rely on the peak location to provide an estimate of the Bragg Peak location for the above measurements. Utilizing the curve fit equation provided in Figure 5.22, we can estimate the proton beam's incident energy and thus its theoretical depth in the HDPE target. Figure 5.28 demonstrates the estimated incident proton energy from the peak location from the image reconstructions of the 718 keV emission for the AM measurements. The same peak locations are used to estimate the expected 22 MeV proton energy threshold.

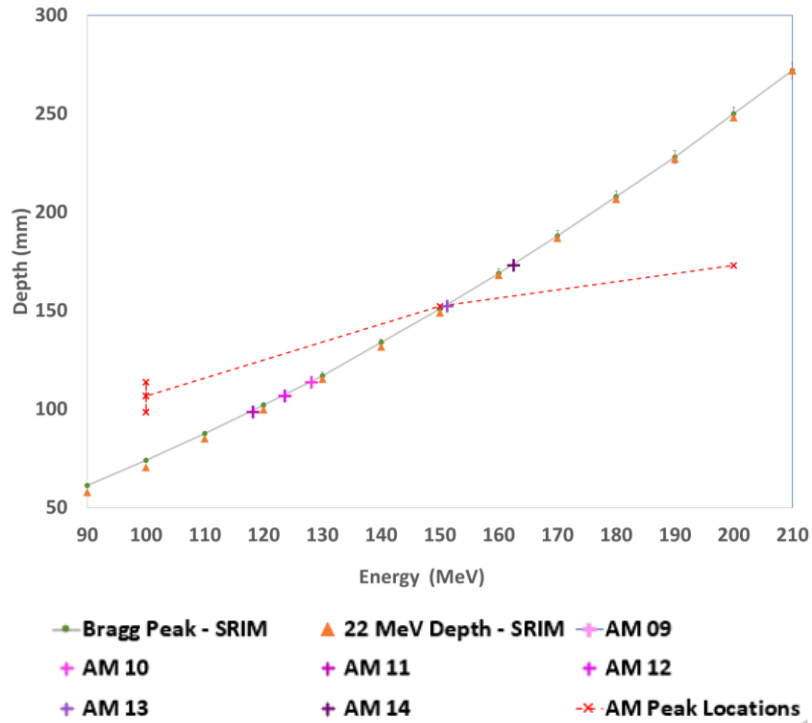


Figure 5.28: Estimation of the incident proton energy and threshold depth from the peak positions of the 718 keV image reconstructions for the M400 AM measurements.

The data fit shows that the AM 09-12 result is nearly a 20 MeV overestimate of the proton beam originating energy whereas AM 13 comes the closest to its originating proton beam energy followed AM 14 which is under by only 40 MeV. The threshold depth estimate is also best shown by AM 13 whereas AM 14 results in a depth closer to AM 13. Further fitting parameters could be

included to better approximate the beam's end point using the peak location of the 718 keV emission profile from image reconstruction. Although, AM 09-12 results in an over estimation the proximity of their estimate to one another for the same beam energy provides promise of the 718 keV emission, or any photon that results in a high energy threshold with a high branching ratio, being used as a PG emission for imaging analysis for comparison to the Proton's Bragg peak location.

As the proton energy and depth into the target increased so does the elongation of the 718 keV emission profile in imaging. This could be leveraged with improved results from possible longer measurement times and careful attention to the time frame in between beams. With closely impinging beams we run the risk of residual photons causing a miscalculation in the next beam's analysis due to late photons from the previous beam while PGs are being recorded for the current beam, as we saw from AM 13 to AM 14.

5.4 Verification Method II: 4.44 MeV Imaging

The 4.44 MeV emission from the carbon nuclei-proton interactions, has been of particular interest in proton radiotherapy for estimating the location of the Bragg peak within a carbon-rich material [50], [72], [89]. The 4.44 MeV PG can be derived from two modes of nuclear spallation with carbon,

$$(1) {}^{12}\text{C}(p, 2p){}^{11}\text{B}^* \rightarrow 4.444 \text{ MeV}$$

$$(2) {}^{12}\text{C}(p, n){}^{12}\text{N}^* \rightarrow 4.438 \text{ MeV}$$

and inelastic scattering on ${}^{12}\text{C}$ can cause the carbon nuclei to become excited and emit a 4.438 MeV gamma ray. Of these three modes the excitation of the ${}^{12}\text{C}$ atom results in the lowest threshold energy of approximately 5.1 MeV as it only requires a little more energy than that of the first excited state. The first nuclear spallation reaction requires the proton have an energy of at least

17.3 MeV and results in a PG emission on the same timescale as the deexcitation of the ^{12}C atom, at $6.1\text{E-}14$ seconds [65]. The second reaction could be considered a delayed photon emission as the excited ^{12}N has a half-life of 11ms.

5.4.1 Simulation Analysis

Knowing that the threshold energy of the 4.44 MeV photon is around 5.1 MeV suggests that this photon could easily be seen near the end of a highly energetic beam as the proton could travel nearly its entire path before it reaches an energy below 5.1 MeV and coming to rest. Figure 5.29 shows a 2-D profile of the 4.44 MeV emission on a simulated HDPE target using *PGCCS*.

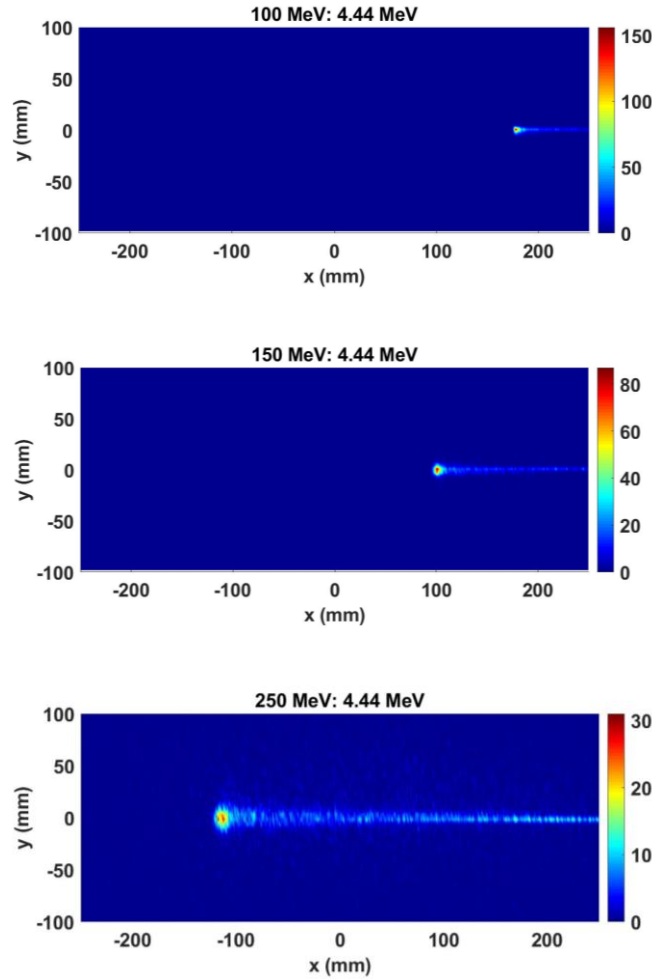


Figure 5.29: Simulation of the 4.44 MeV gamma ray distribution within a HDPE target.

The 2-D profiles show that the 4.44 MeV emission does not deviate much from the beam path and the most intense point of the emission corresponds closely to that of the proton beam's end point. As the energy of the proton beam increases so does the non-uniformity in the 4.44 MeV emission profile, as there are more chances of carbon-proton scatter at such a high incident energy. However, for this target, the profiles are consistent as a function of energy.

The *PGCCS* simulation utilized 1E9 incident protons for each initial energy however, the overall number of 4.44 MeV photons to reach the Polaris J3 detection system resulted in poor photopeak statistics, see Figure 5.18. With low statistics it is infeasible to image the photopeak using an iterative method like MLEM as the convergence of the image reconstruction will suffer. The low number of events collected by CZT at this energy could be attributed to several factors, one being the inherent worsened energy resolution for CZT at this energy due to dynamic range limitations, the tendency of the photon to undergo pair production prior to reaching the detector, and the down scatter of the photon along its path. It has also been shown that the PG emission is nearly isotropic, with the detector system parallel to only one side of the target, this leaves room for many other photons to escape detection [84]

5.4.2 Experimental Analysis

The low statistics seen in simulation translates to data collected experimentally. The H3D-J (formerly known as Polaris J3) detector was used for a 70 MeV proton beam irradiation of an HDPE target shown in Figure 5.30. For this experiment, H3D-J is 30 cm away from the HDPE target on top of the patient bench and the beam with its trajectory going from left to right center of the target.

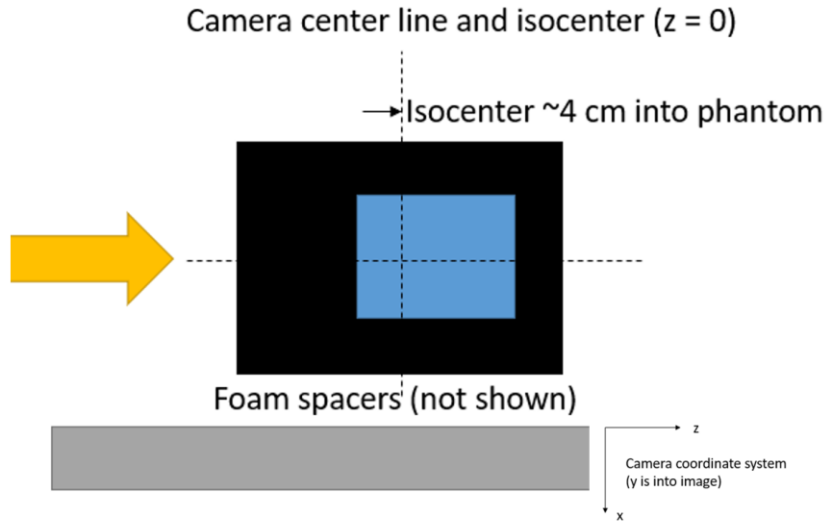


Figure 5.30: Proton beam measurement setup using the Polaris J3 (black) detection system at the MPTC with a $12.5 \text{ cm} \times 12.5 \text{ cm} \times 5 \text{ cm}$ HDPE target (blue). The patient bench is shown in gray. *Not drawn to scale.*

A 70 MeV proton beam has an expected depth of 4 cm before coming to rest in an HDPE target with a density of 0.97 g/cm^3 . To estimate this location the 4.44 MeV photopeak recorded from this experiment was imaged using ROI-MLEM. Figure 5.31 shows the energy spectra of all imageable events (2–5-pixel events) and the desired 4.44 MeV photopeak region used for standard 4π MLEM imaging. The energy window is large, 4.38–4.5 MeV, to compensate for the broad and dampened photopeak due to worsened energy resolution and other conflicting factors. In Figure 5.31 the 5th, 15th, and 25th iterations of standard MLEM are showing that the image reconstructions of this photopeak results in very poor convergence and high-frequency noise artifacts which hinders the image quality and fidelity for beam range verification analysis.

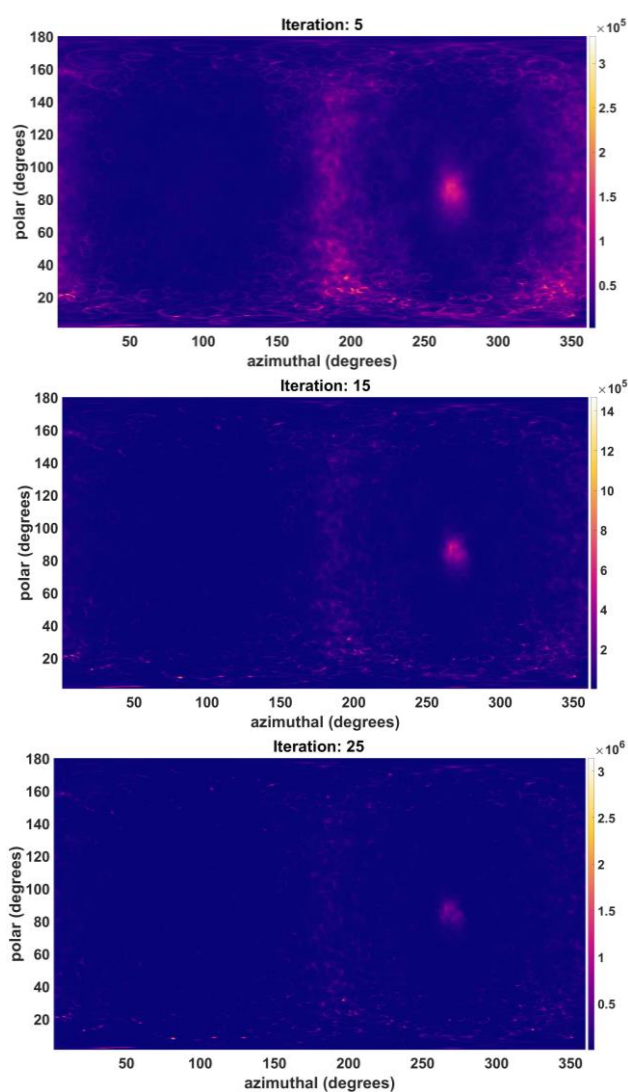
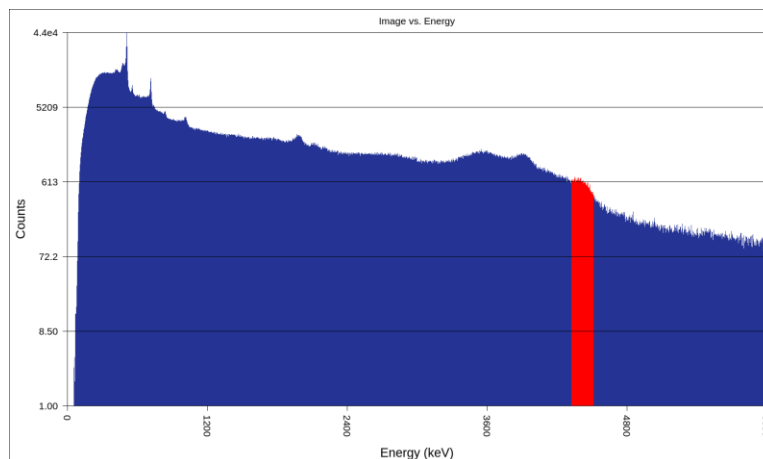


Figure 5.31: 4π image reconstructions of the 4.44 MeV photopeak (highlighted in red) using standard MLEM.

For the ROI-MLEM reconstruction, the same photopeak energy window was used, and the ROI was set to a 90° window about the center of the target dimensions $[10 \text{ cm} \times 10 \text{ cm}]$. Figure 5.32 shows the ROI-MLEM image reconstruction using a pixelation of 450×450 resulting in average pixel resolution of 0.01 cm^2 . Using ROI-MLEM allows for the mitigation of noise in the image space due to mostly pair production events and missequencing. The ROI Image was further truncated post-processing to show only the 4.44 MeV emission distribution within the target dimensions, which shows that the max intensity is within range of the expected distal fall-off of the proton beam.

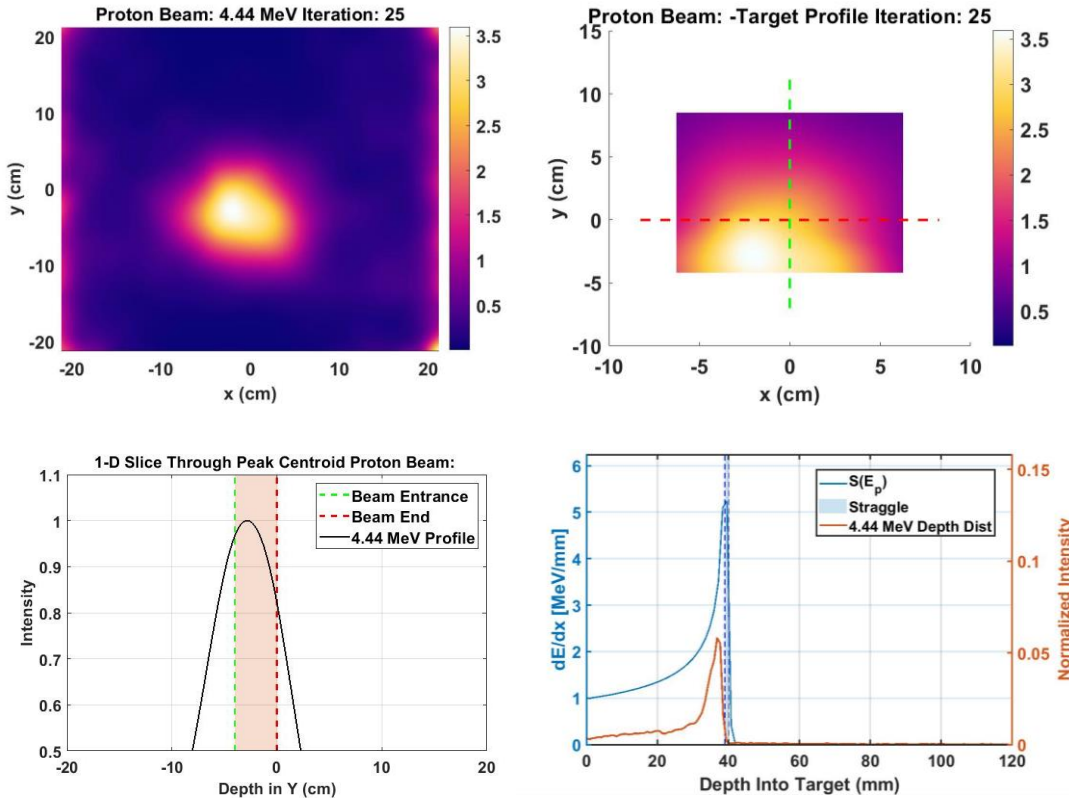


Figure 5.32: ROI-MLEM reconstruction of the 4.44 MeV photopeak. The image reconstruction is truncated to the size of the target profile. The green dotted line indicates the trajectory of the beam upward from the negative y-direction and the red dotted line indicates the beam's end point. The 1-D slice profile is taken from the values along the y-direction through the peak centroid of the image reconstruction.

However, the 1-D profile shows that the peak centroid is further from the beam's end than expected from SRIM and *PGCCS* simulations. The peak centroid location is at -2.73 cm +/- 0.21 cm, 1.27 cm away from the intended beam end point. The expectation is that the 4.44 MeV peak centroid is to be no more than 0.31 cm from the Bragg peak location as estimated by SRIM and *PGCSS*. This misalignment in the peak centroid could be due to a number of possible causes, some listed here:

1. Detector resolution: with worsened energy resolution comes worsened Compton cone estimation which can skew the lever arm directionality and opening angle calculations.
2. The noisiness of the data set: in proton beam measurements the high levels of radioactivity can cause chance coincidence events, partial energy deposition events, and event pile-up which also hinders (1) and skews Compton cone estimation.
3. Pair production events: At this energy the possibility of the PG undergoing pair production is heightened. This means that these events are recorded as imageable Compton photopeak events, which only results in noise.
4. Statistics: without enough true Compton imaging events beneath the photopeak the image reconstruction suffers, causing a low likelihood estimate from the MLEM algorithm and cause a poor convergence which could pull the source distribution from its true location.

Further spectral analysis outlined in Chapter 6 reveals the difficulties of detecting and imaging this photopeak in the high flux environment of proton therapy. Experimental image results provided by ROI-MLEM shows that there is promise in using this photopeak or low energy threshold photopeaks for PBRV. Depending on the concentration of the element of interest in the target, inelastic scattering causing the excitation of the intended nuclei will always result in a

threshold energy slightly higher than that of the 1st excited state gamma ray. Therefore if the excited state gamma-ray energy is below 10 MeV we can expect its threshold to be within vicinity of the Bragg peak of typical therapeutic beam energies.

5.4.3 Analysis Summary

To successfully obtain spatial distribution information from PG emission to describe the proton's energy loss as a function of depth, there are apparent limitations that must be addressed. The high flux of photons cause noise spectrally that it is transferred to the Compton cone reconstruction which produces noise artifacts in the image space. ROI-MLEM shows that much of that noise can be mitigated through truncating the imaging space. However, the image convergence is not reaching the desired resolution to definitively predict the location of the proton beam endpoint from the PG emission profile.

When comparing the image reconstruction in Figure 5.33 of the 718 keV PG line to that of the 4.44 MeV emission for the experimental measurement shown in Figure 5.32, the 718 keV image shows a smaller and more concise hotspot than the 4.44 MeV. The peak centroid also converges closer to the beam's end than the 4.44 MeV reconstruction, which is not expected based on theory.

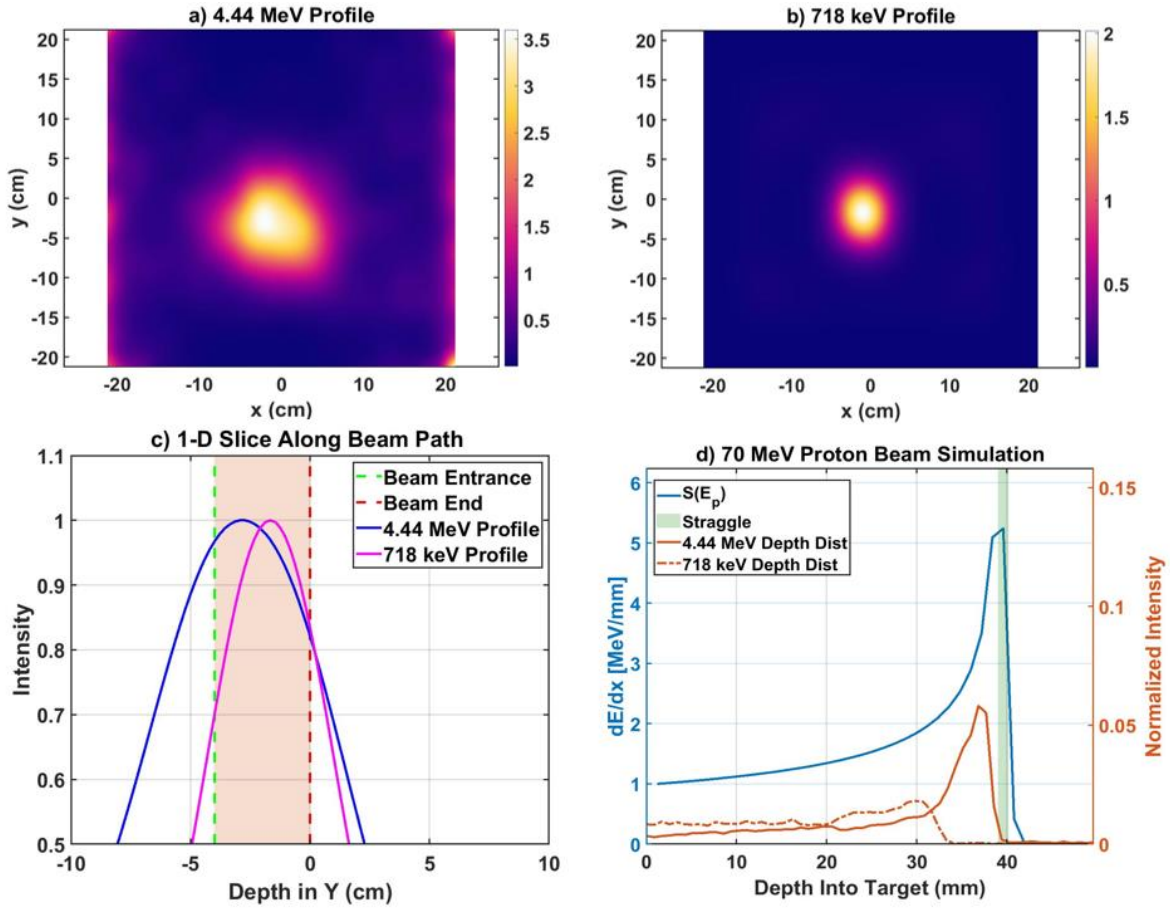


Figure 5.33: $90^\circ \times 90^\circ$ ROI image reconstructions with a 0.02 cm^2 pixel resolution of the (a) 4.44 MeV and (b) 718 keV prompt gamma rays. (c) A 1-D slice is taken through the peak centroid of each image to show the profile of the events along the beam path. This is compared to the (d) simulated Bragg curve of a 70 MeV proton beam incident on a C_2H_4 target ($\rho = 0.97 \text{ g/cm}^3$).

The better performance of the 718 keV image reconstruction is due to the improvement in detection efficiency at this energy in comparison to the 4.44 MeV photopeak. In Figure 5.33 (a) there are noise artifacts around the perimeter of the image reconstruction. Although ROI-MLEM converges to the source's hotspot, these noise artifacts indicate there are strongly intensified artifacts outside the desired FOV which affects the image reconstruction. Chance coincidence, pair production, and partial energy deposition events of higher energy photons also play a role in the increased FWHM of the 4.44 MeV reconstruction in comparison to the 718 keV reconstruction.

The peak centroid location of the 718 keV is at $-1.68 \text{ cm} \pm 0.21 \text{ cm}$, when comparing this to SRIM estimated threshold depth the peak is underestimated by 0.6 cm. This estimate is promising as the estimate threshold depth is depicted as the point at which at least half the photons reach an energy of 22.1 MeV. Further corrections could be applied for a better fit. As for the 4.44 MeV image reconstructions, improvements in detection efficiency of imageable photopeak events must be made to see improvements in imaging.

CHAPTER VI

CZT Detector Considerations for the Improvement of Prompt Gamma Ray Detection

6.1 Introduction

Over the past 10 years, CZT has shown its capabilities of high-performance operation at room temperature, providing 0.3% FWHM at 662 keV. Improvements in temperature corrections, sub-pixel sensing, and ASIC design have all contributed to the improvement of the detection efficiency and imaging capabilities of these semi-conductor systems[24], [90], [91]. However, experimentally CZT's performance degrades as the energy of the photon increases above 2 MeV and the timing resolution of CZT has always been a limiting factor in comparison to other types of detectors such as scintillators [92], [93]. Typically the resolution degrades following a $1/E$ slope along with detection efficiency, but the expectation from simulation analysis have shown that the resolution should prove to remain constant provided a wide enough dynamic range and energy calibration.

For the application of proton beam range verification (PBRV) the tradeoff between detection efficiency, energy resolution, and timing resolution must be well balanced to achieve quality and quantitative results to compare the prompt gamma (PG) emission to that of the proton beam profile. In practice, modular analog ASIC CZT systems, digital ASIC systems, and large array CZT detectors have all been studied in their feasibility for PBRV, each providing different advantages

with similar limitations. There are significant places for improvement for these systems that could allow for improvement in detection efficiency at high energies which could lead to improved imaging results for PBRV.

6.2 Analog and Digital Systems for Prompt Gamma Ray Detection

Two of the stark differences between analog and digital ASIC based CZT, in practice, is the dynamic range provided and the timing resolution. Analog based CZT provides much faster timing as it is easier to process analog data rather than digitize the data to process. In comparison to digital CZT for the same number of crystals, the timing resolution is upwards of three times as fast for analog systems, where the digital averages 10,000 cps per crystal in the S400x system. On the other hand, the dynamic range for analog systems has been limited to 3 MeV for analog systems where the digital ASIC CZT can offer a dynamic range up to 9 MeV, allowing for superior high energy event reconstruction. However for both detector system types the energy calibration is limited to 2.6 MeV for a single pixel event. This is due to the highest available natural energy like is 2614 keV from ^{232}Th decay to ^{208}Tl . Orion research has shown that simple linear extrapolation is feasible for digital systems past this energy but still requires good statistical data for accurate calibration [94]. Digital CZT also offers the capability of sub-pixel sensing allowing for enhanced position resolution [27].

Both systems, for their distinct features, are tested on their performance in the high-flux photon environment of proton therapy and show promising capabilities of providing useful data for PBRV without the need of collimation based on prior knowledge and shielding. However, there is much room for improvement in both detector types before their practical use in real therapeutic settings, where the goal is *in-vivo*, real time analysis.

6.2.1 Simulation Analysis

Figure 6.1 shows the Geant4 simulation used to provide a benchmark on the expectations of CZT's detection efficiency at high energies, particularly at 4.44 MeV, with the pair production, Compton scatter, and photoelectric physics libraries implemented. An extended 4.44 MeV (1 in \times 3 in) source is placed 30 cm away from the front plane detector geometry to mimic an experimental PuBe source and setup depicted later in section 6.2.2.

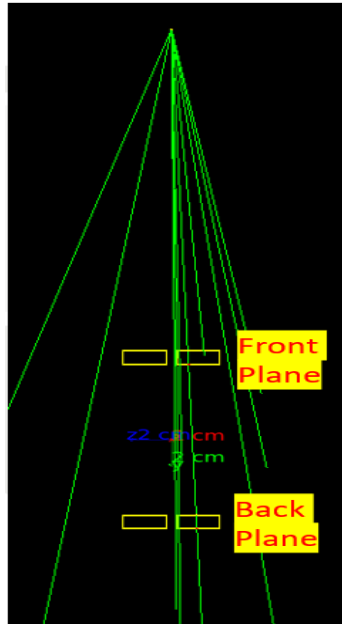


Figure 6.1: Geant4 simulation of two 2 \times 2 CZT arrays with 11 cm separation, 30 cm away from a 4.44 MeV source.

Two 2 \times 2 arrays are simulated with a 11 cm separation distance between both planes of detectors. Figure 6.2 shows the energy spectra recorded for all events measured and those events flagged as interplanar, or “coincidence” events are shown as well. These coincidence events are events that interacted at least once with both planes of CZT. Of the 20 million gamma-ray simulated, at least 15% of all events are recorded as interplanar events. Figure 6.2 shows that the number of photons beneath the single escape, double escape, and photopeak are within proximity

of one another. The photopeak results in the fewest number of events as the probability of pair production becomes more dominant than Compton scatter at higher energies.

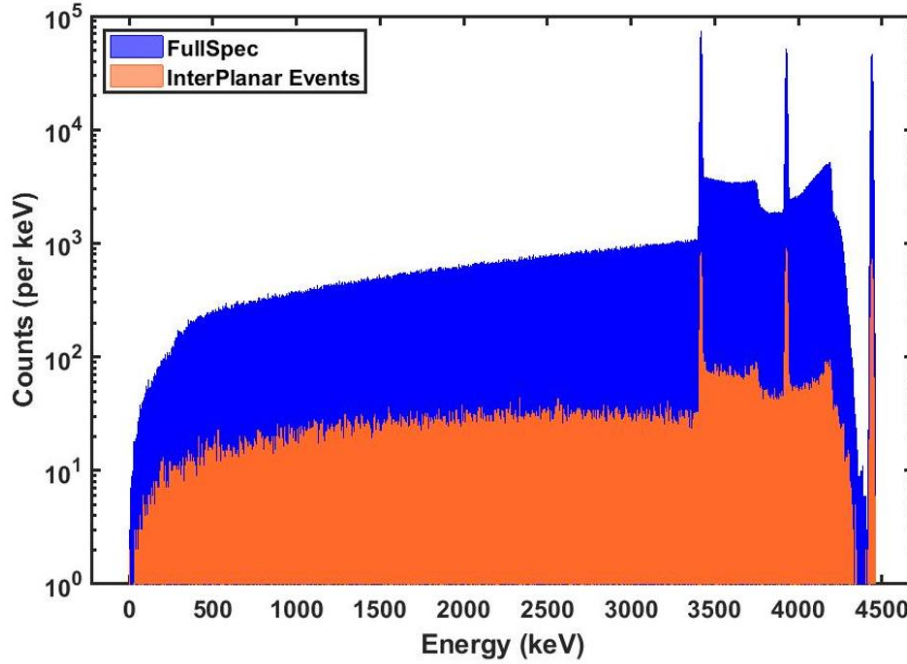


Figure 6.2: Recorded energy spectra from 4.44 MeV Geant4 simulation comparing the spectrum of all recorded events to the spectrum of coincidence events.

The non-interplanar spectra shows similar results in peak ratios when comparing the spectra of events that interacted in either array independently, as seen in Figure 6.3. As expected, the back plane resulted in fewer recorded events as the attenuation through the first plane of detectors could have caused some events to scatter away from the back plane or to be fully absorbed before reaching that plane.

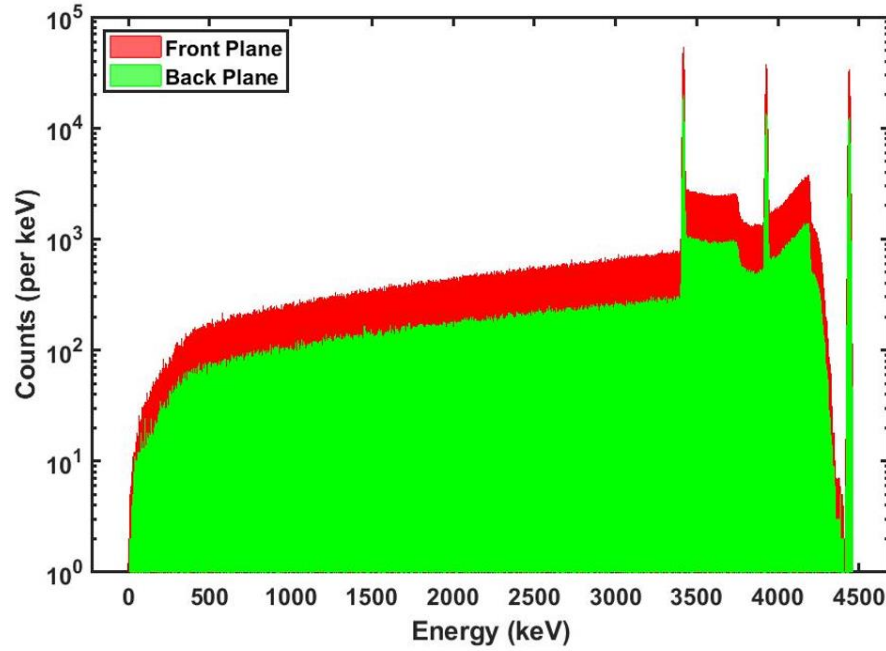


Figure 6.3: Recorded energy spectra from 4.44 MeV Geant4 simulation for each CZT array independently recorded events.

Both planes of CZT result in very narrow photopeaks averaging a FWHM of 15 keV. The photopeaks for both planes average 50,000 events. This is only a quarter of a percent of all gamma-rays emitted and many of these events resulted in pair production events, leaving not many events that were solely Compton scatter events for imaging analysis, as illustrated in Figure 6.4.

Figure 6.4 shows the energy distribution of individual interactions for each gamma-ray emitted recorded by CZT as 2-pixel, 3-pixel, or 4-pixel events that summed to a full energy deposition within the window of 4.34 to 4.54 MeV.

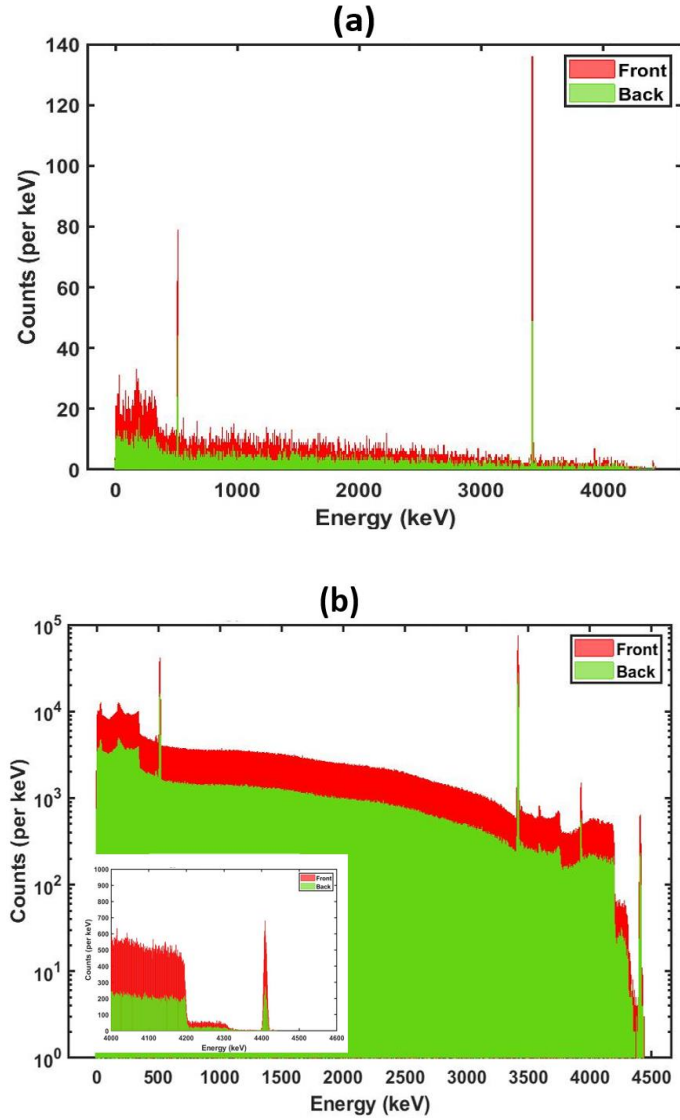


Figure 6.4: (a) Interplanar interaction distribution of each coincidence event as a function of energy. (b) Non-interplanar interaction energy distribution for each plane's independently recorded events.

The interplanar interaction distribution shows that majority of the photopeak events are a product of the summation of the double escape peak and full energy deposition 511 keV photons. There is also a tall shelf below 350 keV that could be from more forward scatter events meaning there was a very high energy deposition events followed by a lower energy scatter or multiple low energy scatters. Nonetheless, our imageable range of events from interplanar interactions is

dominated by pair production. The same can be said for the non-interplanar events when focusing on Figure 6.4(b). The independent plane spectra show we see many near photopeak single scatter events at 4.40 MeV meaning that the adjoining scatter would be of very little energy, equal to or less than 40 keV. This does not negate the 511 keV peak and single and double escape peaks that are indicators of pair production being a dominant mode of interaction of 4.44 MeV gamma-rays in CZT. The single escape peak presence indicates that one of the annihilation photons deposited its energy in very close proximity to the gamma-ray's location and was collected as a single event.

To provide quality images from interplanar events, in theory the forward scattering events, that are expected from the Klein-Nishina cross-section at this energy, will produce small opening angle Compton cones[19]. With correct sequencing, these small-opening cones should point directly back to the source location with little uncertainty and spread in the source distribution. Other research suggest that there is an optimal separation distance for interplanar events at 4.44 MeV, that results in improving the detection efficiency and enhancing the image reconstructions[64]. When imaging all imageable events recorded using ROI-MLEM, Figure 6.5 shows a very blurry reconstruction of the 1 inch by 2.5 inch extend source. The noisy blur of the source distribution is in part due to the number of pair production events recorded as full energy deposition events. Shy shows that the opening angle of these events are near 10° which is with range of our expected forward scatter events [18].

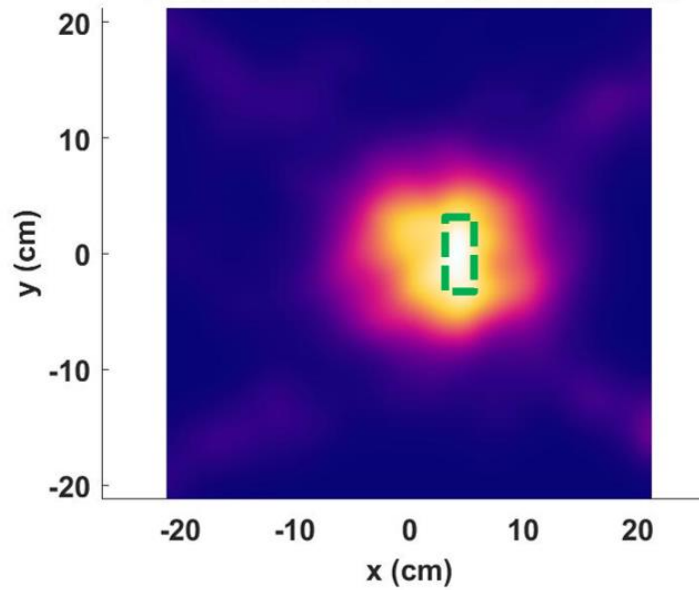


Figure 6.5: ROI-MLEM image reconstruction of the Geant4 simulated extended 4.44 MeV source, with the expected distribution outlined in green.

Simulation shows that with this detection geometry we can achieve well-defined photopeaks at 4.44 MeV using CZT. Although majority of the events result in pair production events there is still promising results from imaging those photopeak events.

6.2.2 Experimental 4.44 MeV Detection Analysis

A PuBe source measurement using the H3D digital system, S400X, in coincidence mode was conducted for spectral and imaging analysis for comparison to the simulated results. The analysis of this work looks at the spectra for each crystal in the detection geometry (totaling eight crystals: four per detector) for both interplanar (coincidence) and non-interplanar (single) events. Figure 6.6 shows the geometry setup used for primary focus on coincidence mode detection.

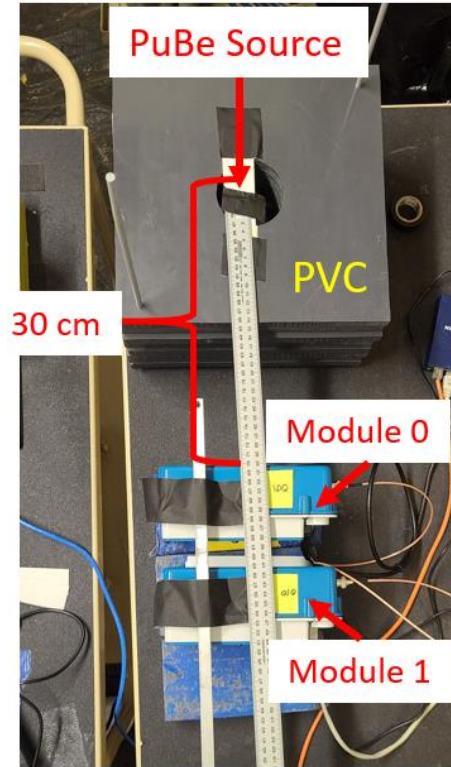


Figure 6.6: PuBe source experimental setup.

The S400X systems are placed parallel of one another and separated with an 11 cm distance and connected such that gamma rays that interact with both systems within a 11 ns window are recorded as coincidence events. The detectors are placed with the front side of Module 0 30 cm away from the PuBe source, which was placed in the center of PVC (polyvinyl chloride), used to both attenuate the neutron emission and cause the emission of the 6.1 MeV photons from neutron activation on chlorine in the PVC. Figure 6.7 shows the recorded energy spectra for both the coincidence events and the single events.

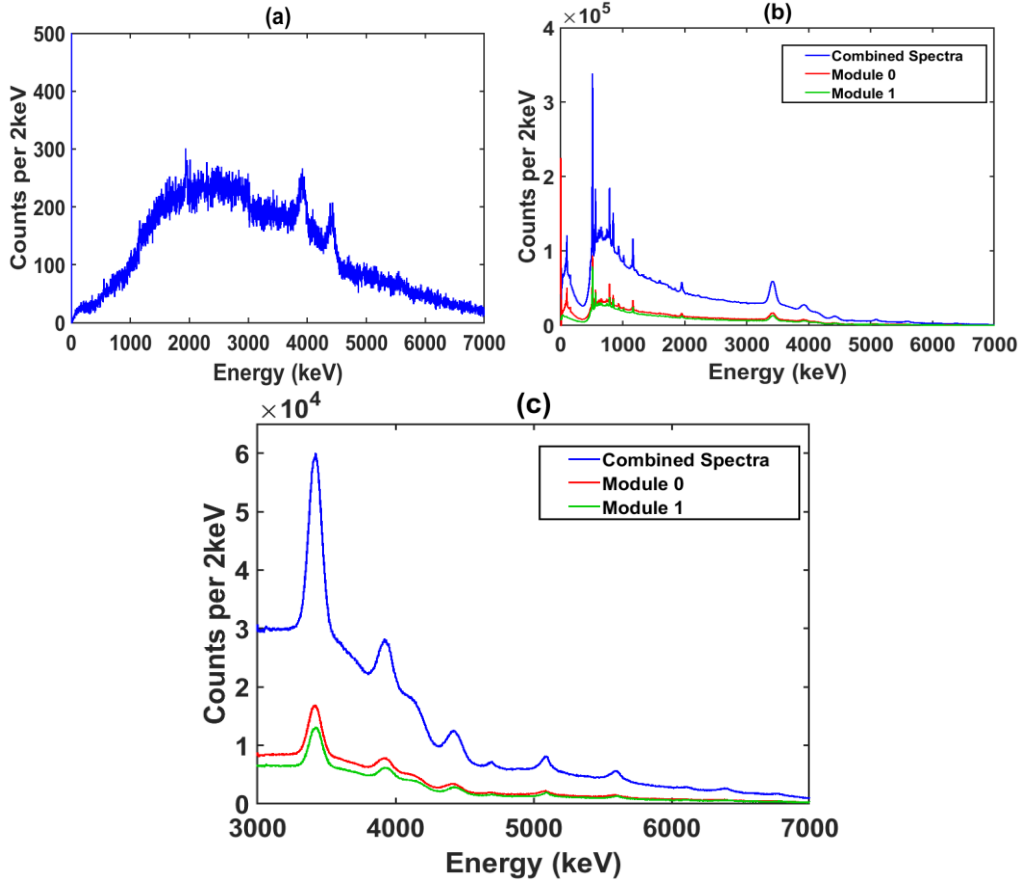


Figure 6.7: PuBe measurement energy spectra results. (a) Recorded coincidence energy spectrum. (b) Recorded single events energy spectra. (c) Single events energy spectra with special attention to the 4.4 MeV and 6.1 MeV photopeaks.

The coincidence energy spectrum shows two orders of magnitude less photopeak events in comparison to the combined single events energy spectrum. There is no 511 keV and single escape peak in the coincidence energy spectra as expected from simulations. This could suggest that the annihilation photon either scattered away from the detectors or happened fast enough within the coincidence timing window that the full photopeak energy was collected. However, when comparing the percentage of full photopeak events to the single and double escape peaks for both experimental and simulation results showed in section 6.2.1, there is some discrepancy in the ratio of the number of events between peaks, as seen in Table 6.1.

RATIO	SIMULATED		EXPERIMENTAL	
	Coincidence	Single	Coincidence	Single
PP/DE	0.88 ± 0.03	0.63 ± 0.03	--	0.21 ± 0.19
PP/SE	0.83 ± 0.03	0.91 ± 0.03	0.78 ± 0.15	0.45 ± 0.21
SE/DE	1.07 ± 0.03	0.69 ± 0.03	--	0.47 ± 0.17

Table 6.1: Comparison of recorded peak events for the 4.44 MeV gamma-ray.

PP = Photopeak, SE = Single Escape, DE = Double Escape

The ratios calculated in Table 6.1 are taken from the number events beneath each peak provided a 50 keV window about each peak, experimentally, and a 20 keV window for simulations, which are both normalized by the window width. Table 6.1 shows a consistent ratio in peak events for the coincidence spectrum. Whereas experimentally the photopeak to single escape ratio is 5% less than that recorded from simulation and is worsened by 46% when comparing the single spectrum data. This suggests that many gamma-rays are lost experimentally at this high energy.

The omission of the 511 keV and single escape photopeaks in the coincidence energy spectrum could be the major contributor to event loss. Figure 6.8 shows the distribution of the 511 keV photopeak events from both the single and coincidence data combined over all CZT crystals. All events that resulted in a full energy deposition within the energy window of 500-520 keV were plotted in Figure 6.8, which shows that these events are not evenly distributed across all four crystals of each detector as expected.

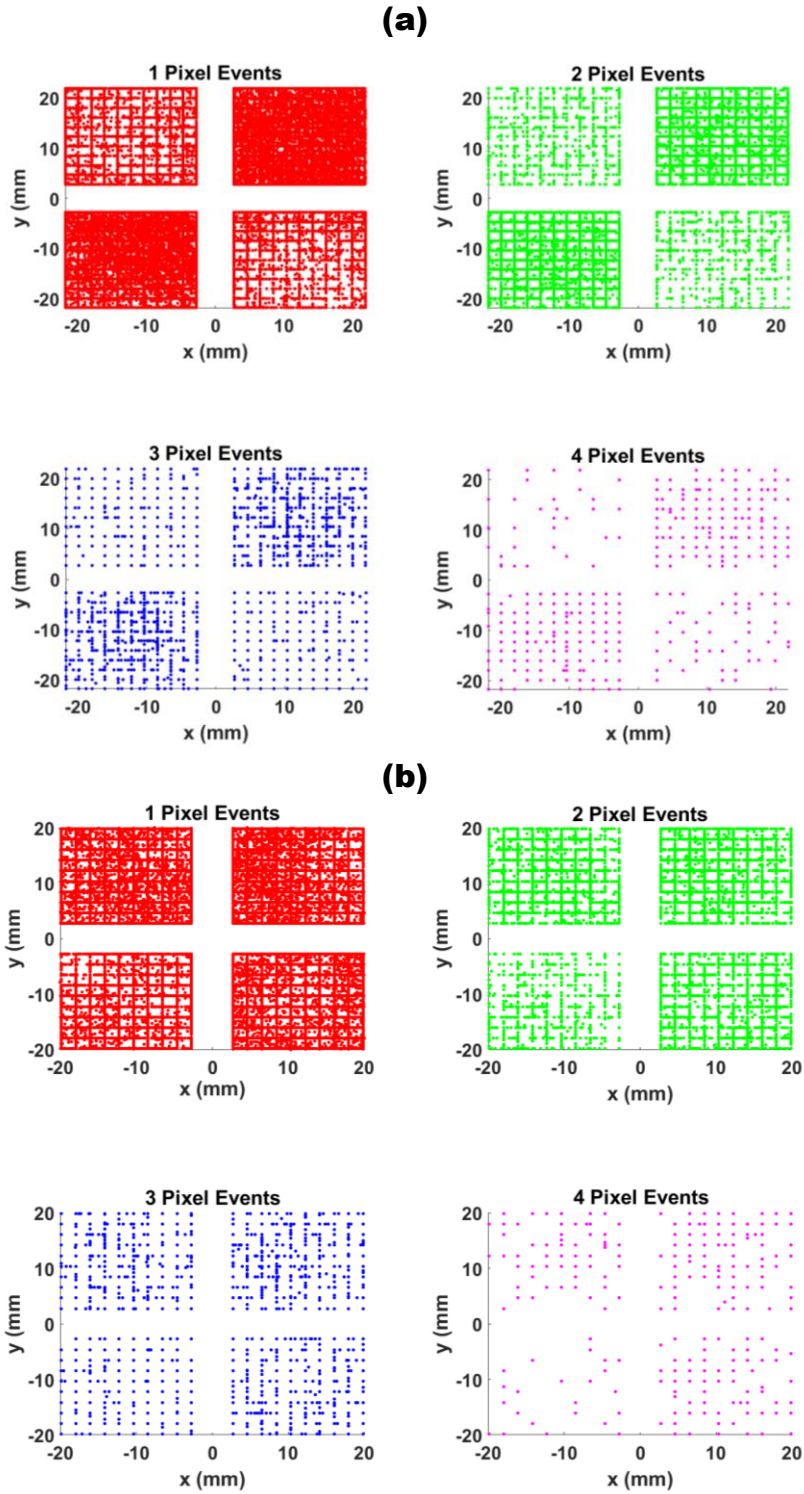


Figure 6.8: 511 keV event distribution across all crystals in (a) Module 0 and (b) Module 1

The distribution of events has a more apparent pattern in module 0 showing that less events are recorded in the top right-hand crystal and the bottom left-hand crystal, consistently for each event type. This may mean that there is some hardware issue causing some events to not be recorded. Table 6.2 shows the percentage of all reconstructed 20 million events over all energies recorded by both detectors distributed over each crystal.

Module 0			Module 1		
1 Pixel	<u>Crystal 1</u> 9.9%	<u>Crystal 2</u> 41.3%	1 Pixel	<u>Crystal 1</u> 26.2%	<u>Crystal 2</u> 30.0%
	<u>Crystal 3</u> 39.6%	<u>Crystal 4</u> 9.2%		<u>Crystal 3</u> 14.4%	<u>Crystal 4</u> 29.4%
2 Pixel	<u>Crystal 1</u> 6.0%	<u>Crystal 2</u> 45.8%	2 Pixel	<u>Crystal 1</u> 25.6%	<u>Crystal 2</u> 34.6%
	<u>Crystal 3</u> 43.2%	<u>Crystal 4</u> 5.0%		<u>Crystal 3</u> 11.3%	<u>Crystal 4</u> 28.5%
3 Pixel	<u>Crystal 1</u> 5.4%	<u>Crystal 2</u> 46.8%	3 Pixel	<u>Crystal 1</u> 26.2%	<u>Crystal 2</u> 35.9%
	<u>Crystal 3</u> 42.8%	<u>Crystal 4</u> 5.0%		<u>Crystal 3</u> 9.1%	<u>Crystal 4</u> 28.8%
4 Pixel	<u>Crystal 1</u> 6.2%	<u>Crystal 2</u> 42.1%	4 Pixel	<u>Crystal 1</u> 26.4%	<u>Crystal 2</u> 41.7%
	<u>Crystal 3</u> 42.1%	<u>Crystal 4</u> 9.6%		<u>Crystal 3</u> 7.7%	<u>Crystal 4</u> 24.2%

Table 6.2: Distribution off all events recorded by both modules for each crystal

The distribution of all recorded events closely mimics that of the 511 keV distribution, where we would expect an even distribution of events across all energies. The PuBe source used in this measurement is considered a hot source, well over 10Ci and could have caused saturation issues over time for the detectors, though the dead time revealed to remain constant. The cause of the uneven spread in the event reconstruction is unknown but believed to be a major factor in the poor spectral results in comparison to expectations from simulations. Figure 6.9 shows the ROI-

MLEM image reconstruction with same pixel resolution as shown for the simulation results, which are comparable in the noise spread of the source distribution.

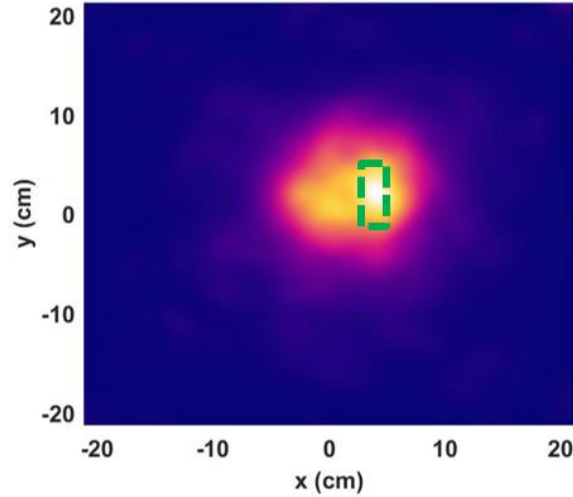


Figure 6.9: 4.44 MeV photopeak image reconstruction from the combined single event spectrum using ROI-MLEM.

Although the photopeaks in both the single and coincidence data for the 4.44 MeV resulted in low counts, due to the wide dynamic range of the S400X system we can see other spectral features out past this energy. Referring to Figure 6.7, the single data shows the photopeak and escape peaks for the 6.1 MeV photon from chlorine and a 4.7 MeV line believed to be an activation line of the aluminum in the case of the S400X system. This shows that with the wide dynamic range we can detect high energy events however the poor statistics are still under investigation. The following sections assesses the M400 systems capabilities in detecting the 4.44 MeV photon but in a much more radioactive environment provided by proton beam irradiation.

6.2.3 Experimental Prompt Gamma Detection Analysis

Two S400X and two M400 systems were used for proton beam measurements at the Maryland Proton Therapy Center (MPTC) for analysis of their capabilities of prompt gamma ray detection. Figure 5.23 in Chapter 5 shows the experimental setup used for prompt gamma-ray

imaging with these systems and Table 6.3 lists again the proton beam specifications and in addition, notable spectral features, and detector characteristics for each beam irradiation.

Beam#	Energy	Dose Rate	Total Dose	Photopeaks	Notes
7	150 MeV	50 kMU/min	50 kMU	718, 511 only	Spike in low energy events
8	92.5 MeV	50 kMU/min	200 kMU	No photopeaks recorded	
9	100 MeV	50 kMU/min	100 kMU	No photopeaks recorded	Beam went offline mid dose Loss of one crystal in each system
10	100 MeV	50 kMU/min	100 kMU	4.44 DE only, 718, 511	~65-70% dead time 70-75% dead time Spike in low energy events
11	100 MeV	100 kMU/min	100 kMU	511 only	90% dead time 70-75% dead time
12	100 MeV	150 kMU/min	100 kMU	718, 511 only	~95% dead time 70-75% dead time
13	150 MeV	150 kMU/min	100 kMU	718, 511 only Broad 3.5 MeV structure	~95% dead time 70-75% dead time
14	200 MeV	150 kMU/min	100 kMU	718, 511 only Broad 3.5 MeV structure	~95% dead time 70-75% dead time

Table 6.3: Proton Beam Measurements specifications. Red: M400 specific, Blue: S400X specific

Figure 6.10 shows the single or non-interplanar event spectra combined for both S400X modules for all measurements normalized by the 511 keV photopeak, revealing the major loss of photopeaks with increase in proton beam energy, dose, and dose rate. Measurements 8 and 9 performed the worst as they resulted in completed photopeak loss, with measurement 8 being the highest total dose and measurement 9 experiencing beam malfunction.

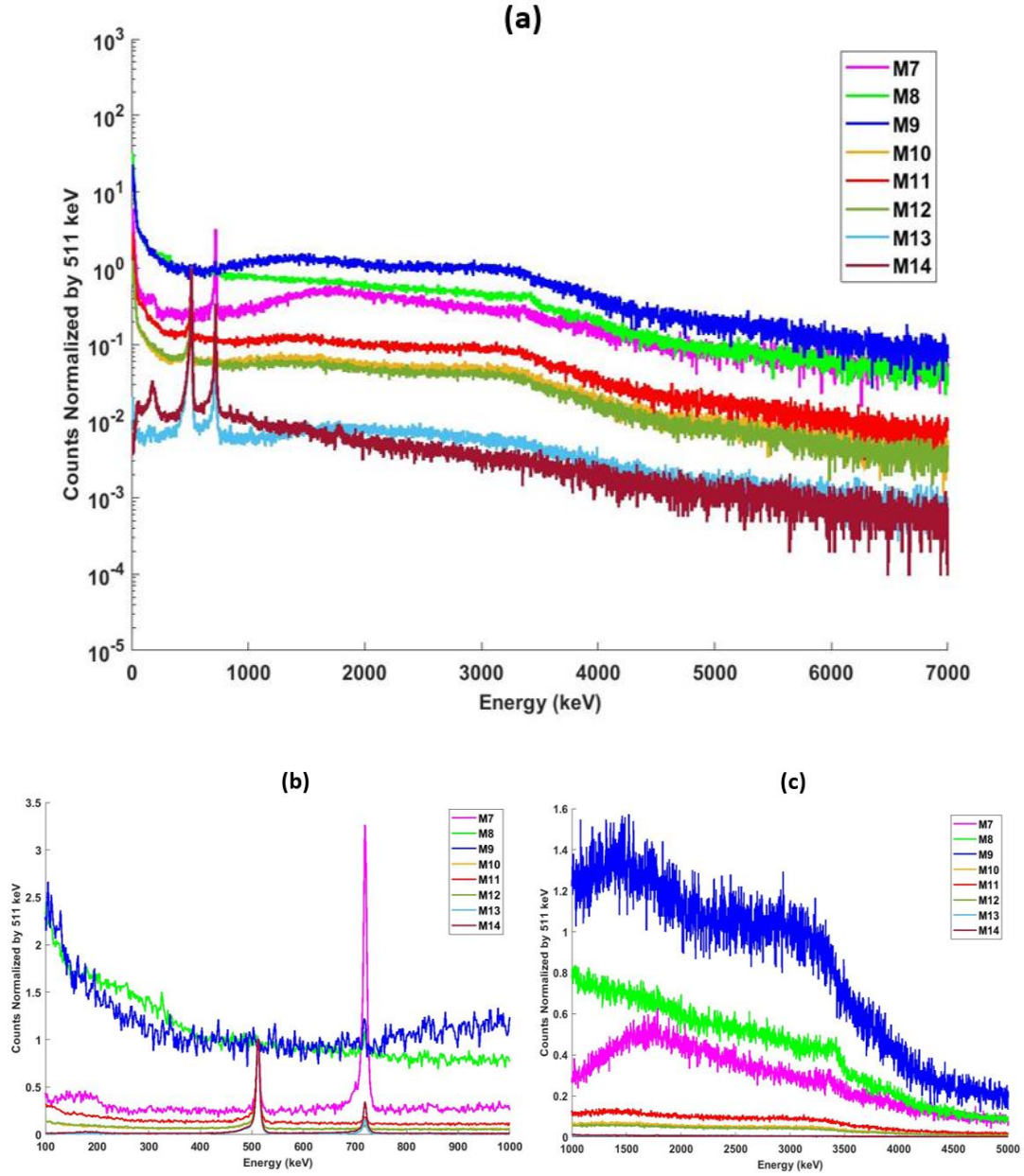


Figure 6.10: S400X Non-interplanar spectra for each proton beam measurement.

In the log-scale energy spectra plot of Figure 6.10, measurements 8 and 9 show a very high low energy tail even though the cathode energy threshold for these measurements were increased to mitigate low energy events (< 100 keV). This was not expected as increasing the energy threshold should have pushed the spectra to start at an energy above 0, with little to no events recorded until the threshold energy is reached. However, the opposite happened and the

change in the amount of high energy events recorded was negligible in comparison to all other measurements. The large low energy spike in events for measurement 9 is hypothesized to be the result of saturation and the high flux of events causing partial energy deposition events and poor event reconstruction. The high energy range spectral plot shows that for all measurements there are no true photopeaks seen for the 4.44 MeV line, however some result in a broad shoulder at the 4.44 double escape peak.

When focusing on the M400 system the improvement overall is the dead time, which stayed consistently below 80% for the duration of the measurements despite the loss of one crystal per system shown in Figure 6.11, which is thought to be attributed to the high-flux environment. The M400 systems also showed fair consistency in its spectral results for measurements 10-12 where the same beam energy and dose rate was used.

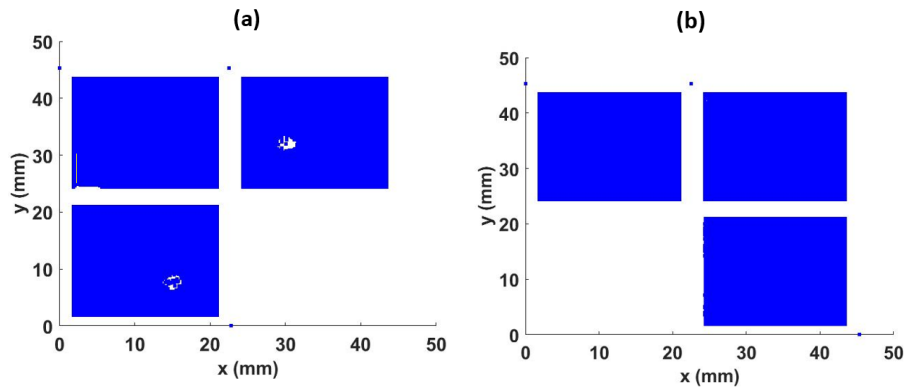


Figure 6.11: 3-D plot of all events recorded for measurement 10 in the M400 systems: (a) System 1 on the left and (b) System 0 on the right

Figure 6.12 and Figure 6.13 compares the energy spectrum for measurement 10 which is a full beam dose with no interruptions, and measurement 9, where the beam shuts off mid dose, respectively. In comparison to measurement 9, measurement 10 reveals a slightly lower low-energy shelf and much less events recorded beneath the 511 keV photopeak, which is also consistent for measurements 11 and 12. The break in the measurement 9 could have caused a spike

in event recording of delayed emissions. These measurements all displayed nearly the same results as they were all at the same energy and dose. Although, measurement 12 is of a higher dose rate, there was not a considerably noticeable increase in counts for this measurement in comparison to the previous beam measurements, as the total dose is kept constant. In these measurements (10-12) we see a slight increase in the number of high energy (> 1 MeV) events recorded.

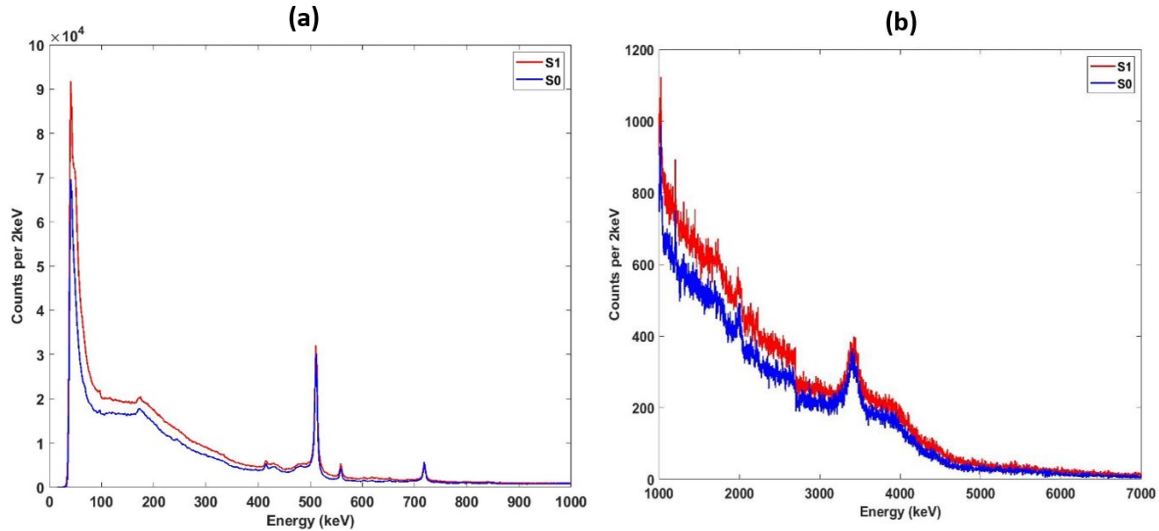


Figure 6.12: Recorded energy spectra for Measurement 10 for both M400 systems

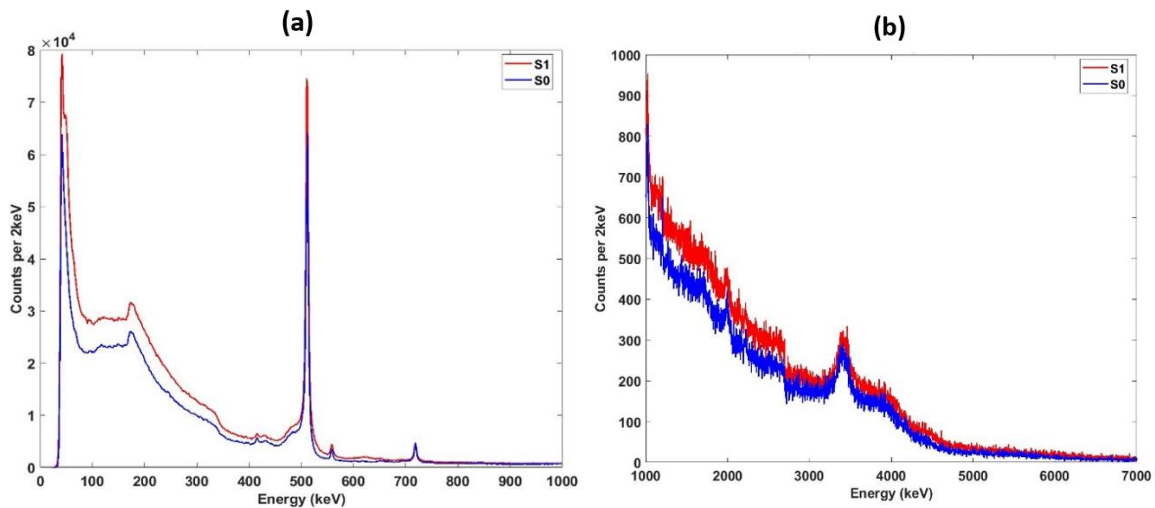


Figure 6.13: Recorded energy spectra for proton beam measurement 9 for both M400 systems

Measurements 13 and 14 are at the highest dose rate allowed and the two highest energies tested, 200 MeV being the highest energy allowed. Figure 6.14 shows the energy spectra recorded for measurement 13, both measurements showed nearly the same number of events recorded indicating that the change in proton beam energy did not significantly affect the overall detection. It is worth noting at this point the analog systems were around 75-80% dead time and that there was little to no rest time between beam irradiations.

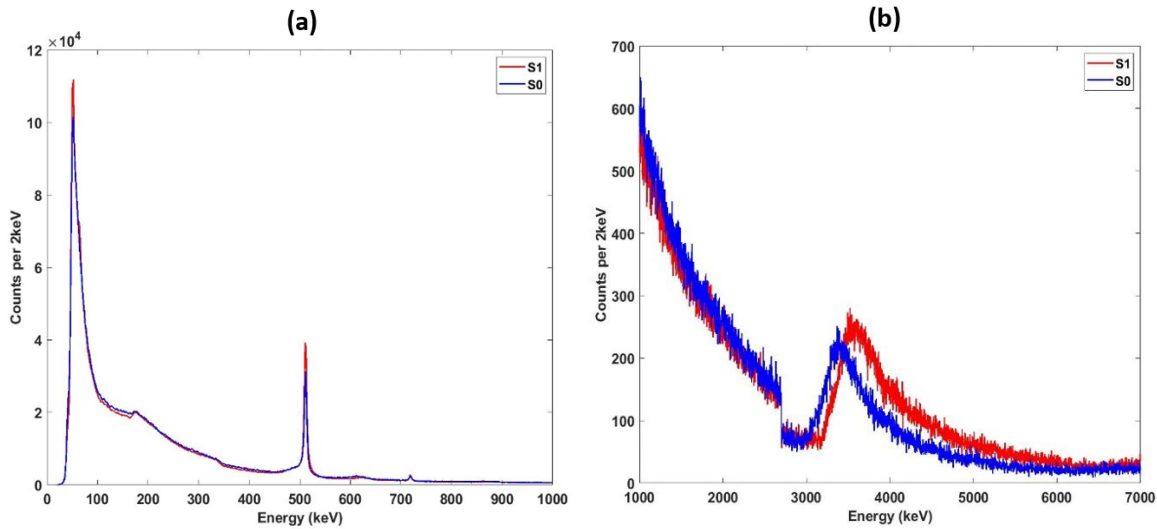


Figure 6.14: Recorded energy spectra for Measurement 13 for both M400 systems

Above 1 MeV, both measurements show an uncharacteristic hump around 3.5 MeV in the spectra and a hard shelf cut-off at 2.6 MeV. Figure 6.15 indicates that the hump is most prevalent in the recorded 2-pixel events and the hard drop in events is most prominent in the one-pixel events. The cut-off is explained by the energy calibration only being available up to 2.6 MeV and any single pixel event above this energy is not extrapolated out. However, the broad hump in the two-pixel events is still quite a mystery as it is not seen in the other measurements, but this could be due to the detectors approaching saturation in these measurements, not allowing enough time for proper event reconstruction of events past the 3 MeV dynamic range of the analog based systems.

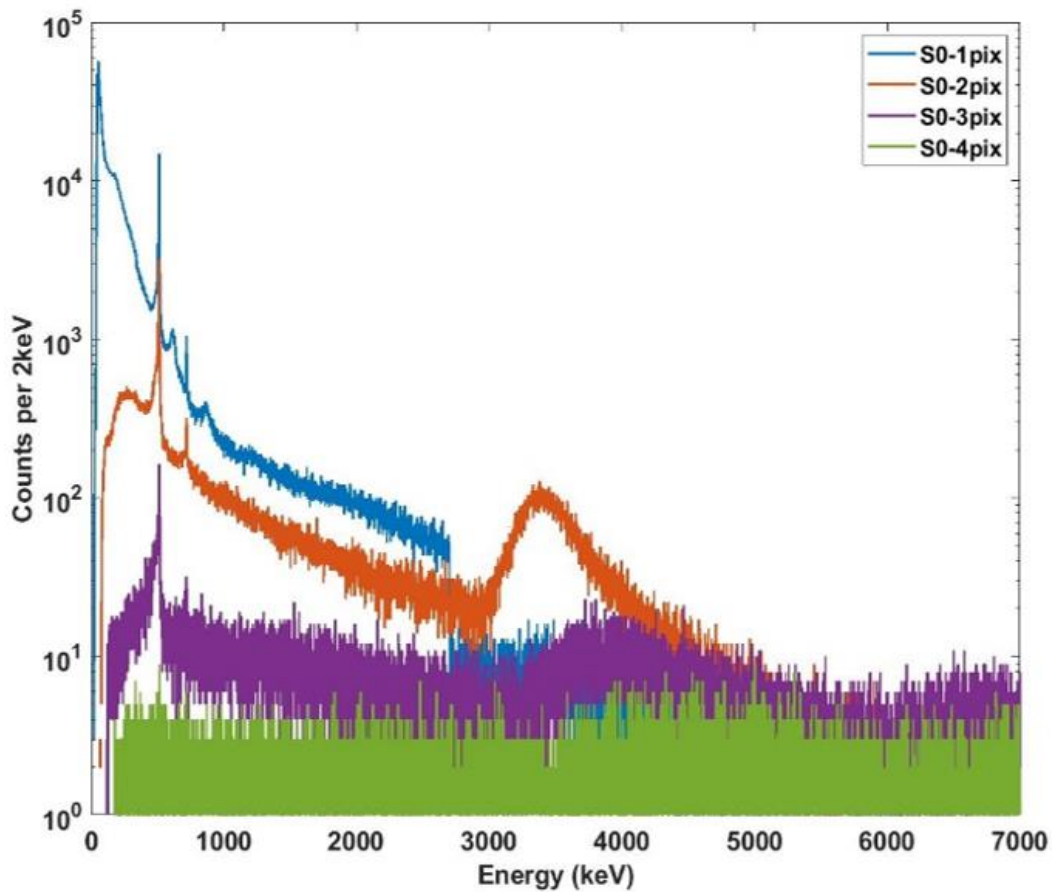


Figure 6.15: Energy spectra for Measurement 13 separated by number of interactions for one M400 system.

6.2.3.1 Comparative Summary

The M400 systems consistently resulted in two orders of magnitude more events recorded over all in comparison to the S400X systems. The larger number of events recorded is majorly attributed to the faster analog ASIC allow for less dead time and more events to be processed. Although, the M400 did not experience the high levels of saturation that the S400X systems did, it did have complications in event reconstruction past 3 MeV and a loss of a crystal, believed to be caused by saturation.

The S400X performance shines in its ability to suppress low-energy noise provided it's within a reasonable range of dead time (60%). However, the capabilities of the wider dynamic range (up to 9 MeV) are lost due to the slower timing of the digital ASIC. In the PuBe measurements, these systems have proved that measuring photopeaks above 3 MeV is possible. However under such a high flux and with very short measurement windows the results in prompt gamma-ray detection did not reflect that.

6.3 Large Array CZT (H3D-J) for Prompt Gamma Detection

The H3D-J detection system houses 64 CZT crystal in two 2×2 arrays (see chapter 2 for further detector specifications) that are in parallel of one another but do not operate in coincidence mode. Each module in the 2×2 array operates independently, only recording events that occur within its bound 16 crystals. This maybe disadvantageous in prompt gamma-ray detection as the Klein-Nishina cross-section shows that forward scattering is more probable for high energy events. Therefore we run the risk of missing out on valuable information without the coincidence mode feature for the two planes of CZT.

The H3D-J system was used for a series of proton beam measurements at the MPTC, showing the capability of large-array, analog, CZT detector system to detect a wide array of photopeaks in a high-flux environment. Figure 6.16 shows the detection setup for the measurements, where the H3D-J system is attached to the underside of the patient bench.

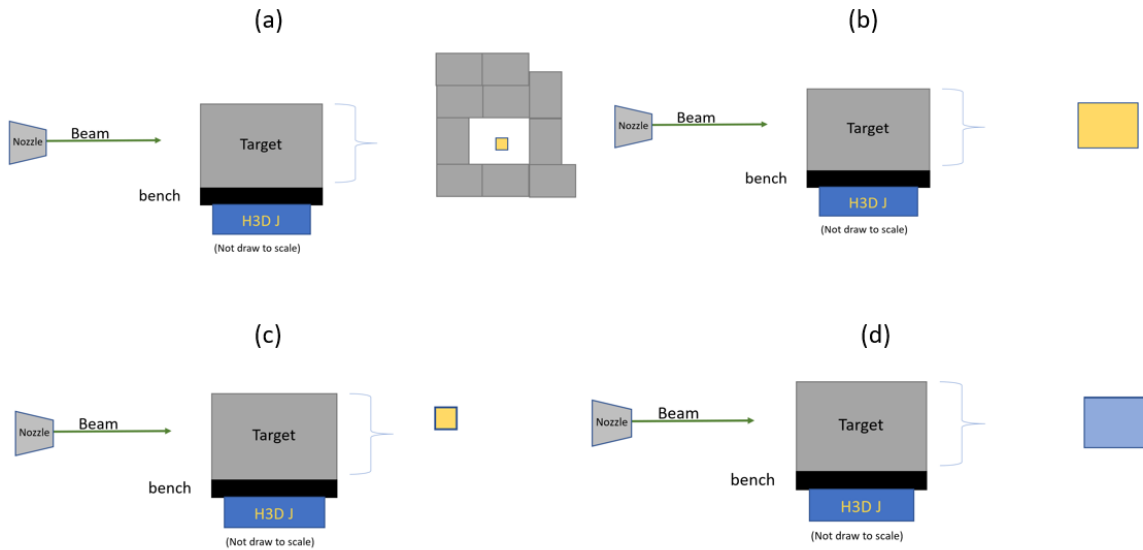
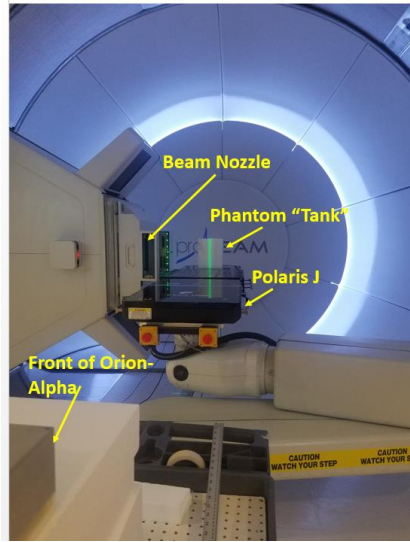


Figure 6.16: Experimental setup of the H3D J system for four different beam measurements: (a) small HDPE tube shielded by lead, (b) a large HDPE tank, (c) unshielded HDPE tube, (d) a large water bottle. Each target is centered above H3DJ which is attached to the underside of the patient bench.

The following figures show the spectral results from the four measurements as a function of total dose. Figure 6.17 highlights the most noticeable feature is from the tube shielded spectra which shows many photopeaks which are a result of lead activation, most likely due to the neutron emission. This is further validated by the very large 558 keV peak in the spectrum as well, which signifies neutron capture on the cadmium in CZT. The H3D-J system also shows a significant

increase in events for the 718 keV photopeak when comparing the tube measurement to the tank measurement. A likely reason for the spike in the photopeak is the increase in dose for the tube measurement, as the lead measurement resulted in full shielding of the 718 keV gamma-rays. Further work could leverage photopeaks in this energy region for dose analysis of the proton beam profile as the energy resolution at this energy for CZT is adequate for analysis.

Figure 6.18 and Figure 6.19 show the high energy spectral features recorded by H3D-J. In these measurements we are able to see the 2.00 MeV from Carbon which typically has a much lower cross-section than the 718 keV and 4.44 MeV photopeaks. The larger dose of the tube measurement allowed for a longer measurement time to collect the less probable events.

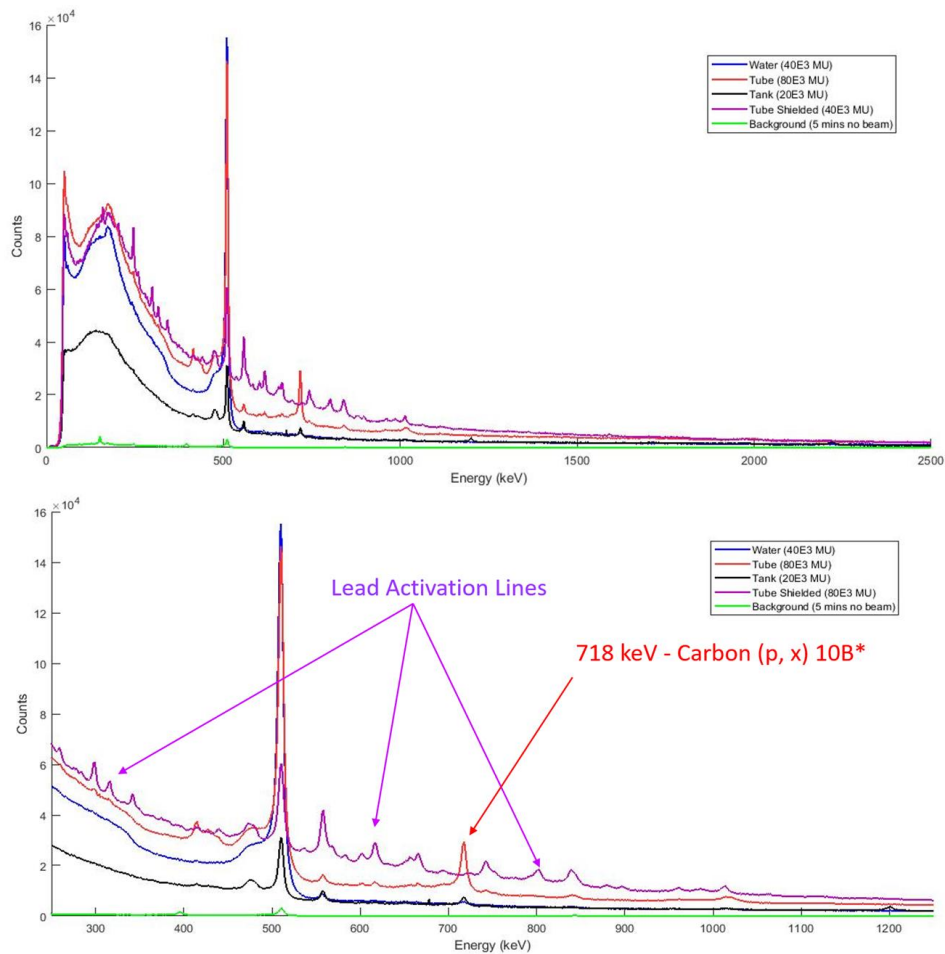


Figure 6.17: Raw recorded energy spectra for the H3D-J measurements.

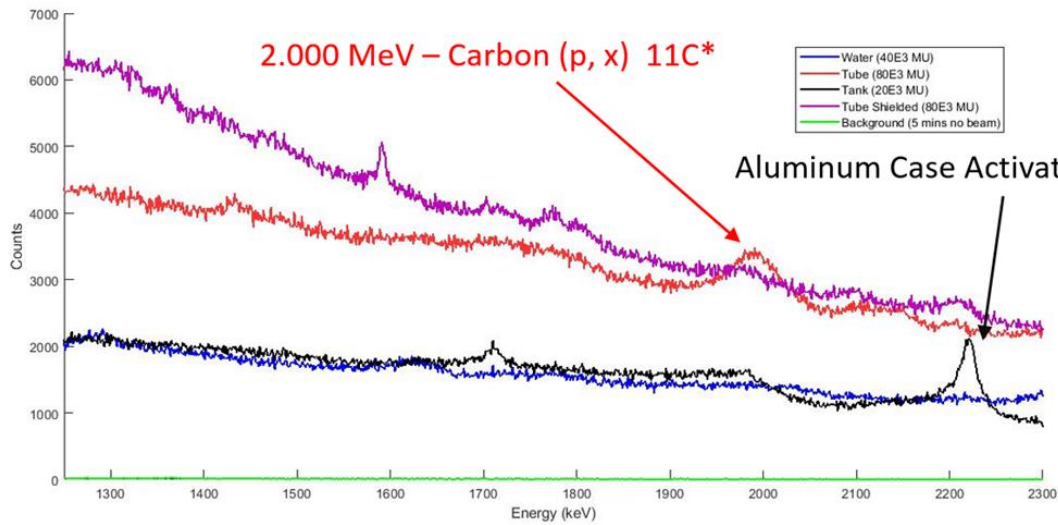


Figure 6.18: Recorded energy spectra range: 1250 keV – 2300 keV.

We also can see features in the water spectrum for the 5.1 MeV oxygen reactions from the water bottle target, and structural features for the 4.44 MeV for majority of the beam measurements in Figure 6.19. H3D-J shows promising results at energies at 2 MeV and below, and it is speculated that with coincidence mode interactions much of the Compton continuum seen for these measurements could be suppressed as those dual plane scatters would be counted as full energy deposition events, where they are now treated as partial energy deposition events in two separate planes only adding noise to the spectrum which will inherently cause noise in the image space as well.

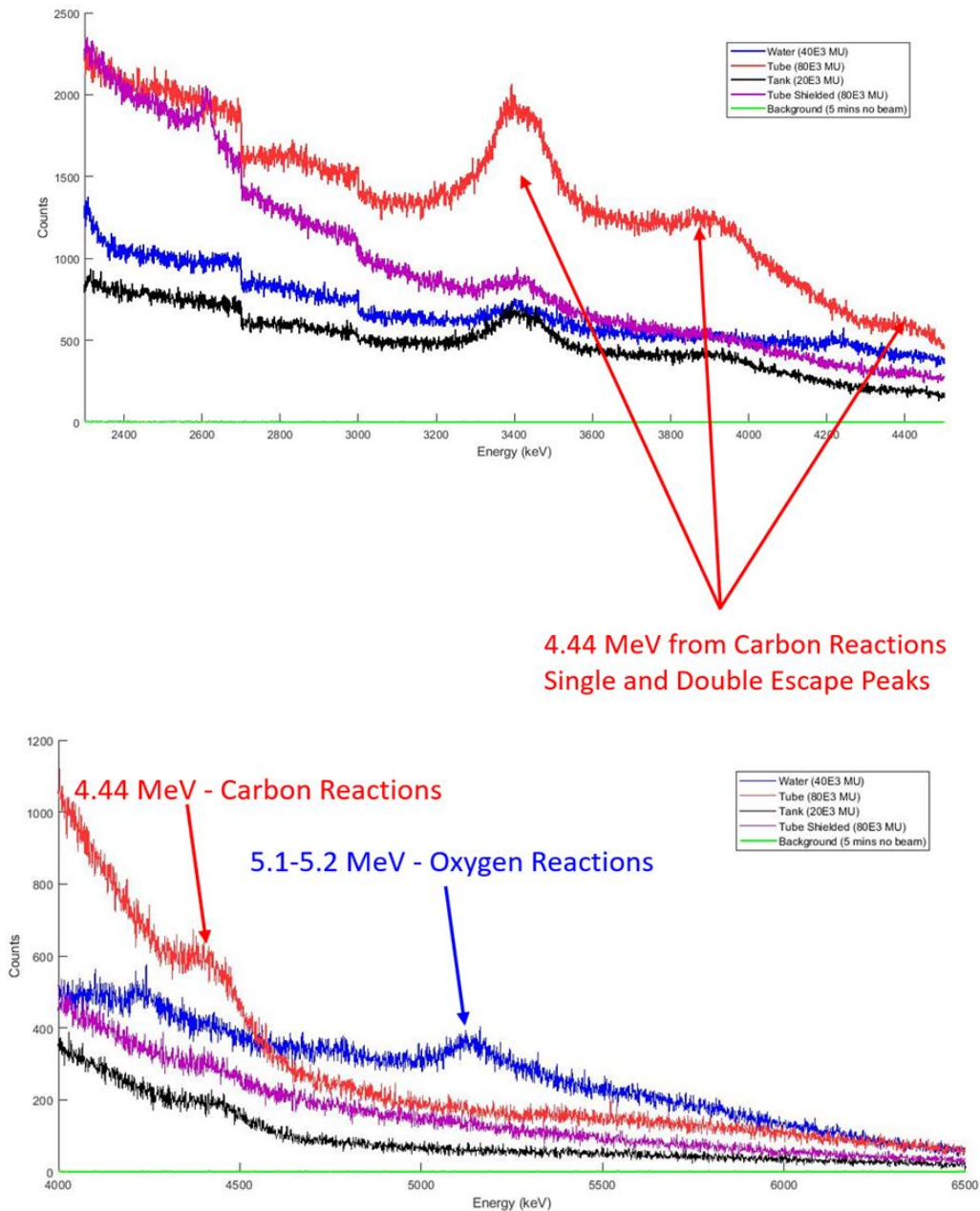


Figure 6.19: High energy spectra from H3D-J measurements.

Figure 6.19 also shows the apparent drop in events at 2.6 MeV due to the energy calibration restriction. The H3D-J system is an analog based system meaning the dynamic range is only 3 MeV as well, however the large number of CZT crystals allows for an increase in detection

efficiency past 3 MeV allowing for photopeak results but with the drawback of poorer energy resolution.

6.4 Conclusion

The overarching theme behind the limitations of CZT in proton beam therapy applications is the timing resolution and energy resolution constraints. CZT has shown that there is room for improvement in both the timing and dynamic range of CZT which could aid in increasing the detection efficiency of those high energy photons, and reducing the noise, spectrally, from partial energy deposition events and chance coincidence events.

Improvement of the timing resolution, especially for the smaller compact CZT systems is hypothesized to help prevent the loss of events over entire crystals from high saturation and dead time. Having a more robust system that can withstand the high flux of photons will maximize the efforts of CZT for prompt-gamma ray detection.

The large-array CZT system is the first of its kind introduced in the Orion research group and shows great potential for large field detection, high-flux, and high energy applications. Even with the limitations of the 3 MeV dynamic range, H3D-J showed that it can provide standard spectral results below 2 MeV and can provide spectral information about those events past its dynamic range. However, imaging with this system has shown to be a challenge as the photopeaks sit on top of a large Compton continuum which is in part due to the independent read out of the four modules in the H3D-J system. With interconnectivity between modules especially interplanar coincidence event recording could lead to improving the detection efficiency of events overall suppressing partial deposition events in the continuum and possibly enhancing those photopeaks past 3 MeV.

CHAPTER VII

Summary and Future Considerations.

7.1 Benefits and Limitations of Using CZT for Proton Beam Range

Verification

The underlying goal of this work is to provide a foundation in the understanding of 3-D position sensitive CZT detectors use in beam range verification for proton therapy for cancer treatment. CZT can provide an alternative approach to verifying the proton beam path and point of rest within the patient through the detection of the prompt gamma rays emitted as the proton interacts with the atoms along its path. Pixelated CZT could be an advantageous approach as it does not require collimation and offers a robust a compact design for easy implementation for detection. With sufficient detection of the prompt gamma rays, images can be reconstructed to provide a visual analysis of the proton beam in space. Preliminary results using 3-D position-sensitive, large volume CZT detectors have demonstrated the potential to provide valuable information in proton beam range verification analysis. The experimental analysis of this work focused on a first order degree of difficulty, detecting prompt gammas from a single homogeneous target from pencil beam irradiations, with the goal of specific photopeak imaging. However the ultimate goal is to provide in-vivo real time imaging of the prompt gammas as they are emitted from multiple materials along the beams path within a patient body.

Both analog and digital ASIC CZT systems provide unique advantages in the application of imaging and detecting high energy photons in a high flux environment. With the improvement of sub-pixel sensing and dynamic range, digital CZT shows the capability to reconstruct photopeaks at high energies in interplanar geometries, where there are two planes of CZT systems for scatter and absorption, and when using only one plane of CZT to collect both interactions. The drawback and space for improvement, however, lies in the timing resolution of the digital ASIC. Digital systems quickly reach saturation in proton therapy settings, which hinders its capability to reconstruct high energy events, and causes hardware issues that depletes the overall detection efficiency.

Analog systems have the advantage of timing resolution allowing upward of 75 kcps depending on the geometry of the system. Although most therapeutic settings can easily surpass this limitation, the analog systems have shown a robust withstanding of the high flux of photons, still providing valuable spectral information. With the limitation of a dynamic range to 3 MeV, the analog systems have shown their promise of collecting high energy photopeak events provided enough statistics.

The H3D-J system is the largest-array CZT system employed for research by the Orion group and its 64-crystal system has shown promising results in the detection of high energy photons. There is much room for improvement in this analog ASIC based system but the large volume of CZT allows for many photons to be detected at once. Implementing features such as interplanar event reconstruction across the four modules in the system could prove to aid in noise reduction and statistical improvement in high-energy photopeak counts.

All systems studied have provided imaging results from prompt gamma-ray data using MLEM imaging. However the M400 system provided superior spatial resolution for further analysis using ROI-MLEM developed in this work.

ROI-MLEM has shown the capability to reconstruct high resolution images for data analysis whilst focusing on a small FOV and mitigating noise interference from incorrectly reconstructed Compton cones. The digital S400X has shown that we can measure a 1 cm difference in peak centroid location at 4.44 MeV via ROI-MLEM imaging. Whereas the M400 system as shown that with one minute measurement windows from proton beam irradiations, the 718 keV photopeak from carbon-proton interactions can be used for image reconstruction for correlation to the proton beam depth and incident energy. ROI-MLEM was designed to provide a less computationally expensive approach to iterative based imaging when the source location is well defined prior to image reconstruction. Truncating the imaging space from a full 4π FOV allows for enhancing the reconstruction of data in the desired region of interest by suppressing data in the space outside of that region. In this work ROI-MLEM is applied to a spherical space, however, could be implemented for cartesian space imaging as well as 3D imaging applications.

There is still much room for improvement overall for detection and imaging with CZT for PBRV however, this foundational work has outlined the current capabilities of CZT in this effort and provide a method of Compton imaging for analysis and correlation of the prompt gamma emission to the profile of the proton beam.

Portions of the work presented in this thesis are based on the motivation discussed by Nwadeyi et al. [95].

7.2 Future Work

As a preliminary study of CZT's performance in prompt gamma ray detection and imaging, there are several areas for future work and improvement upon the work shown here to advance CZT use in proton beam range verification.

7.2.1 Detection Efficiency Improvements through Detector Geometries

With 64 crystals in the H3D-J systems design, leaves open the question if the detection geometry chosen is optimal. Very naive studies were done comparing three different CZT designs to that of the H3D-J geometry, with the only restriction that no more than 64 crystals were used. The results from simulations showed that the detection efficiency could be improved with a more compact design and employing a more Compton telescope geometry to account for more forward scattering events of high energies. This is working with the assumption that interplanar events are

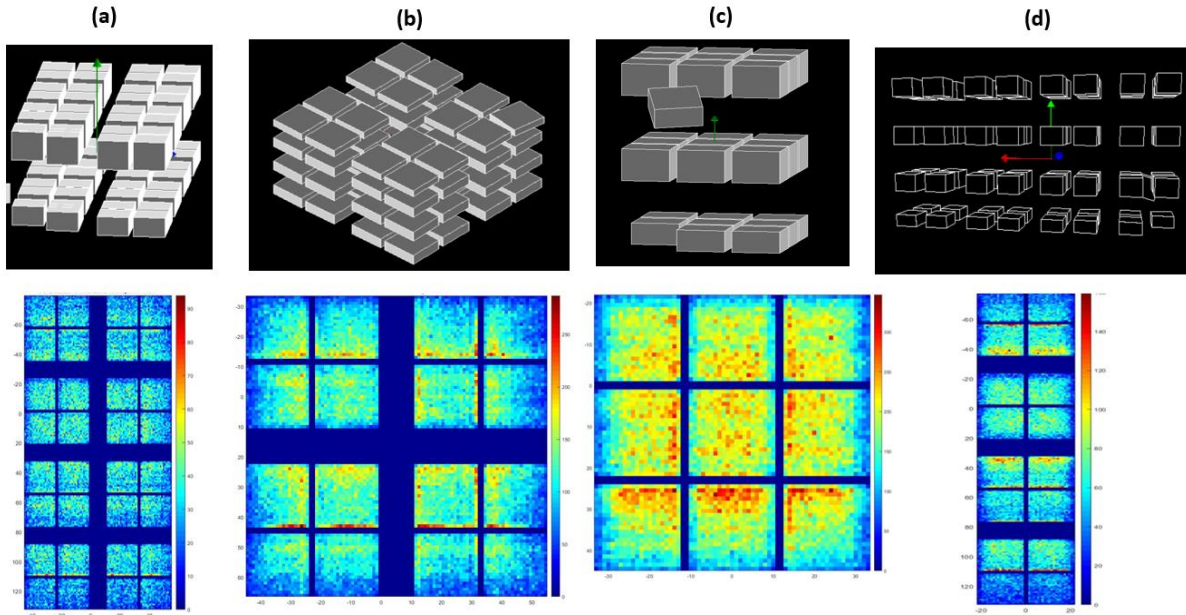


Figure 7.1: Simulated CZT detection geometries: (a) “H3D-J” configuration of 64 crystals, (b) “Square” configuration of 64 crystals and four planes, (c) “Triple” configuration of 27 crystals and three planes, (d) “Long” configuration of 64 crystals, 2×8 crystals per plane for four planes.

collected across multiple planes of CZT. Figure 7.1 shows the four simulated geometries, using Geant4, and brief comparison of the full energy absorption detection efficiency, e^{FE} , of each geometry at 2.31 MeV, 4.44 MeV, and 6.13 MeV, is shown in Figure 7.2.

Equation 7.1 is used to assess the full energy absorption efficiency for each geometry,

$$e^{FE} = \frac{n^{FE}}{N_\gamma} \quad (7.1)$$

where n^{FE} represents the number of photons that resulted in a fully energy absorptions and N_γ is the total number of photos emitted (4e6).

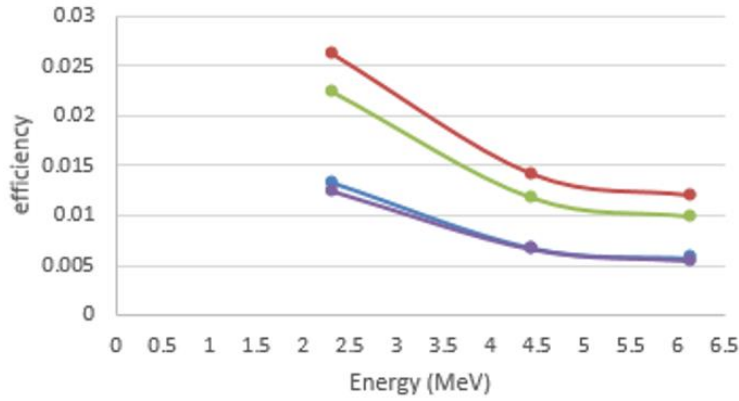


Figure 7.2: Full energy absorption efficiency calculated for each geometry at 2.31 MeV, 4.44 MeV, and 6.10 MeV. Blue: H3D-J, Purple: Long, Red: Square, Green: Triple

Figure 7.2 suggests that the more symmetrical geometries, “Square” and “Triple” perform best at detecting full energy absorption events at higher energies. However, this study is incomplete and there are many different ways to assess detection efficiency for geometries and other parameters that must be taken into consideration. For example the Cramer-Rao bound can

be used to assess the optimal spacing between CZT planes and even crystals in the geometry to optimize spatial resolution and reduce partial energy deposition events from out scattered photons.

7.2.2 Alternative Imaging Methods

In this work MLEM was the primary imaging method use for spatial analysis and comparison of the prompt gamma ray spatial distribution to the proton beam, but there are many different algorithms that could lend additional and enhanced imaging information for this application. For example FBP is a fast alternative to an iterative method such as MLEM, which could provide comparable spatial resolution provided a well-designed PSF for high energy events. Stochastic origin ensemble (SOE) is an alternative iterative approach that bases the update of the image on the probability of comparison of the event origins to randomly selected new event origins in space [96], [97]. The change in the gamma-ray event density along the proton beam could be leveraged using SOE, which could mean that this iterative approach could provide a quickly ascertained imaging result of the prompt gamma ray emission that closely reflects the expected PG distribution from simulations.

3D imaging via MLEM was also tested for PG imaging however the results were inconclusive due to the low statistics of photopeak events in PG data and the large noise profile in the imaging space. With improved detection efficiency and advancements in 3D imaging to allow for small FOV imaging through methods such as ROI-MLEM could be very advantageous in prompt gamma ray imaging. Currently 3D MLEM requires a FOV much larger than the detection system which is computationally expensive when submillimeter resolution is required for analysis. When truncating the 3D cartesian space the corner and edge artifacts are also present as shown in 2D imaging in this work.

From simulations of various target materials being irradiated by proton beams, it is evident that due to the proton threshold energy and elements present in various materials that there is the potential to use multiple PG energy lines for imaging and comparative analysis for the same proton beam irradiation of a specific material. With that said, Energy Integrated Imaging Deconvolution, EIID, maybe a viable imaging modality for this purpose. EIID provides the means of imaging multiple energy peaks and assessing the variation in their locations in space relative to one another, via LM-MLEM iteration. This method has also shown to be somewhat expensive and would require some refinement to allow for submillimeter pixel resolution combined with a large system matrix that encompasses data for multiple energy lines. However in theory this method could provide information about the entire trajectory of the beam as its energy changes, thus its spectral emission will change which could be visualized using EIID and leveraged for beam range verification.

All methods suggested including 2D ROI-MLEM requires further work to push them to real time imaging which is the overarching goal.

7.3 Other Applications of This Work

Though the goal of this thesis was to provide a preliminary study of CZT use for proton beam verification applications, the study of this work could be applied to many realms that interested in high energy photons or data collection and analysis of highly radioactive environments. 3D position sensing CZT has shown it can provide information in both instances and can be useful in non-proliferation efforts such as uranium detection and analysis, waste management and quick search and identify scenarios. Astrophysics is another application that could benefit from Compton telescopes for high energy photon detection and imaging. With improvements in interplanar detection efficiency at high energies, the robust design of the S400

system could prove to be very useful. The modular compact design of the M400 system could lend itself to handheld applications in the medical field such as brachytherapy and high dose rate therapy. The application of CZT strives to be boundless as the development of its enhancement is fostered by research willing to push the bounds of its capabilities.

BIBLIOGRAPHY

- [1] A. H. Compton, "A Quantum Theory of the Scattering of X-rays by Light Elements," *Phys. Rev.*, vol. 21, no. 5, p. 483, May 1923.
- [2] P.G. Lale, "The examination of internal tissues, using gamma-ray scatter with a possible extension to megavoltage radiography," *Phys. Med. Biol.*, vol. 4, no. 2, pp. 159–167, 1959.
- [3] G. Harding and E. Harding, "Compton scatter imaging: A tool for historical exploration," *Appl. Radiat. Isot.*, vol. 68, no. 6, pp. 993–1005, Jun. 2010.
- [4] J. M. Ollinger and J. A. Fessler, "Positron-emission tomography," *IEEE Signal Process. Mag.*, vol. 14, no. 1, pp. 43–55, 1997.
- [5] M. Fontana, *et. al.*, "Compton camera study for high efficiency SPECT and benchmark with Anger system," *Phys. Med. Biol.*, vol. 62, no. 23, pp. 8794–8812, Nov. 2017.
- [6] T. Nakano *et al.*, "Imaging of ^{99m}Tc -DMSA and ^{18}F -FDG in humans using a Si/CdTe Compton camera," *Phys. Med. Biol.*, vol. 65, no. 5, p. 05LT01, Feb. 2020.
- [7] M. Sakai, Y. Kubota, R. K. Parajuli, M. Kikuchi, K. Arakawa, and T. Nakano, "Compton imaging with ^{99m}Tc for human imaging," *Sci. Rep.*, vol. 9, no. 1, Dec. 2019.
- [8] E. R. Christensen, "Monte Carlo calculations for the surface gamma density gauge," *Nucl. Eng. Des.*, vol. 22, no. 2, pp. 342–347, 1972.
- [9] D. Goodman, M. Streicher, Y. Zhu and Z. He, "Identification of Intervening Materials in Gamma-Ray Spectroscopy Measurements Using Angularly Deconvolved Spectra With Multiple Sources in the Field of View," *IEEE Trans. Nuc. Sci.*, vol. 65, no. 3, pp. 924–931, March 2018.
- [10] J. Braga, "Coded Aperture Imaging in High-energy Astrophysics," *Publ. Astron. Soc. Pacific*, vol. 132, no. 1007, p. 012001, Dec. 2019.
- [11] H. Bloemen *et al.*, "COMPTEL imaging of the Galactic disk and the separation of diffuse emission and point sources," *Astrophys. J. Suppl. Ser.*, vol. 92, p. 419, Jun. 1994.
- [12] F. Zhang, "Events Reconstruction in 3-D Position Sensitive CdZnTe Gamma-Ray Spectrometers." Ph. D. Thesis. *University of Michigan*, 2005.
- [13] D. Xu, Z. He, C. E. Lehner, and F. Zhang, "4- π Compton imaging with single 3D position-sensitive CdZnTe detector," *SPIE Hard X-Ray and Gamma-Ray Detector Physics VI*, 2004, vol. 5540, p. 144.
- [14] J. Chu, "Advanced Imaging Algorithms with Position-Sensitive Gamma-Ray Detectors," Ph. D. Thesis., *University of Michigan*. 2018.
- [15] D. Xu, "Gamma-Ray Imaging and Polarization Measurement Using 3-D Position-Sensitive CdZnTe Detectors," Ph. D. Thesis, *University of Michigan*. 2006.
- [16] D. Goodman, "Passive Characterization of Unknown Spaces Using Large-Volume Pixelated CdZnTe," Ph. D. Theis, *University of Michigan*. 2019.
- [17] J. M. Jaworski, "Compton Imaging Algorithms for Position-Sensitive Gamma-Ray Detectors in the Presence of Motion." Ph. D. Thesis, 2013.
- [18] D. Shy, "Super-MeV Compton Imaging and 3D Gamma-Ray Imaging Using Pixelated

- CdZnTe,” Ph. D. Thesis. *University of Michigan*. 2020.
- [19] Glenn G. Knoll, *Radiation Detection and Measurement (4th Edition)*. 2010.
 - [20] P. W. Frame, “A history of radiation detection instrumentation,” *Health Physics*. 2005.
 - [21] Z. He, W. Li, G. F. Knoll, D. K. Wehe, J. Berry, and C. M. Stahle, “3-D position sensitive CdZnTe gamma-ray spectrometers,” *Nucl. Instruments Methods Phys. Res. Sect. A Accel. Spectrometers, Detect. Assoc. Equip.*, vol. 422, no. 1–3, pp. 173–178, 1999.
 - [22] Z. He, “Review of the Shockley-Ramo theorem and its application in semiconductor gamma-ray detectors,” *Nucl. Instruments Methods Phys. Res. Sect. A Accel. Spectrometers, Detect. Assoc. Equip.*, 2001.
 - [23] “Products - H3D, Inc.” [Online]. Available: <https://h3dgamma.com/ProductTiles.php>. 2021.
 - [24] H. Yang, “Applications of Digital ASIC Array System for Noise Analysis , Non-linearity Correction , Event Classification and Reconstruction,” Ph. D. Thesis. *University of Michigan*. 2013.
 - [25] C. G. Wahl *et al.*, “The Polaris-H imaging spectrometer,” *Nucl. Instruments Methods Phys. Res. Sect. A Accel. Spectrometers, Detect. Assoc. Equip.*, vol. 784, pp. 377–381, Jun. 2015.
 - [26] F. Zhang, C. Herman, Z. He, G. De Geronimo, E. Vernon, and J. Fried, “Characterization of the H3D ASIC Readout System and 6.0 cm³ 3-D Position Sensitive CdZnTe Detectors,” *IEEE Trans. Nucl. Sci.*, vol. 59, no. 1, pp. 236–242, 2012.
 - [27] Y. Zhu, S. E. Anderson, and Z. He, “Sub-pixel position sensing for pixelated, 3-D position sensitive, wide band-gap, semiconductor, gamma-ray detectors,” *IEEE Trans. Nucl. Sci.*, 2011.
 - [28] M. W. Streicher, “Applications of Digitized 3-D Position-Sensitive CdZnTe Spectrometers for National Security and Nuclear Nonproliferation,” Ph. D. Thesis. *Univ* 2017.
 - [29] D. Xu, Z. He, C. E. Lehner, and F. Zhang, “4- π Compton imaging with single 3D position-sensitive CdZnTe detector,” *Hard X-Ray Gamma-Ray Detect. Phys. VI*, vol. 5540, p. 144, 2004.
 - [30] C. E. Lehner, “4- π Compton Imaging Using a Single 3-D position sensitive CdZnTe detector,” Ph. D. Thesis, *University of Michigan*. 2004..
 - [31] J. Chu, M. Streicher, J. A. Fessler, and Z. He, “Unbiased Filtered Back-Projection in 4 π Compton Imaging With 3D Position Sensitive Detectors,” *IEEE Trans. Nucl. Sci.*, vol. 63, no. 6, pp. 2750–2756, 2016.
 - [32] D. Shy, J. Xia, and Z. He, “Artifacts in High-Energy Compton Imaging with 3D Position Sensitive CdZnTe.” *IEEE Trans. Nuc. Sci.*, 2020.
 - [33] D. Xu, Z. He, C. E. Lehner, and F. Zhang, “4 π Compton imaging with single 3D position sensitive CdZnTe detector.” *SPIE*. 2004.
 - [34] W. Wang, C. G. Wahl, J. M. Jaworski, S. Member, Z. He, and S. Member, “Maximum-Likelihood Deconvolution in the Spatial and Spatial-Energy Domain for Events With Any Number of Interactions,” *IEEE Trans. Nucl. Sci.*, vol. 59, no. 2, p. 469, 2012.
 - [35] T. Mitin and A. L. Zietman, “Promise and Pitfalls of Heavy-Particle Therapy,” *J Clin Oncol*, vol. 32, pp. 2855–2863, 2014.
 - [36] R. R. Wilson, “Radiological use of fast protons.,” *Radiology*, vol. 47, no. 5, pp. 487–491, 1946.
 - [37] J. H. Lawrence, P. C. Aebersold, and E. O. Lawrence, “Comparative Effects of X-Rays

- and Neutrons on Normal and Tumor Tissue,” *Proc. Natl. Acad. Sci.*, vol. 22, no. 9, pp. 543–557, Sep. 1936.
- [38] R. F. Barth and A. H. Soloway, “Boron Neutron Capture Therapy for Cancer: Cancer Causing Compounds” *Sci. Amer.* vol. 263, no. 4, pp. 100-107. Oct. 1990.
- [39] A. Degiovanni and U. Amaldi, “History of hadron therapy accelerators,” *Physica Medica*, vol. 31, no. 4, pp. 322–332, 01-Jun-2015.
- [40] X. Tian, K. Liu, Y. Hou, J. Cheng, and J. Zhang, “The evolution of proton beam therapy: Current and future status (Review),” *Mol. Clin. Oncol.*, pp. 15–21, 2017.
- [41] “Pummeling Cancer With Protons - Interactive Graphic - NYTimes.com.” [Online]. http://archive.nytimes.com/www.nytimes.com/interactive/2007/12/14/business/20071217_PROTON_GRAPHIC.html?_r=1. 2021.
- [42] J. M. Slater, J. O. Archambeau, D. W. Miller, M. I. Notarus, W. Preston, and J. D. Slater, “The proton treatment center at Loma Linda University Medical Center: Rationale for and description of its development,” *Int. J. Radiat. Oncol. Biol. Phys.*, vol. 22, no. 2, pp. 383–389, Jan. 1992.
- [43] H. Paganetti, *Proton beam therapy*. IOP Publishing Ltd, 2017.
- [44] J. M. Schippers and A. J. Lomax, “Emerging technologies in proton therapy,” in *Acta Oncologica*, 2011, vol. 50, no. 6, pp. 838–850.
- [45] “Gastrointestinal Cancer Treatment - SCCA Proton Therapy Center.” [Online]. Available: <https://www.sccaprotontherapy.com/cancers-treated/gastrointestinal-cancer-treatment>. 2021.
- [46] D. F *et al.*, “Proton therapy in adjuvant treatment of gastric cancer: planning comparison with advanced x-ray therapy and feasibility report,” *Acta Oncol.*, vol. 53, no. 10, pp. 1312–1320, Oct. 2014.
- [47] H. Liu and J. Y. Chang, “Proton therapy in clinical practice,” *Chin. J. Cancer*, vol. 30, no. 5, pp. 315–326, 2011.
- [48] D. Schardt, T. Elsässer, and D. Schulz-Ertner, “Heavy-ion tumor therapy: Physical and radiobiological benefits,” *Rev. Mod. Phys.*, vol. 82, no. 1, pp. 383–425, Feb. 2010.
- [49] J. S. Loeffler and M. Durante, “Charged particle therapy-optimization, challenges and future directions,” *Nature Reviews Clinical Oncology*, vol. 10, no. 7. pp. 411–424, Jul-2013.
- [50] K. Parodi and J. C. Polf, “In vivo range verification in particle therapy,” in *Medical Physics*, 2018, vol. 45, no. 11, pp. e1036–e1050.
- [51] J. Krimmer, D. Dauvergne, J. M. Létang, and Testa, “Prompt-gamma monitoring in hadrontherapy: A review,” *Nuc. Instr. Meth. Phys.*, vol. 878. Elsevier B.V., pp. 58–73, 11-Jan-2018.
- [52] N. Hall and B. Rouge, “The physics of proton therapy,” *Phys. Med. Biol.*, vol. 60, no. 8, 2015.
- [53] N. Boar, “Scattering and Stopping of Fission Fragments.”
- [54] W. H. Bragg and R. Kleeman, “XXXIX. On the α particles of radium, and their loss of range in passing through various atoms and molecules ,” *London, Edinburgh, Dublin Philos. Mag. J. Sci.*, vol. 10, no. 57, pp. 318–340, Sep. 1905.
- [55] J. F. Ziegler, “The Stopping of Energetic Light Ions in Elemental Matter,” 1999.
- [56] “The African School of Physics Lecture : Particle Interactions with Matter,” 2012.
- [57] M. J. Berger *et al.*, “Report 49,” *J. Int. Comm. Radiat. Units Meas.*, vol. os25, no. 2, p. NP-NP, May 1993.

- [58] H. H. Andersen and J. F. Ziegler, "Hydrogen stopping powers and ranges in all elements," Pergamon Press, 1977.
- [59] J. F. Ziegler, M. D. Ziegler, and J. P. Biersack, "SRIM - The stopping and range of ions in matter (2010)," *Nucl. Instruments Methods Phys. Res.*, vol. 268, no. 11–12, pp. 1818–1823, Jun. 2010.
- [60] W. Ulmer, E. Matsinos, K. Frankfurt, and / Oder, "Theoretical methods for the calculation of Bragg curves and 3D distributions of proton beams," *Eur. Phys. J. Spec. Top.*, vol. 190, pp. 1–81, 2010.
- [61] J. M. Verburg, *Reducing range uncertainty in proton therapy*. 2015.
- [62] W. T. Chu, B. A. Ludewigt, and T. R. Renner, "Instrumentation for treatment of cancer using proton and light-ion beams," *Review of Scientific Instruments*, vol. 64, no. 8. American Institute of PhysicsAIP, pp. 2055–2122, 04-Jun-1993.
- [63] W. El Kanawati *et al.*, "Monte Carlo simulation of prompt γ -ray emission in proton therapy using a specific track length estimator," *Phys. Med. Biol.*, vol. 60, no. 20, pp. 8067–8086, Oct. 2015.
- [64] J. C. Polf, D. Mackin, E. Lee, S. Avery, and S. Beddar, "Detecting prompt gamma emission during proton therapy: the effects of detector size and distance from the patient," *Phys Med Biol*, vol. 59, no. 9, pp. 2325–2340, 2014.
- [65] B. Kozlovsky, R. J. Murphy, and R. Ramaty, "Nuclear Deexcitation Gamma-Ray Lines from Accelerated Particle Interactions," *Astrophys. J. Suppl. Ser.*, vol. 141, no. 2, pp. 523–541, Aug. 2002.
- [66] P. Dyer, D. Bodansky, A. G. Seamster, E. B. Norman, and D. R. Maxson, "Cross sections relevant to gamma-ray astronomy: Proton induced reactions," *Amer. Phys. Soc.* vol. 23. no. 5, pp. 1865-1882. 1981.
- [67] F. L. Lang, C. W. Werntz, C. J. Crannell, J. I. Trombka, and C. C. Chang, "Cross sections for production of the 15.1 Mev and other astrophysically significant gamma-ray lines through excitation and spallation of ^{12}C and ^{16}O with protons," *Phys. Rev. C. Nucl. Phys.* vol. 35, no.4, pp. 1214-1227. 1987.
- [68] A. Kowalczyk, "Proton induced spallation reactions in the energy range 0.1-10 GeV," Ph.D Thesis. *Jagiellonian University*. 2008.
- [69] J. Jeyasugiththan and S. W. Peterson, "Evaluation of proton inelastic reaction models in Geant4 for prompt gamma production during proton radiotherapy," *Phys. Med. Biol.*, vol. 60, no. 19, pp. 7617–7635, 2015.
- [70] H. H. Barrett, T. White, and L. C. Parra, "List-mode likelihood," *J. Opt. Soc. Am. A*, vol. 14, no. 11, p. 2914, Nov. 1997.
- [71] J. C. Polf, S. Avery, D. S. Mackin, and S. Beddar, "Imaging of prompt gamma rays emitted during delivery of clinical proton beams with a Compton camera: feasibility studies for range verification," *Phys. Med. Biol. Phys. Med. Biol*, vol. 60, pp. 7085–7099, 2015.
- [72] E. Draeger *et al.*, "3D prompt gamma imaging for proton beam range verification," *Phys. Med. Biol.*, vol. 63, no. 3, Jan. 2018.
- [73] P. G. Ortega *et al.*, "Noise evaluation of Compton camera imaging for proton therapy," *Phys. Med. Biol.*, vol. 60, no. 5, pp. 1845–1863, 2015.
- [74] L. Kelleter *et al.*, "Spectroscopic study of prompt-gamma emission for range verification in proton therapy," *Phys. Medica*, vol. 34, pp. 7–17, 2017.
- [75] V. Ferrero *et al.*, "Evaluation of In-Beam PET Treatment Verification in Proton Therapy

- With Different Reconstruction Methods,” *IEEE Trans. Radiat. Plasma Med. Sci.*, vol. 4, no. 2, pp. 202–211, 2019.
- [76] A. Ziegler, T. Nielsen, and M. Grass, “Iterative reconstruction of a region of interest for transmission tomography,” *Med. Phys.*, vol. 35, no. 4, pp. 1317–1327, Mar. 2008.
 - [77] L. A. Shepp, *et. al.*, “Maximum likelihood pet with real data,” *IEEE Trans. Nucl. Sci.*, vol. 31, no. 2, pp. 910–913, 1984.
 - [78] A. P. Dempster, ; N M Laird, and ; D B Rubin, “Maximum Likelihood from Incomplete Data via the EM Algorithm,” *Royal Stat. Soc.* vol 39, no. 1, pp. 1-38. 1977.
 - [79] Y. Ma *et al.*, “Region-of-interest micro-focus computed tomography based on an all-optical inverse Compton scattering source,” *Matter Radiat. Extrem.*, vol. 5, 2020.
 - [80] D. Goodman, J. Xia, and Z. He, “Qualitative measurement of spatial shielding isotopics via Compton imaging neutron-induced gamma rays using 3-D CdZnTe detectors,” *Nucl. Inst. Methods Phys. Res.*, vol. 935, pp. 214–221, 2019.
 - [81] W. Wang, W. R. Kaye, J. C. Kim, F. Zhang, and Z. He, “Improvement of Compton imaging efficiency by using side-neighbor events,” *Nucl. Instruments Methods Phys. Res. Sect. A Accel. Spectrometers, Detect. Assoc. Equip.*, vol. 687, pp. 62–68, Sep. 2012.
 - [82] F. H. González, M. Rabe, T. Ruggieri, T. Bortfeld, and J. M. Verburg, “A full-scale clinical prototype for proton range verification using prompt gamma-ray spectroscopy,” *Phys. Med. Biol.*, vol. 63, no. 18. 2018.
 - [83] J. M. Verburg, H. A. Shih, and J. Seco, “Simulation of prompt gamma-ray emission during proton radiotherapy,” *Phys. Med. Biol.*, vol. 57, no. 17, pp. 5459–5472, 2012.
 - [84] R. Panthi, P. Maggi, S. Peterson, D. Mackin, and J. Polf, “Secondary Particle Interactions in a Compton Camera Designed for in vivo Range Verification of Proton Therapy,” *IEEE Trans. Rad. Plas. Med. Sci.* vol.5, no. 3, pp. 383-39, 2020.
 - [85] T. Saito, T. Katabuchi, B. Hales, and M. Igashira, “Measurement of thick-target gamma-ray production yields of the ${}^7\text{Li}(p, p'){}^7\text{Li}$ and ${}^7\text{Li}(p, \gamma){}^8\text{Be}$ reactions in the near-threshold energy region for the ${}^7\text{Li}(p, n){}^7\text{Be}$ reaction,” *J. Nucl. Sci. Tech.*, vol. 54, no. 2, pp. 253–259, Feb. 2016.
 - [86] C. Birattari, M. Bonardi, L. Gini, F. Groppi, and E. Menapace, “Experimental Thin-Target and Thick-Target Yields for $\text{natOs}(\alpha, \text{xn})\text{Pt}$, $\text{natOs}(\alpha, \text{X})\text{Os}$, Ir and $\text{natMo}(p, \text{xn})\text{Tc}$ Nuclear Reactions from Threshold up to 38 and 45 MeV, by Combined Single and Stacked Foil Techniques,” *J. Nucl. Sci. Tech.*, vol. 39, pp. 1302–1305, 2014.
 - [87] N. N. Krasnov, “Thick target yield,” *Int. J. Appl. Radiat. Isot.*, vol. 25, no. 5, pp. 223–227, May 1974.
 - [88] M. Aikawa, S. Ebata, and S. Imai, “Thick-target yields of radioactive targets deduced from inverse kinematics,” *Nucl. Inst. Meth. Phys.*, vol. 353, pp. 1-3. 2015.
 - [89] M. Zarifi, S. Guatelli, D. Bolst, B. Hutton, A. Rosenfeld, and Y. Qi, “Characterization of prompt gamma-ray emission with respect to the Bragg peak for proton beam range verification: A Monte Carlo study,” *Phys. Medica*, vol. 33, pp. 197–206, 2017.
 - [90] J. Xia, Y. Zhu, and Z. He, “Efficient temperature corrections for gamma-ray energy reconstruction in 3-D position-sensitive CdZnTe detectors,” *Nucl. Inst. Methods Phys. Res. A*, 2018.
 - [91] F. Zhang and Z. He, “3D position sensitive CdZnTe gamma-ray spectrometers-improved performance with new ASICs.” *SPIE*. 2004.
 - [92] E. Abuelhia, K. Alzimami, M. Alkhorayef, Z. Podolyák, and N. M. Spyrou, “Measurement of coincidence timing resolution of scintillation detectors compared to

- semiconductor detectors to image three-photon positron annihilation,” *J. Rad. Nucl. Chem.*, vol. 278, no. 3, pp. 767–771, Dec. 2008.
- [93] L. J. Meng and Z. He, “Exploring the limiting timing resolution for large volume CZT detectors with waveform analysis,” *Nucl. Instruments Methods Phys. Res. A*, vol. 550, pp. 435–445, 2005.
 - [94] J. Xia, “Interaction Reconstruction in Digital 3-D CdZnTe Under Various Circumstances.” Ph. D. Thesis. *University of Michigan*. 2019.
 - [95] V. Nwadeyi, P. maggi, Z. He, and J. Polf, “Experimental Study of Using a 3-D Position Sensitive CdZnTe Detector for Proton Beam Range Verification,” Mar. 2021.
 - [96] D. Mackin, S. Peterson, S. Beddar, and J. Polf, “Evaluation of a stochastic reconstruction algorithm for use in Compton camera imaging and beam range verification from secondary gamma emission during proton therapy,” *Phys. Med. Biol.*, vol. 57, no. 11, p. 3537, Jun. 2012.
 - [97] A. Andreyev, A. Sitek, and A. Celler, “Fast image reconstruction for Compton camera using stochastic origin ensemble approach,” *Med. Phys.*, vol. 38, no. 1, pp. 429–438, 2011.